New developments in quantum molecular dynamics: excited state dynamics and large scale simulations

Thesis submitted for the degree of

"Doctor Philosophiæ"

CANDIDATE

Francesco Mauri

SUPERVISOR

Prof. Roberto Car

September 1994

SISSA ISAS

SCUOLA INTERNAZIONALE SUPERIORE DI STUDI AVANZATI
INTERNATIONAL SCHOOL FOR ADVANCED STUDIES

New developments in quantum molecular dynamics: excited state dynamics and large scale simulations

Thesis submitted for the degree of

"Doctor Philosophiæ"

CANDIDATE

Francesco Mauri

SUPERVISOR

Prof. Roberto Car

September 1994

Contents

Chapter 1

Introduction

Molecular dynamics (MD) simulations with forces derived from quantum mechanics have been widely applied in solid state physics, in materials science and in physical chemistry [1]. Quantum MD is effective for optimizing atomic geometries either locally or globally using simulated annealing techniques. Moreover it can be used to study both equilibrium and dynamical properties associated with atomic motion at finite temperature.

In quantum MD the ionic forces are determined by the electronic structure, which is usually computed within density functional theory (DFT) in the local density approximation (LDA). This provides a good description of interatomic interactions in a variety of situations involving different chemical bonding such as covalent, metallic and ionic bonding. As a consequence DFT-LDA has considerably improved the predictional power of standard MD simulations based on classical empirical potentials, which have well known transferability problems. Unfortunately the computational cost of MD simulations based on DFT-LDA is considerably greater than that of MD based on classical empirical potentials. In view of this, simplified quantum MD schemes such as those based on empirical tight-binding (TB) Hamiltonians have been used in some cases. TB-MD represents an intermediate scheme between a fully self-consistent DFT-LDA approach and one based on empirical potentials [2]. In particular TB Hamiltonians describe accurately many features of covalently bonded systems.

The treatment of the electronic structure in all quantum MD schemes results in an increase of the computational effort compared to classical MD. In particular, in quantum MD the computational effort grows as the cube of

the number of atoms while it grows only linearly in classical MD. Therefore, if it is nowadays standard to perform classical MD simulations in which the number of atoms is of the order of 10^4 and which last for a time span of nanoseconds, quantum MD can only handle systems with a few hundred atoms for time scales of picoseconds.

Another limitation of quantum MD simulations is that so far these have been restricted to ground state adiabatic processes, while the study of photochemical processes or of light-induced structural modifications would require an excited state adiabatic MD. More generally it would be desirable to extend quantum MD simulations also to non-adiabatic processes since chemical reactions often involve non-adiabatic transitions. This however represents a rather formidable task which poses important conceptual problems that are still open [3].

In this thesis we present new methodological developments that allow to overcome some of the above limitations. In particular:

— We have developed a scheme for adiabatic MD simulations on an excited state Born-Oppenheimer energy surface, i.e. a simulation in which the electrons are kept in an excited state configuration.

— We have proposed a method for electronic structure calculations and quantum MD simulations whose computational cost grows linearly with the system size. Although our formulation is very general, so far we have applied it mainly in the context of TB MD.

— We have devised an acceleration scheme which allows us to increase the integration time step in DFT-LDA quantum MD simulations, in order to extend the accessible time span of these simulations.

Thanks to the above algorithmic advances we have been able to study two physical problems which were out of the reach of the pre-existing methods.

(i) We have used excited state quantum MD to study the formation of light-induced defects in diamond within DFT-LDA. In particular we have considered the phenomenon of self-trapping of core and valence excitons in diamond. In diamond the lower conduction band has antibonding character. If self-trapping occurs, the electrons excited in the conduction band localize on a single crystalline bond which is thus broken. Our calculations predict self-trapping of the $1s$ core exciton and provide a coherent description of the K-edge absorption and emission processes, which compares well with the experimental data. In addition we predict that self-trapping should also occur for the valence biexciton. A self-trapped biexciton would constitute a new

type of intrinsic defect in diamond not yet observed experimentally. In our calculation the biexcitonic self-trapping is accompanied by a large local relaxation of the lattice, producing a kind of local graphitization. This implies a strong Stokes shift in the stimulated-absorption spontaneous emission cycle of about 3 eV, which could be observed experimentally. Moreover our findings have important consequences in the behavior of a high density electron hole plasma in diamond.

(ii) We have used our TB quantum MD scheme, having a numerical cost that scales linearly with system size, to study the impact of C_{60} clusters on a semiconducting surface. We have simulated C_{60} collisions on the clean (2×1) reconstructed (111) surface of diamond using cells containing 1140 atoms. The efficiency of the algorithm has allowed us to carry out all calculations on a workstation. The results of our simulations are in very good agreement with experiments performed under similar impact conditions. In addition our calculations provide a detailed characterization of the microscopic processes occurring during the collision and allow us to identify three impact regimes, as a function of the fullerene incident energy. The three energy regimes (low, medium and high) can be defined according to the modification of the C_{60} ionic structure and to the bonding properties between the cluster and the surface. In particular in the low energy regime, the molecule bounces off the surface without ever forming bonds, and recovers its original shape after severe distortions. In the medium energy regime, C_{60} forms covalent bonds with the surface. The cluster can be either adsorbed on or leave the substrate, preserving its original cage structure with few coordination defects. In the high energy regime the molecule cage structure opens and pieces of the broken cage form stable bonds with the substrate. Finally, we found a relation between the cluster reactivity to the surface and the presence of defects in the cluster. This observation gives us insight into the deposition mechanisms of C_{60} on semiconducting substrates.

1.1   Structure of this work

In Chapter 2 we discuss variational properties of ground and of excited states of a generic Hamiltonian and then we extend this formulation to the framework of DFT. In a variational approach an eigenvalue quantum mechanical problem is recast as a minimization of a functional. This scheme has sev-

eral computational advantages with respect to a direct diagonalization of a Hamiltonian matrix. especially in context of DFT-LDA quantum MD. In the same Chapter we also describe the minimization schemes used in this work, with a particular emphasis on the acceleration methods reported in the Appendix.

In Chapter 3 we discuss the two fundamental approximations which are at the basis of quantum MD schemes, i.e. the adiabatic Born-Oppenheimer decoupling between electronic and ionic motion and the classical approximation for the ionic motion. Then we present the unified approach for ab-initio molecular dynamics introduced by Car and Parrinello (CP) [4], which provides an efficient approach for ground state quantum MD simulations. The variational properties of the excited states discussed in Chapter 3 allows us to extend the CP scheme to excited state quantum MD. Finally the acceleration methods reported in Appendix allows us to increase the integration time step in CP quantum MD.

In Chapter 4 we use the excited state quantum MD to study the excitonic self-trapping in diamond. To this purpose we first introduce the self-trapping phenomena by presenting a qualitative model for such processes. Then we illustrate the theoretical and the experimental facts which suggest the occurrence of self-trapping processes in diamond. Finally we present the results of our DFT-LDA calculations for the core exciton, the valence exciton and the valence biexciton.

In Chapter 5 we present a method for electronic structure calculations and quantum MD simulations whose computational cost grows linearly with the system size. Our approach is based on two ideas: (i) The use of a novel energy functional which does not require either explicit orthogonalization of the electronic orbitals, or inversion of an overlap matrix, and whose minimum coincides with the exact DFT-LDA minimum. (ii) The introduction of localization constraints for the single particle wave-functions. In this Chapter we first discuss the analytic properties of the novel energy functional within DFT-LDA. Then we demonstrate that a quantum MD algorithm with linear system-size scaling can be obtained when the functional is minimized with respect to localized wave-functions. Finally we present a practical implementation of this algorithm in a TB context.

In Chapter 6 we use the TB quantum MD scheme having computational cost that grows linearly the system size to study the impact of a C_{60} fullerene on a clean (2×1) reconstructed (111) surface of diamond.

6

In the Appendix we reproduce a reprint of Ref. [5], in which we introduce acceleration schemes for DFT-LDA quantum MD and electronic structure calculations. In particular we present a fictitious damped second-order dynamics for total energy minimizations and we show that the convergence rate of this dynamics is comparable to that of conjugate gradient methods. Moreover we increase the integration time step in damped second-order dynamics and in CP quantum MD by preconditioning the fictitious electronic motion. Finally we analyse in detail a numerical instability, usually referred to as charge sloshing instability, which could be induced by the Coulomb potential in large supercells.

Chapter 2

Variational formulation of the eigenvalue-eigenvector problem

The matrix formulation of quantum mechanics reduces any quantum mechanical problem to the diagonalization of matrices. In a practical calculation finite matrices are used. These are obtained by approximating the wave-function Hilbert space with a vector space of finite dimension, and by expanding the wave-functions on a finite basis of this vector space.

However, in some cases the direct diagonalization presents a number of difficulties and/or practical inefficiencies. In particular a direct diagonalization provides all the eigenvectors and eigenvalues of the vector space, whereas often only occupied eigenstates are sought. The empty state overload is particularly important, if the number of occupied states is much smaller than the dimension of the vector space, e.g. in a plane-wave formulation. Furthermore, if the Hamiltonian matrix depends self-consistently on the occupied eigenstates as in density functional theory (DFT) or in a mean field approximation, the direct diagonalization has to be repeated many times up to the reach of self-consistency. Another inefficiency of the direct diagonalization turns out, whenever the eigenvectors are sought as a function of some continuously changing external parameters in the Hamiltonian, as e.g. in quantum molecular dynamics. Indeed the diagonalization at a given value of the external parameters takes no advantages from the solution obtained at the previous values of the parameters. Finally it is not possible to use a matrix representation whenever the approximate wave-functions used in a calculation belong to a subset of the Hilbert space which is not a vector space. This

8

is the case, for instance. of variational quantum MonteCarlo, where approximate eigenstates of the Hamiltonian are obtained by constructing a family of trial functions that depend on a number of parameters, and subsequently by looking for the optimal values of these parameters. The wave-functions do not span a vector space also in the case treated in Chapter 5 where we present an algorithm based on a localized orbital formulation, whose computational workload grows linearly with the system size.

Variational approaches represent an alternative to direct matrix diagonalization, which do not suffer from the above limitations. In a variational formulation the eigenvalue eigenvector problem is recast as a minimization of a functional. The functional to minimize contains only the occupied wave-functions. Self consistency loops are not required, since DFT or other mean field theories are often based on a variational principle. When the Hamiltonian depends on some external parameters, the minimization of the functional at a given value of the external parameters can use, as a starting guess, the result of a minimization performed for close values of the external parameters. Finally the subset spanned by the wave-functions has not to be a vector space.

In this Chapter we discuss the variational properties of the ground state and of the excited states. first for a generic Hamiltonian in Sec. 2.1, and then in the framework of DFT in Sec. 2.2. Furthermore we introduce in Sec. 2.3 the minimization schemes used in this thesis work. In particular we give in the same Sec. a brief overview of the acceleration methods introduced in Ref. [5]. A reprint of Ref. [5] is reproduced in the Appendix.

2.1   Energy and variance

Given an Hamiltonian H and a generic wave-function ψ we define the energy functional $E[\psi]$ by taking the expectation value the Hamiltonian:

$$E[\psi] = < \psi|H|\psi >, \tag{2.1}$$

where wave-function ψ is normalized, i.e.:

$$< \psi|\psi >= 1 \tag{2.2}$$

To simplify the notation in the following ψ is supposed to be real.

9

We now consider when this energy functional is stationary with respect to ψ. To this purpose we calculate the functional derivative of $E[\psi]$ with respect to ψ:

$$\frac{\delta E[\psi]}{\delta|\psi>} = 2(H|\psi> +\lambda|\psi>) \qquad (2.3)$$

where λ is the Lagrangian multiplier which assures the normalization. The energy functional is stationary with respect to ψ when the functional derivative is equal zero, i.e. when:

$$H|\psi> = -\lambda|\psi> \qquad (2.4)$$

This equation is verified if and only if ψ is an eigenstate of H. In particular, if ψ is equal to the minimum energy eigenvector of H, the stationary point is the absolute minimum of $E[\psi]$. Thus the ground state eigenenergy and the ground state eigenfunction can be calculated by minimizing the energy functional $E[\psi]$.

If ψ is a generic eigenstate of H the stationary point of $E[\psi]$ is only a saddle point, i.e. along some directions $E[\psi]$ has a positive curvature (positive second derivative) and along other directions $E[\psi]$ has a negative curvature (negative second derivative). As a consequence the excited state eigenenergies and the excited state eigenfunctions can not be obtained by a direct minimization of $E[\psi]$.

We now formulate a variational principle for the excited states. To this purpose let us consider the variance of the Hamiltonian:

$$\mathcal{V}[\psi] = <\psi|H^2|\psi> - <\psi|H|\psi>^2 = |[H- <\psi|H|\psi>]|\psi>|^2 \qquad (2.5)$$

Since $\mathcal{V}[\psi]$ is the square modulus of a vector, $\mathcal{V}[\psi]$ is non-negative and it is equal to zero if and only if ψ is an eigenstate of H. Thus a generic eigenstate of H is a local minimum of $\mathcal{V}[\psi]$ and it can be obtained by minimizing the variance in place of the energy.

Finally we combine the energy and the variance to define a new energy functional $U[\psi]$:

$$U[\psi] = E[\psi] + \eta\mathcal{V}[\psi] \qquad (2.6)$$

where η is a positive constant. $U[\{\psi\}]$ is stationary if and only if ψ is a generic eigenstate of H, since it is the sum of two quantities which have this property. Moreover the eigenstate with eigenvalue E_i is a local minimum of

$U[\psi]$ if $\eta > 1/(E_i - E_g)$ where E_g is the ground state eigenvalue. Indeed under this condition the negative second derivatives of $E[\psi]$ are smaller than the positive second derivatives of $\eta V[\psi]$. We finally note that $U[\psi]$ coincides with $E[\psi]$ on its local minima since on the eigenstates the variance is zero.

2.2 Energy and variance in density functional theory

In this Section we introduce the DFT formalism and we extend to this framework the considerations done the previous Section. The Hohenberg and Kohn theorem in the Kohn and Sham formulation uses the ground state variational principle to map an interacting electron system onto a non-interacting electron system with a self-consistent Hamiltonian [6]. In particular, for a system of N interacting electrons. Kohn and Sham defined an energy functional $E[\{\psi\}]$ of $N/2$ single particle doubly occupied orbitals $\{\psi\}$, such that the ground state energy and the ground state density are obtained by minimizing $E[\{\psi\}]$ with respect to $\{\psi\}$. $E[\{\psi\}]$ is defined as:

$$E[\{\psi\}] = < \psi_i| - \nabla^2|\psi_i > + \int V_{ext}(\mathbf{r})n(\mathbf{r})d^3r + \frac{1}{2}\int \frac{n(\mathbf{r})n(\mathbf{r}')}{|\mathbf{r} - \mathbf{r}'|}d^3r d^3r' + E_{xc}[n],$$

(2.7)

where $V_{ext}(\mathbf{r})$ is the one body external potential, $E_{xc}[n]$ is the exchange-correlation functional,

$$n(\mathbf{r}) = 2 < \psi_i|\mathbf{r} >< \mathbf{r}|\psi_i >$$

(2.8)

is the electronic density and the single particle doubly occupied orbitals $\{\psi\}$ are orthonormal, i.e.:

$$< \psi_i|\psi_j >= \delta_{ij}.$$

(2.9)

Note that $E[\{\psi\}]$ is invariant under unitary rotation in the occupied subspace.

In its exact form the functional in Eq. (2.7) is of no practical use since an explicit expression of $E_{xc}[n]$ is unknown. However there are simple and accurate approximations to $E_{xc}[n]$ which allow us to evaluate explicitly the exchange and correlation energy. The simplest and most widely used approximation is the so called Local Density Approximation (LDA) that states that

the contribution of each small volume of the system to $E_{xc}[n]$ is the same as in an homogeneous electron gas of density equal to the local one:

$$E_{xc}^{LDA}[n] = \int d^3r \epsilon_{xc}^{hom}(n(\mathbf{r}))n(\mathbf{r}) \qquad (2.10)$$

where $\epsilon_{xc}^{hom}(n)$ is the exchange and correlation energy per particle of the homogeneous electron gas of density n.

To study when $E[\{\psi\}]$ is stationary we consider the functional derivative of $E[\psi]$ with respect to $\{\psi\}$:

$$\frac{\delta E[\{\psi\}]}{\delta|\psi_i>} = 2(2H_{KS}|\psi_i> +\lambda_{ij}|\psi_j>). \qquad (2.11)$$

Here λ_{ij} is a symmetric matrix of Lagrangian multipliers, which ensure the orthonormalization, and the Kohn Sham Hamiltonian H_{KS} is defined as:

$$H_{KS} = -\frac{1}{2}\nabla^2 + V_{ext}(\mathbf{r}) + \int \frac{n(\mathbf{r}')}{|\mathbf{r}-\mathbf{r}'|}d^3r' + V_{xc}(\mathbf{r}) \qquad (2.12)$$

where $V_{xc}(\mathbf{r}) = \delta E_{xc}[n]/\delta n(\mathbf{r})$ is the exchange-correlation potential. The functional is stationary with respect to $\{\psi\}$ when the rhs Eq. (2.11) is equal to zero, i.e. when $\{\psi\}$ are eigenstates of H_{KS} or are the result of a unitary rotation of $N/2$ eigenstates of H_{KS}.

In principle, only the energy and the density on the absolute minimum of the Kohn Sham functional are equal to the corresponding quantities of the interacting electronic system, while the other saddle points of $E[\{\psi\}]$ have no physical meaning. However, in many cases the stationary point of $E[\{\psi\}]$ can be a valuable approximation to the excited states energy and density of the interacting electronic system. In Chapter 4 we use the saddle points of $E[\{\psi\}]$ to describe electronic excitations. We defer to this Chapter for a more detailed discussion on this assumption.

To apply a variational procedure for a general saddle point of $E[\{\psi\}]$, we define the variance of the Kohn and Sham Hamiltonian H_{KS} as:

$$\mathcal{V}[\{\psi\}] =< \psi_i|H_{KS}^2|\psi_i> - < \psi_i|H_{KS}|\psi_j><\psi_j|H_{KS}|\psi_i> \qquad (2.13)$$

It is easy to show that $\mathcal{V}[\{\psi\}]$ is invariant under unitary rotation in the occupied subspace as the energy functional $E[\{\psi\}]$: $\mathcal{V}[\{\psi\}]$ is non negative

and is zero if and only if the $\{\psi\}$ are eigenstates of H_{KS} or a unitary rotation of H_{KS} eigenstates. Thus $\mathcal{V}[\{\psi\}]$ has local minima which coincide with the saddle points of $E[\{\psi\}]$. Finally, in analogy with what done in the previous Section, we combine the energy and the variance to define a new functional $U[\{\psi\}]$, which has the excited states as local minima and which coincides with $E[\{\psi\}]$ on the local minima.

$$U[\{\psi\}] = E[\{\psi\}] + \eta \mathcal{V}[\{\psi\}] \tag{2.14}$$

To minimize $U[\{\psi\}]$ we make use of the derivative of $U[\{\psi\}]$ with respect to $\{\psi\}$ which is given by:

$$\frac{\delta U[\{\psi\}]}{\delta|\psi_i>} = \frac{\delta E[\{\psi\}]}{\delta|\psi_i>} + 2\eta(H_{KS}^2|\psi_i> - 2H_{KS}|\psi_j><\psi_j|H_{KS}|\psi_i> + V_V|\psi_i>), \tag{2.15}$$

were $V_V(\mathbf{r})$ is a local potential defined as:

$$V_V(\mathbf{r}) = \int \left[\frac{1}{|\mathbf{r}-\mathbf{r}'|} + \frac{\delta V_{xc}(\mathbf{r}')}{\delta n(\mathbf{r})} \right] n_V(\mathbf{r}') d^3r', \tag{2.16}$$

and the density $n_V(\mathbf{r})$ is defined as:

$$n_V(\mathbf{r}) = 2(<\psi_l|\mathbf{r}><\mathbf{r}|H_{KS}|\psi_l> - <\psi_l|\mathbf{r}><\mathbf{r}|\psi_m><\psi_m|H_{KS}|\psi_l>). \tag{2.17}$$

Note that in an infinite system the long range integral appearing in Eq. (2.16) can be treated as a Coulomb potential of a globally neutral charge distribution since $\int n_V(\mathbf{r})d^3r = 0$. For the sake of numerical efficiency, before evaluating the charge density $n_V(\mathbf{r})$, it is useful to rotate the set of occupied wave-functions $\{\psi\}$ in order to obtain the set $\{\bar{\psi}\}$ such that the matrix $<\bar{\psi}_m|H_{KS}|\bar{\psi}_l>$ is diagonal. Then Eq. (2.17) can be rewritten as:

$$n_V(\mathbf{r}) = 2(<\bar{\psi}_l|\mathbf{r}><\mathbf{r}|H_{KS}|\bar{\psi}_l> - <\bar{\psi}_l|\mathbf{r}><\mathbf{r}|\bar{\psi}_l><\bar{\psi}_l|H_{KS}|\bar{\psi}_l>). \tag{2.18}$$

2.3 Minimization algorithms

In this Section we briefly describe the minimization schemes applied in this work. A more comprehensive analysis of the different minimization algorithms and the details of their numerical implementation are given in the reprint of Ref. [5] reproduced in the Appendix.

13

Our minimization schemes require explicit knowledge of the first derivative of the functional with respect to the wave-functions. Indeed the evaluation of this gradient implies only a small computational overload once the energy is calculated. We used two different approaches: namely an approach based on fictitious dynamical methods and an approach based on conjugate gradient (CG) scheme. The dynamical methods, introduced in the context of DFT in Ref.[4], are based on a fictitious dynamics for the wave-functions which converges asymptotically to the minimum of the functional.

In particular the simplest fictitious dynamics is the steepest descent. It can be viewed as a dynamics of the first order in the time derivative:

$$\mu | \dot{\psi}_i > = -\frac{1}{2} \frac{\delta E[\{\psi\}]}{\delta | \psi_i >} \tag{2.19}$$

where μ is a fictitious electronic mass. This equation can be integrated in time by finite differences. The resulting discretized motion converge exponentially to the minimum of the functional in a number of time steps which depends both on the system and on the functional. A more advantageous dynamical method is based on a Newtonian dynamics with a friction term:

$$\mu | \ddot{\psi}_i > = -\frac{1}{2} \frac{\delta E[\{\psi\}]}{\delta | \psi_i >} - 2\gamma\mu | \dot{\psi}_i > \tag{2.20}$$

Here γ is a damping constant, which, as shown in Ref. [5], has to be chosen appropriately in order to induce critical damping on the slowest component of the motion. Also in this case the discretized motion converges exponentially to the minimum of the functional. However the number of iteration required to reach with damped dynamics a given convergence is the square root of the number of iterations required by steepest descent (see Ref. [5] or in the Appendix). The gain compared to steepest descent is particularly important when a large number of iterations is needed to converge to the ground-state, which is typically the case of metallic systems.

The fictitious mass μ in Eq.s (2.19,2.20) is used to tune the speed of the electronic fictitious dynamics and does not describe any other physical property. For a time independent functional this mass is irrelevant since it can be included in the definition of the integration time step. The mass μ can be replaced by a any positive definite operator $\hat{\mu}$. This arbitrariness in the choice of $\hat{\mu}$ is useful to precondition the fictitious dynamics: by giving

higher masses to the higher frequency components of the fictitious motion the integration time step can be increased. This is the basic idea of the mass preconditioning introduced in the context of dynamical methods in Ref. [5] (Appendix). The highest frequency components in calculations with a plane-wave basis set are due to the high energy unoccupied Hamiltonian eigenstates which are free particle like. Therefore, for the minimization of the energy functional $E[\{\psi\}]$, it is convenient to choose an operator $\hat{\mu}$ which is diagonal in q-space has eigenvalues $\mu(q)$ proportional to the kinetic energy for high q:

$$\begin{aligned}
\mu(q) &= \mu_0 & \text{if } \tfrac{1}{2}q^2 < E_p \\
\mu(q) &= \mu_0 \tfrac{q^2}{2E_p} & \text{if } \tfrac{1}{2}q^2 > E_p
\end{aligned} \qquad (2.21)$$

Below a cutoff energy E_p, it is worth considering a constant mass μ_0, because the low energy eigenstates are not free-particle like. The preconditioning cut-off E_p therefore represents the threshold above which the states are dominated by the kinetic energy. As shown in Ref. [5] (Appendix) the mass preconditioning allows to increase the convergence rate in the damped dynamics minimization of $E[\{\psi\}]$ by a factor of 2-3.

For the minimization of the energy functional $U[\{\psi\}]$, it is convenient to choose a mass operator $\mu(q)$ proportional at high q to the square of the kinetic energy:

$$\begin{aligned}
\mu(q) &= \mu_0 & \text{if } \tfrac{1}{2}q^2 < E_p^2 \\
\mu(q) &= \mu_0 \left(\tfrac{q^2}{2E_p}\right)^2 & \text{if } \tfrac{1}{2}q^2 > E_p
\end{aligned} \qquad (2.22)$$

In the damped dynamics minimization of $U[\{\psi\}]$ the mass preconditioning allows to increase the convergence rate by a factor of 4-9.

When mass preconditioning is used, the standard algorithm which computes the orthonormality constraints, has to be modified as specified in Appendix. The modified algorithm has a computational overload which is negligible in system with less than ~ 400 electrons.

The second minimization approach used in this thesis is the CG method. A general description of this approach is given in Ref. [7]. In Ref. [8] CG algorithms are introduced in the context of DFT. In Ref. [5] (Appendix) it is shown that, in electronic energy minimization, the convergence rate of the CG method is equal to that of the dynamical method based on the damped Newtonian dynamics. Thus a choice between the two approaches mainly relies on the following considerations. In the CG method there are no minimization parameters such as a time step or a damping coefficient. Therefore

15

the CG method is more suitable to be used as a black box algorithm. However, in the CG method, at each step the functional is minimized along the straight line of the conjugate direction. Since a line minimization is not defined in presence of explicit constrains as the orthonormalization constrains, the CG method can be applied only to unconstrained functionals. Furthermore, due to the line minimization, a code based on a CG method is more complex than a code based on a dynamical approach.

Chapter 3

Quantum molecular dynamics

Quantum molecular dynamics allows us to obtain from first-principles electronic, structural, dynamical and thermodynamical properties of real materials. In quantum molecular dynamics the electrons are treated within quantum mechanics, whereas the ionic motion is described by classical Newtonian dynamics. For each given ionic position the electrons are supposed to be in an instantaneous eigenstate of the electronic Hamiltonian, whose eigenenergy defines the ionic classical potential energy. The two basic approximations which are understood in this treatment are the adiabatic BO decoupling between the electronic motion and the ionic motion, which is justified by the large ion/electron mass ratio, and the classical approximation for the ionic motion. Note that the second approximation requires the validity of the first one.

Along the ionic trajectory, the electronic eigenstates and eigenenergies can be computed using two different approaches: either by minimizing the energy functional introduced in the previous Chapter at each ionic step or by moving the electronic wave-functions according to an appropriate fictitious dynamics. In the latter case the adiabatic *real* dynamics of the electronic quantum system is simulated by an adiabatic *fictitious* dynamics suitable for an efficient numerical integration. This is the key idea of the unified approach for ab-initio molecular dynamics introduced by Car and Parrinello [4].

The Chapter is organized as follows. In Sec. 3.1 we derive the equations of motion of quantum molecular dynamics. In Sec. 3.2 we show how the ionic forces can be evaluated. In Sec. 3.3 we introduce the Car-Parrinello fictitious dynamics and we discuss the basic ideas of this method.

3.1 Adiabatic and classical approximation for the ionic motion

In this Section we specified the equations of motion of the quantum molecular dynamics. To this purpose two consecutive approximations to the exact ionic-electronic dynamics are applied: the Born-Oppenheimer (BO) adiabatic approximation and the classical approximation for the ionic motion.

The evolution of a ionic-electronic system is dictated by the Schroedinger equation:

$$i\hbar\dot{\Phi}(\mathbf{R},\mathbf{r}) = [-\frac{1}{2M}\nabla_{\mathbf{R}}^2 - \frac{1}{2m}\nabla_{\mathbf{r}}^2 + V(\mathbf{R},\mathbf{r})]\Phi(\mathbf{R},\mathbf{r}) \qquad (3.1)$$

were $\mathbf{R}$ and $\mathbf{r}$ are ionic and electronic positions, M and m are ionic and the electronic masses and $V(\mathbf{R},\mathbf{r})$ is the potential energy operator. The exact solution of Eq. (3.1) can be formally written as:

$$\Phi(\mathbf{R},\mathbf{r},t) = \sum_k \phi_k(\mathbf{R},t)\chi_{k,\mathbf{R}}(\mathbf{r}). \qquad (3.2)$$

were the electronic wave-functions $\chi_{k,\mathbf{R}}(\mathbf{r})$ are the solution of the eigenvalue problem:

$$[-\frac{1}{2m}\nabla_{\mathbf{r}}^2 + V(\mathbf{R},\mathbf{r})]\chi_{k,\mathbf{R}}(\mathbf{r}) = E_k(\mathbf{R})\chi_{k,\mathbf{R}}(\mathbf{r}). \qquad (3.3)$$

Here the index k is the electronic quantum number and the ionic coordinates $\mathbf{R}$ act as an external parameter.

In general the evolution of the ionic wave-function $\phi_k(\mathbf{R},t)$ at a given k is entangled with the the evolution of ionic wave-functions at different k. However, the large ratio between ionic and electronic masses justifies the use of the the adiabatic BO approximation [9]; within this approximation the evolutions of the ionic wave-functions with different k are decoupled. Indeed within the BO approximation the ionic wave-functions obey a Schroedinger equation:

$$i\hbar\dot{\phi}_k(\mathbf{R}) = [-\frac{1}{2M}\nabla_{\mathbf{R}}^2 + E_k(\mathbf{R})]\phi_k(\mathbf{R}). \qquad (3.4)$$

Note that in this equation the eigenvalues $E_k(\mathbf{R})$ of the electronic Hamiltonian act on the ionic wave-functions as a potential energy. Thus the energies $E_k(\mathbf{R})$ are commonly called BO potential energy surfaces.

The second approximation of quantum molecular dynamics is the replacement of the quantum description of the ionic motion on a given BO surface with a classical description. This approximation is justified if the ionic temperature is not to low , e.g. if in a solid the ionic temperature is larger than the Debye temperature, or whenever quantum effects such as zero point motion, tunneling or quantization of the ionic energy levels are irrelevant for the properties under study. In the classical approximation the Schroedinger Eq. (3.4) is replaced by the Newton equation:

$$M\ddot{\mathbf{R}} = -\frac{dE_k(\mathbf{R})}{d\mathbf{R}}.$$ (3.5)

Eq. (3.3) and Eq. (3.5) define the evolution of the ionic-electronic system in quantum molecular dynamics. Then the energy conserved during the ionic motion is:

$$E_{qmd} = \frac{1}{2}M\dot{\mathbf{R}}^2 + E_k(\mathbf{R})$$ (3.6)

In the following the electronic eigenenergies E_k will be evaluated in the framework of density functional theory (DFT) as the values of the Kohn and Sham energy functional $E[\{\psi\}]$ on its stationary points.

3.2   Ionic forces

In quantum molecular dynamics the classical forces acting on the ions are defined as the total derivatives of the electronic eigenenergy $E_k(\mathbf{R})$ with respect to the ionic positions $\mathbf{R}$. Within DFT we have:

$$E_k(\mathbf{R}) = E[\{\chi_{k,\mathbf{R}}\}, \mathbf{R}]$$ (3.7)

where $\{\chi_{k,\mathbf{R}}\}$ makes the functional stationary with respect to its first argument and the second argument underlines the explicit dependence of the electronic external potential upon the ionic positions $\mathbf{R}$. Then the force on the ions is given by:

$$-\frac{dE_k(\mathbf{R})}{d\mathbf{R}} = -\frac{\partial E[\{\chi_{k,\mathbf{R}}\}, \mathbf{R}]}{\partial\{\chi_{k,\mathbf{R}}\}}\frac{\partial\{\chi_{k,\mathbf{R}}\}}{\partial\mathbf{R}} - \frac{\partial E[\{\chi_{k,\mathbf{R}}\}. \mathbf{R}]}{\partial\mathbf{R}}.$$ (3.8)

Since $E[\{\psi\}, \mathbf{R}]$ is stationary for $\{\psi\} = \{\chi_{k,\mathbf{R}}\}$, the first partial derivative in the rhs of Eq. (3.8) vanishes giving:

$$-\frac{dE_k(\mathbf{R})}{d\mathbf{R}} = -\frac{\partial E[\{\chi_{k,\mathbf{R}}\}, \mathbf{R}]}{\partial \mathbf{R}}. \tag{3.9}$$

Thus the explicit evaluation of the ionic forces in quantum molecular dynamics requires only the knowledge of the occupied eigenstates of the electronic Kohn Sham Hamiltonian. This result is commonly known as the Hellmann-Feynman theorem [10]. Note that the above derivation also holds if we substitute the functional $E[\{\psi\}, \mathbf{R}]$ with the functional $U[\{\psi\}, \mathbf{R}]$ defined in the Sec. 2.2.

3.3 Car-Parrinello quantum molecular dynamics

To integrate the ionic motion in quantum molecular dynamics we can minimize $E[\{\psi\}, \mathbf{R}]$ or $U[\{\psi\}, \mathbf{R}]$ with respect to $\{\psi\}$ to obtain the ground state or an excited electronic state and then we can evaluate the ionic forces using Eq. (3.9). This procedure has to be repeated at each ionic step. The minimized electronic wave-functions at a given step can be used as the starting point for the electronic minimizations at the successive steps. The drawback of this scheme is that the minimization must be very well converged in order to avoid a systematic damping of the ionic motion [11], i.e. a systematic decrease of the constant of motion E_{qmd} (Eq. (3.6)).

An elegant and more efficient scheme is to introduce a fictitious electronic dynamics which keeps, during the ionic motion, the electronic wave-function adiabatically close to the instantaneous eigenstates of the quantum Hamiltonian. To perform a quantum molecular dynamics simulation on the ground state BO energy surface Car and Parrinello proposed to evolve the electronic wave-functions using a fictitious classical Newtonian dynamics [4]. In the Car Parrinello approach the electronic wave-functions are treated as classical fields, where the potential energy is the variational energy functional $E[\psi(t), \mathbf{R}]$. The coupled ionic-electronic Car-Parrinello dynamics is defined by the following equations:

$$M\ddot{\mathbf{R}} = -\frac{\partial E[\{\psi\}, \mathbf{R}]}{\partial \mathbf{R}} \tag{3.10}$$

$$2\mu|\ddot{\psi}_i> = -\frac{\delta E[\{\psi\}]}{\delta|\psi_i>} \tag{3.11}$$

Here μ is a fictitious electronic mass, whose value tunes the speed of the electronic dynamics with respect to that of the ionic dynamics. Note that the Car-Parrinello dynamics conserves the energy:

$$E_{cp} = \mu < \dot{\psi}_i|\dot{\psi}_i> + \frac{1}{2}M\dot{\mathbf{R}}^2 + E[\{\psi\}, \mathbf{R}] \tag{3.12}$$

where $\mu < \dot{\psi}_i|\dot{\psi}_i >$ is a fictitious kinetic energy associated to electrons.

To understand how the Car-Parrinello dynamics can be used to follow adiabatically the ground state during the ionic motion we fist consider the electronic motion at fixed ionic positions. If the wave-function $\{\psi\}$ is close to the minimum of $E[\{\psi\}, \mathbf{R}]$ and the $\{\psi\}$ evolves according to Eq. (3.11) with the ions fixed, the $\{\psi\}$ performs small oscillations around the minimum of $E[\{\psi\}, \mathbf{R}]$. The characteristic frequencies of these oscillations depend both on the energy functional and on the fictitious mass μ. In particular in Ref. [11] (see also Ref. [5] or in the Appendix) it is shown that for a non self-consistent Hamiltonian the lowest eigenfrequency of the fictitious motion ω_{min}^ϵ is equal to:

$$\omega_{min}^\epsilon = \sqrt{\frac{2E_{gap}}{\mu}} \tag{3.13}$$

where E_{gap} is the energy gap separating the lowest unoccupied from the highest occupied electronic level. Now we consider the coupled ionic-electronic Car-Parrinello motion and we chose at the initial time, $t = 0$, a set of wave-functions $\{\psi\}$ close to the minimum of $E[\{\psi\}, \mathbf{R}]$. At $t > 0$ the wave-functions $\{\psi\}$ remain adiabatically close to the instantaneous minimum of $E[\{\psi\}, \mathbf{R}]$. if the lowest eigenfrequency of the fictitious electronic motion ω_{min}^ϵ is much larger than the highest characteristic frequency of the ionic motion ω_{max}^I:

$$\frac{\omega_{min}^\epsilon}{\omega_{max}^I} \gg 1 \tag{3.14}$$

In the Car-Parrinello method a value of the fictitious electronic mass μ has to be chosen in order to satisfy this condition. Once the adiabatic decoupling is satisfied, the average energy transfer between the ionic and the electronic motion is zero. In particular the fictitious kinetic energy $\mu < \dot{\psi}_i|\dot{\psi}_i >$ oscillates around a constant value which is much smaller than the ionic kinetic

energy $\frac{1}{2}M\dot{\mathbf{R}}^2$. This consideration and the conservation of E_{cp} (Eq. (3.12)) imply that energy E_{qmd} (Eq. (3.6)) is conserved without any systematic drift.

The Car-Parrinello dynamics is integrated in time by finite differences using the Verlet algorithm. The technical details of the numerical integration are reported in the Appendix. The integration time step is proportional to the inverse of the maximum electronic frequency ω^ϵ_{max}. In the Appendix we show that, if the wave-functions are expanded using a plane wave basis set, ω^ϵ_{max} is given by:

$$\omega^\epsilon_{max} = \sqrt{\frac{2E_{cut}}{\mu}} \tag{3.15}$$

where E_{cut} is the cut-off energy of the plane wave basis set. Being the ratio $\omega^\epsilon_{min}/\omega^I_{max}$ fixed by the adiabatic decoupling condition, Eq. (3.14). the number N_{cp} of integration step per ionic period is proportional to :

$$N_{cp} \propto \frac{\omega^\epsilon_{max}}{\omega^\epsilon_{min}} = \sqrt{\frac{E_{cut}}{E_{gap}}} \tag{3.16}$$

A way to speed up the Car-Parrinello dynamics is to reduce ω^ϵ_{max} in order to increase the integration time step. The mass preconditioning introduced in Sec. 2.3 in the context of total energy minimization with dynamical methods can be used as well for Car-Parrinello dynamics. By substituting the constant mass μ with the positive mass operator $\hat{\mu}$ defined in Eq. (2.21) the integration time step can be increased by a factor of 2-3 without any computational overload, as shown in the Appendix.

A Car-Parrinello dynamics with the electrons in an excited state is not stable. Indeed, since the excited states are saddle points of $E[\{\psi\},\mathbf{R}]$. in the Car-Parrinello dynamics the wave-functions fall down away from an excited state in the the directions with negative second derivatives. A way to perform a stable Car-Parrinello dynamics with the electron in an excited state is to use the functional $U[\{\psi\},\mathbf{R}]$ defined in Sec. 2.2 in place of the energy functional $E[\{\psi\},\mathbf{R}]$. We note that a Car-Parrinello dynamics based on the functional $U[\{\psi\},\mathbf{R}]$ has been introduce in Ref. [12] in a quantum statistical mechanics context. The mass preconditioning is very useful to speed up a Car-Parrinello dynamics based on the functional $U[\{\psi\},\mathbf{R}]$. By using the mass operator defined in Eq. (2.22) the integration time step can be increased by a factor of 4-9. In the Chapter 4 we present the first application of an excited state Car-Parrinello dynamical simulation.

Finally we note that in a metal the energy gap E_{gap} tends to zero for a cell size going to infinity. In this case a perfect adiabatic separation between the ionic and the electronic motion is not possible. However, as shown in Ref. [13] a satisfactory solution to this problem in the context of Car-Parrinello dynamics can be obtained by using two Nosé thermostats to control separately the respective temperatures of the ions and of the electrons.

Chapter 4

Excited state quantum molecular dynamics: excitonic self-trapping in diamond

Diamond presents an unusually favorable combination of characteristics such as a high mechanical strength. an excellent thermal conductivity, a high optical transparency, a wide electronic band gap, high electron and hole mobilities. and a high resistance to radiation and to temperature. All the above properties, in connection with the recent development of techniques for deposition of thin diamond films, make this material a future candidate for many technological applications. Particularly appealing is the use of diamond in electronic or in opto-electronic devices, as e.g. UV-light emitting devices. Moreover diamond is an ideal material for the construction of windows that operate under high power laser radiation or/and in adverse environments. Point defects with deep electronic levels in the gap have relevant implications in many of these applications. Therefore the possibility to create by light-radiation such a type of defects has to be considered with special interest.

In this Chapter we present a theoretical study on the formation of light-induced intrinsic defects in diamond. In particular we will focus on the phenomenon of self-trapping of excitons. The study of excitonic self-trapping in diamond is interesting also from a fundamental point of view. Up to now the occurrence of excitonic self-trapping was studied mostly in ionic compounds. In these materials self-trapping is always associated with, and often driven by, a charge transfer. It is therefore interesting to see if self-trapping

occurs also in pure covalent materials where there is no charge transfer and where the driving mechanism could be related only to the different bonding character of the valence and conduction bands.

There are experimental and theoretical facts which indicate the occurrence of self-trapping processes in diamond. In particular the nitrogen substitutional donor impurity induces a strong local deformation of the host crystalline lattice [14, 15, 16] which can be interpreted as a self-trapping of the donor electron. Very controversial is the structure of the $1s$ core exciton in diamond [17, 18, 19, 20, 21]. K-edge absorption spectra suggest that the core exciton is weakly bound and of Wannier type [17, 20, 21]. On the contrary emission spectra [21] indicate that the $1s$ core exciton undergoes a self-trapping process similar to that of the nitrogen impurity.

On the other hand, experimental data exclude the self-trapping of a single valence exciton in diamond. Finally no experimental or theoretical investigations were done up to now to identify or to exclude biexcitonic self-trapping in diamond, although simple arguments suggest that biexcitons have a stronger tendency to self-trap than single excitons.

In this Chapter we present a theoretical study of the excited-state Born-Oppenheimer (BO) potential energy surfaces of crystalline diamond within DFT-LDA. To this purpose we applied the ab-initio molecular dynamics scheme discussed in Sec. 3.3, in which the electrons are forced to stay in an arbitrary eigenstate rather than in the ground-state as in the standard Car-Parrinello method. In agreement with the most recent experimental data [21] we found that self-trapping is energetically favorable on the core exciton BO surface. The atomic relaxation associated with self-trapping is qualitatively similar to the one found theoretically for the substitutional nitrogen impurity [16]. Again in agreement with experiments we found that self-trapping is not energetically favorable on the valence exciton BO surface. Finally we predict that self-trapping is energetically favorable on the biexcitonic BO surface. Indeed by minimizing the energy with respect to the ionic positions, we found that two excitons localize themselves on a single crystalline bond which is thus broken. This process is accompanied by a large local relaxation of the lattice, producing a kind of local graphitization.

The Chapter is organized as follows. In Sec. 4.1 we introduce the self-trapping phenomena by presenting a qualitative model for such processes. In Sec. 4.2 we illustrate the theoretical and experimental facts which suggest the occurrence of self-trapping processes in diamond. In Sec. 4.3 we discuss

25

the accuracy of a DFT-LDA description of excitonic self-trapping. In Sec. 4.4 we give the technical details of our calculations. We present the results of DFT-LDA calculation for the core exciton in Sec. 4.5 and for the valence exciton and the valence biexciton in Sec. 4.6. In Sec. 4.7 we describe the ionic and the electronic structure of the self-trapped biexciton and we discuss the experimental implications of our predictions. Sec. 4.8 is devoted to the conclusions.

4.1 A qualitative model of polaronic self-trapping in covalent non polar crystals

In this Section we analyze the driving mechanisms of self-trapping of electrons, holes or excitons in a covalent non polar crystal. In particular, following Ref. [22], we present a simple qualitative model of these processes based on scaling arguments.

We are interested here in insulating non polar crystals such as carbon, silicon or germanium in the diamond structure. In these materials the occupied valence bands and the first conduction bands derive respectively from a bonding and from an antibonding superposition of sp^3 atomic hybrids. We consider the effect of an electronic perturbation on the perfect crystal structure such as the addition of a finite number of electrons and/or holes to the lowest conduction band states or to the highest valence band states respectively. If the ionic positions are frozen, the electronic perturbation extends over the whole crystal. Given the different bonding character of the valence and the conduction bands, the electronic perturbation reduces the bond strength. Thus it is plausible that, once the ions are freed, the system would gain energy by relaxing the ionic structure. However, as we will show with a simple argument below, the energy gain is non-zero only if the electronic perturbation localizes itself on a finite region of space. The localized electronic perturbation is commonly called self-trapped polaron.

The self-trapping energy gain E_{st} due to ionic relaxation can be viewed as resulting from two main contributions with opposite sign: the deformation energy E_{def}, which promotes localization and the quantum confinement kinetic energy E_{kin}, which favors delocalization. When the electronic perturbation contains more than one particle there is also a Coulomb interaction

energy E_{Cou}, whose effect towards localization depends on the relative sign of the particles.

We start by considering the deformation energy E_{def}. We approximate the total energy of a crystal as a sum of independent contributions $\{E_b\}$ each one of which comes from a single bond; we model the energy contribution E_b of a given bond with a function which depends only on the bond length d:

$$E_b = f(d) \qquad (4.1)$$

At the equilibrium distance d_0 the total energy of the crystal is minimum, hence $f'(d_0) = 0$. Now we consider an electronic perturbation spread equally over N bonds and, for simplicity, we ignore interference effects between different bonds. The energy contribution E_b^* of the N perturbed bonds is given by:

$$E_b^* = f(d) + \alpha g(d) \qquad (4.2)$$

where $\alpha = A/N$, A is the total number of electron, holes or excitons which constitute the perturbation, and the function $g(d)$ models the contribution of a hole, an electron or an exciton to E_b. To determine the new equilibrium bond length d_0^* of when α is small we can expand E_b^* around d_0 obtaining:

$$d_0^* - d_0 = -\frac{g'(d_0)}{f''(d_0)}\alpha \qquad (4.3)$$

The deformation energy per bond is then

$$E_b^*(d_0^*) - E_b^*(d_0) = -\frac{g'^2(d_0)}{2f''(d_0)}\alpha^2 = -k_{def}\alpha^2 \qquad (4.4)$$

Recalling that there are N perturbed bonds the total relaxation energy E_{def} is given by:

$$E_{def} = -A^2 k_{def}\frac{1}{N} \qquad (4.5)$$

From this equation it is clear that the more localized is the perturbation the larger is the deformation energy gain. In particular the deformation energy gain is zero if the perturbation is delocalized ($N = \infty$).

The second energy contribution to the self-trapping energy is the kinetic energy associated with quantum confinement. For the Heisenberg uncertainty

27

principle. the energy E_{kin} of A quantum particles localized in a finite volume V is proportional to $AV^{-\frac{2}{3}}$. Since $V \propto N$:

$$E_{kin} = +Ak_{kin}\frac{1}{N^{2/3}} \qquad (4.6)$$

where k_{kin} is a positive constant This energy contribution is positive and larger the smaller is N. Thus the kinetic energy acts against localization.

To study if self-trapping occurs, we minimize the self-trapping energy $E_{st} = E_{def} + E_{kin}$ with respect to N. Since the only stationary point of E_{st} is a maximum, E_{st} reaches its minimum value at one of the two extrema $N = 1$ and $N = \infty$. In particular if $k_{kin} < Ak_{def}$, the minimum occurs for $N = 1$ and the perturbation self-traps on one bond of the system. If $k_{kin} > Ak_{def}$, the minimum occurs for $N = \infty$, and the perturbation does not self-trap. Thus the behaviour of the perturbation with respect to a continuous variation of the physical parameters of the system is discontinuous. Note that, if the perturbation self-traps, it is localized on a single bond.

In the above discussion we neglected the Coulomb interaction energy E_{Cou}. If the perturbation contains more than one particle E_{Cou} contributes to the self-trapping energy. Since the Coulomb potential scales as the inverse of the linear dimension of the charge distribution, $E_{Cou} \propto N^{-1/3}$. The sign of E_{Cou} depends on the relative sign of the charges of the particles which constitute the perturbation. In particular if the perturbation is globally neutral the contribution is negative and favors localization:

$$E_{Cou} = -Ak_{Cou}\frac{1}{N^{1/3}} \qquad (4.7)$$

The perturbation is neutral if the number of electrons is equal to the number of holes. i.e. in the case of excitons. The perturbation is also neutral if the nuclear charge changes in such a way as to neutralize the variation in the electronic charge. i.e. in the case of a substitutional acceptor or donor impurity. Note that for $N \to 0$. E_{Cou} grows less rapidly than E_{def} and E_{kin}. Thus, remembering that a self-trapped perturbation is localized on a single bond, we conclude that E_{Cou} influences the behavior of a self-trapped perturbation less than E_{def} and E_{kin}. In absence of self-trapping, the perturbation produced by a substitutional acceptor, donor or by an exciton is localized on a larger length scale. In this case E_{def} is negligible and the localization

28

length is determined by the competitive and opposite contributions of E_{Cou} and E_{kin} as in a shallow substitutional impurity or in a Wannier exciton.

The model presented in this Section allows the study of the tendency of the perturbation to self-trap as a function of the number of particles A. The deformation energy E_{def} which promotes self-trapping grows as A^2, whereas E_{kin} which favors delocalization grows only as A. Furthermore in the case of a neutral perturbation E_{Cou}, which favors self-trapping grows as A. Since E_{def} increases faster than E_{kin}, the larger is the number of particles in the perturbation the stronger is the probability that the perturbation self-traps. However, note that the number of equal particles that can be accommodated on one bond of the crystal in the same quantum state is limited by the Pauli exclusion principle. Thus no more than two holes or/and two electrons with opposite spins can be localized on one bond of a sp^3 bonded semiconductor.

4.2   Polaronic self-trapping in diamond

In this Section we review the experimental and theoretical facts which suggest the occurrence of self-trapping processes in diamond. In particular we first consider the behaviour of a hole and of an electron due to a donor or to an acceptor substitutional impurity. If self-trapping occurs in these cases it is of "extrinsic" type, since the translational invariance is broken by the defect from the beginning. In addition we discuss the behavior of a core exciton of a valence exciton and of a valence biexciton. If self-trapping occurs in the latter cases it is of "intrinsic" type.

4.2.1   Extrinsic self-trapping

A boron substitutional impurity can be viewed as resulting from the simultaneous subtraction of an electron from the valence bands and of a nuclear charge from a crystal atom. For this defect there is no experimental evidence of extrinsic self-trapping. The hole sits in a shallow acceptor level 0.37 eV above the top of the valence bands [23].

The nitrogen substitutional impurity can be viewed as resulting from the simultaneous addition of an electron to the conduction bands and of a nuclear charge to a crystal atom. Contrary to the acceptor case the extra electron sits in a deep donor level 1.7 eV below the bottom of the conduction bands
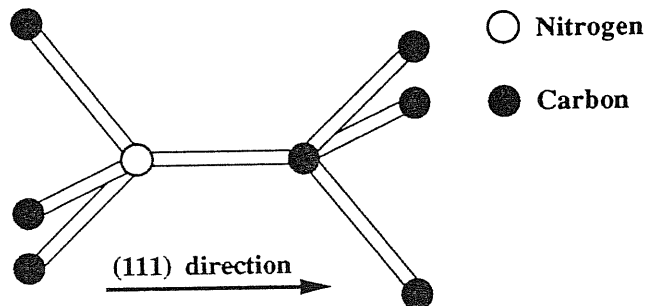
Figure 4.1: Schematic representation of the ideal ionic structure of the substitutional nitrogen impurity.

[24]. Moreover EPR [14] and electron-nuclear double-resonance-technique [15] experiments indicate a symmetry-breaking structural relaxation: the nitrogen atom moves in the $(\bar{1}\bar{1}\bar{1})$ direction (see Fig. 4.1) thus stretching the bond with its nearest-neighbor carbon atom along the (111) direction. The experimental data suggest that this distortion is substantial, $\sim 10\% - 30\%$ of the bond length, and that the donor electron wave-function has most of its amplitude on the nearest carbon atom in the (111) position.

The experimental features associated with the nitrogen impurity are well reproduced in a theoretical calculation based on DFT-LDA [16]. In this calculation it was found that in the relaxation of the defect ionic structure the nitrogen atom and the nearest-neighbor carbon atom in the (111) position move away from each other along the (111) direction. The displacements of the nitrogen atom and of the (111) carbon atom from the ideal positions are equal to 11% and to 14% of the bond length, respectively. The other nearest-neighbor atoms move only by 3%. The relaxation energy, i.e. difference between the the total energy of the relaxed structure and that of the ideal structure, is equal to $-.76$ eV. After the ionic relaxation the donor electron in the antibonding conduction band is localized on the broken bond between the nitrogen and the (111) carbon atom and occupies a level lying 1.9 eV below the bottom of the conduction bands. Thus DFT-LDA reproduces not only the experimental lattice distortion but also the position of the deep donor level in the gap, if the position is measured with respect to the conduction band edge (which is reasonable since the donor level originates mainly from conduction band states). Finally from the ab-initio calculation it turns out

that the symmetry-breaking distortion is not due to a Jahn-Teller effect since in the ideal symmetric structure the donor electronic level is not degenerate.

From the above experimental and theoretical considerations we argue that the nitrogen impurity distortion is due to a self-trapping process. In particular, following the intuitive picture given in the previous Section, the antibonding electron in the conduction band localizes itself on a single bond to maximize the deformation energy gain E_{def}. The localization of the perturbation on one bond is not compatible with the point symmetry of the ideal structure, which is thus broken. The qualitative model presented in the previous Section helps us to understand the different behavior of the the boron acceptor hole, which does not self-trap. Indeed self-trapping occurs if the gain in the deformation energy is larger than the kinetic energy due to quantum confinement. The kinetic energy of an electron or a hole localized on one bond is proportional to the energy width of the sp^3 conduction and valence bands respectively. The experimental width of the diamond valence bands is 24 eV [25]. The width of conduction bands is not known experimentally, but it can be obtained by gw band structure calculations, which give results in agreement with experiments when available. Within gw calculations the width of the conduction bands in diamond is smaller than the width of the valence bands and is equal to 14 eV [26, 27]. Thus the kinetic energy of a strongly localized hole is larger than the kinetic energy of a strongly localized electron.

4.2.2   Intrinsic self-trapping

Now we consider the behavior of excitons in diamond with respect to self-trapping.

Although the diamond 1s core exciton has been the subject of many recent experimental and theoretical investigations [17, 18, 19, 20, 21], a complete agreement on its structure has not yet been reached. In principle the structure of the core exciton should be similar to that of the substitutional nitrogen impurity. Indeed, in an equivalent core approximation, the excited core of carbon can be viewed as a ground-state core of nitrogen and in both cases an antibonding extra electron is present in the conduction bands. However the position of the core exciton peak in the carbon K-edge absorption spectra is only 0.2 eV lower than the conduction band minimum [17, 20, 21], in apparent contrast with the position of the nitrogen impurity deep donor

level, which is instead situated 1.7 eV below the bottom of the conduction band. This has led the authors of Ref. [17] to state that the core exciton is shallow and its energy is reproduced by effective mass theory, implying that the equivalent core approximation does not hold. This conclusion was questioned by the results of a DFT-LDA calculation presented in Ref. [18]. The authors of Ref. [18] argued that the agreement between experiments and effective mass theory was coincidental and that a deeper core exciton state existed which was not observable in dipole transitions. However further experimental investigations [20] did not find the hypothetical dipole-forbidden transition associated with a deep core exciton level. Finally in Ref. [21] a Stokes shift of about 1 eV between the peak position in the X-ray absorption and emission spectra was observed. The authors of Ref. [21] propose the following interpretation for their experimental results: (i) Given the different time scale of the electronic transition and of the ionic motion, during the absorption the atoms can be considered frozen in the ideal lattice positions. In the ideal lattice the core exciton level is shallow. (ii) After the absorption the system gains energy by self-trapping the core exciton: the core exciton is localized on a crystal bond and the lattice relaxes as in the the nitrogen impurity case. (iii) Finally the exciton decays back to the ground state and the photon energy is lower in emission than in adsorption. Indeed the self-trapping ionic relaxation lowers the exciton energy and raises the ground state energy.

In view of the above conflicting experimental and theoretical interpretations we performed a DFT-LDA calculation to help clarifying the situation. Our results, which are presented in Sec. 4.5, support the interpretation given in Ref. [21].

Now we turn our discussion to the valence exciton. There is no experimental evidence for valence exciton self-trapping. The valence exciton is Wannier-like, bound by the Coulomb energy with a binding energy of 0.07 eV [25]. An hypothetical self-trapped valence exciton could be constructed as a superposition of a nitrogen impurity, in which the conduction electron and the ionic distortion are localized on one bond, and a boron impurity, in which the valence hole and the ionic distortion are localized on the same bond. Hence a rough estimate of the valence exciton self-trapping energy would be given by sum of the self-trapping energy of the nitrogen donor, which is negative and favors localization, and the self-trapping energy of the boron acceptor, which is positive and favors delocalization. The experimen-

tal finding that the valence exciton has Wannier character suggests that the tendency of the hole to remain delocalized dominates over the tendency of the electron to self-trap.

Finally the model presented in the previous Section suggests that a valence biexciton has a stronger tendency to self-trap than a single valence exciton. However no experimental nor theoretical investigations were done up to now to identify or to exclude biexcitonic self-trapping in diamond. Motivated by the above considerations we present in the next Sections a theoretical analysis of biexcitonic self-trapping within the DFT-LDA framework. which indeed predicts that self-trapping should occur.

4.3 Excited state quantum molecular dynamics

Since we applied DFT-LDA. i.e. a ground state theory, to excited states some considerations are in order. First we notice that, in the case of finite systems like atoms or small molecules the DFT-LDA total energy differences provide a reasonably good description of the exact excitation energies, if the relaxation of the electronic charge in the self-consistent KS Hamiltonian is fully taken into account. In an extended system the delocalized excitations do not change the KS DFT-LDA Hamiltonian, since the LDA exchange and correlation energy is described by a continuous functional with respect to the density. Therefore the DFT-LDA total energy differences corresponding to delocalized excitations are equal to the differences of the KS DFT-LDA Hamiltonian eigenenergies. Also in the case of extended systems the KS DFT-LDA eigenenergies and eigenfuctions provide a reasonably good approximation to the quasi-particle excitation energies and wave-functions. In semiconductors the main error is on the energy gap between occupied and empty states. which is underestimated by DFT-LDA. The underestimation is due to a discontinuity of the exact DFT exchange and correlation energy with respect to the density. which is not taken into account in the LDA functional.

Excitons are bound states of electrons and holes. In Wannier excitons the long range correlation between the holes and the electrons is responsible for the binding. This long range correlation is missing in LDA. In the case of

self-trapped excitons, which are the subject of the present study, the binding is provided by the ionic distortion, i.e. by the electron-ion potential, which is correctly described by LDA. Moreover, since in the self-trapped excitons the holes and the electrons are localized on the scale of a crystal bond, LDA can provide a good description also for the short range exchange and correlation energy as it does in atoms and in small molecules.

We studied the BO surfaces corresponding to ground state, core exciton valence exciton and valence biexciton.

We performed the DFT-LDA calculations using both the standard energy functional $E[\{\psi\}, \mathbf{R}]$ and the energy functional $U[\{\psi\}, \mathbf{R}]$, defined in Sec. 2.2, whose local minima coincide with the saddle points of $E[\{\psi\}, \mathbf{R}]$. We described the interaction between the ionic cores and the valence and conduction electrons in diamond by a norm conserving pseudopotential [28].

The diamond crystal ground state has two doubly occupied valence levels per atom.

In the case of a core exciton an electron is promoted from the $1s$ atomic core level to the conduction bands. To describe the core exciton BO surface we applied the method presented in Ref. [29]. We generated a norm conserving pseudopotential for an atom of carbon with one electron in the $1s$ core level and five electrons in the valence $2s$-$2p$ levels. The core exciton energy is then the minimum of $E[\{\psi\}, \mathbf{R}]$ in a supercell in which one atom is described by the excited core pseudopotential.

In the case of valence exciton an electron belonging to the highest doubly occupied level of the valence bands is promoted to the lowest empty level of the conduction bands. Hence the energy of the valence exciton is the absolute minimum of the functional $E[\{\psi\}, \mathbf{R}]$ in which two levels are singly occupied.

The valence biexciton is obtained by promoting two electrons from the highest doubly occupied level of the valence bands to the lowest empty level of the conduction bands. In this case we used the functional $U[\{\psi\}, \mathbf{R}]$. Indeed the biexciton is only a saddle point for $E[\{\psi\}, \mathbf{R}]$, since a doubly occupied state has a higher eigen-energy than an empty state. The functional $U[\{\psi\}, \mathbf{R}]$ has many local minima which correspond to different excitations, hence we started the minimization with a trial initial state close to the desired excited state. To this purpose we first computed the highest occupied orbital $|\psi_h>$ of the ground state. Then we obtained the trial initial set of wave-functions by minimizing the functional $E[\{\psi\}, \mathbf{R}]$ in the sub-space orthonormal to $|\psi_h>$. Note that for a non-self-consistent Hamiltonian the

component	α	a	b
loc	3.14960999		
s	5.50708802	17.85441785	-11.09816279
p	3.75969632	-8.90408188	7.12960011

Table 4.1: Parameters of the norm conserving pseudopotential for an excited core carbon atom. The parameters are given in atomic units. The pseudopotential was generated using as reference the $1s^1 2s^2 2p^3$ atomic configuration. The local component of the pseudopotential is equal to $-(5/r)\mathrm{erf}(\alpha_{loc}^{1/2} r)$. The non local components are equal to $(a_l + b_l r^2)\exp(-\alpha_l r^2)$, where the index l indicates s or the p components.

trial state would be the exact excited state.

4.4   Details of the calculation

We used the Bachelet-Hamann-Schlüter norm conserving pseudopotential [28] to describe the interaction between the ground state carbon atom cores and the valence and conduction electrons. As explained in the previous Section, to compute the core exciton BO surface we generated an excited core, norm conserving pseudopotential. To construct the excited core pseudopotential we adopt the Car-von Barth procedure [30]. The parameters of our excited core pseudopotential are reported in Table 4.1. The pseudopotentials were used in a separable form [31] with s-nonlocality only, i.e. the non-local components with angular momentum larger than 1 are taken equal to the p component.

The electronic wave-functions and the density were expanded using a plane-wave basis set with a kinetic energy cutoff of 35 Ry and 140 Ry respectively. These energy cutoffs allow a quite good description of the properties of carbon in different crystalline structures, in the liquid and in the amorphous phases (see e.g. [32]).

We used a periodically repeated simple cubic supercell containing 64 car-

35

bon atoms at the experimental equilibrium lattice constant. For the k-space sampling only the Γ point was considered. In the 64 atom cell at Γ the gap between the valence and conduction bands is 4.0 eV to be compared with 3.5 eV which we obtained with an accurate k-point sampling. The errors introduced by Γ point sampling on structural properties are negligible, e.g the error on the lattice constant is of 0.1%. The self-trapped states are localized on one bond, hence in a 64 atom super-cell they are weakly affected by the boundary condition. Indeed in Ref. [16] the nitrogen impurity was studied with a 64 atom super-cell and a Γ k-point sampling. A more accurate k-point sampling does not change the qualitative physics of the distortion but only increases the self-trapping energy by 0.13 eV [16].

We adopted the damped Newtonian electronic dynamics to minimize the energy functionals $E[\{\psi\}, \mathbf{R}]$ and $U[\{\psi\}, \mathbf{R}]$ with respect to $\{\psi\}$ at fixed ionic positions (see Sec. 2.3). We use the conservative Newtonian electronic dynamics to keep the wave-functions close to the instantaneous minimum of the energy functionals during the ionic motion (see Sec. 3.3) and on a given BO surface we minimized the energy with respect to the ionic position by a damped Newtonian ionic dynamics.

In order to improve the efficiency of the computation we preconditioned the electronic fictitious mass as described in Sec. 2.3. We set the mass preconditioning cut-off energy E_p at 3.5 Ry. The mass preconditioning allowed us to increase the integration time step by a factor of 3 in the fictitious Newtonian dynamics based on the functional $E[\{\psi\}, \mathbf{R}]$ and by a factor of 9 in the fictitious Newtonian dynamics based on the functional $U[\{\psi\}, \mathbf{R}]$.

4.5 Core exciton

4.5.1 Ionic and electronic structure

In this Section we describe the electronic and the ionic structure of the core exciton obtained in the DFT-LDA.

On the lowest BO surface of the core exciton we minimized the energy with respect to the ionic positions. We found that the minimum energy configuration corresponds to an asymmetric distortion of the atomic lattice very similar to that of the nitrogen impurity described in Sec. 4.2. In particular the excited core atom and the nearest-neighbor atom in the (111) position
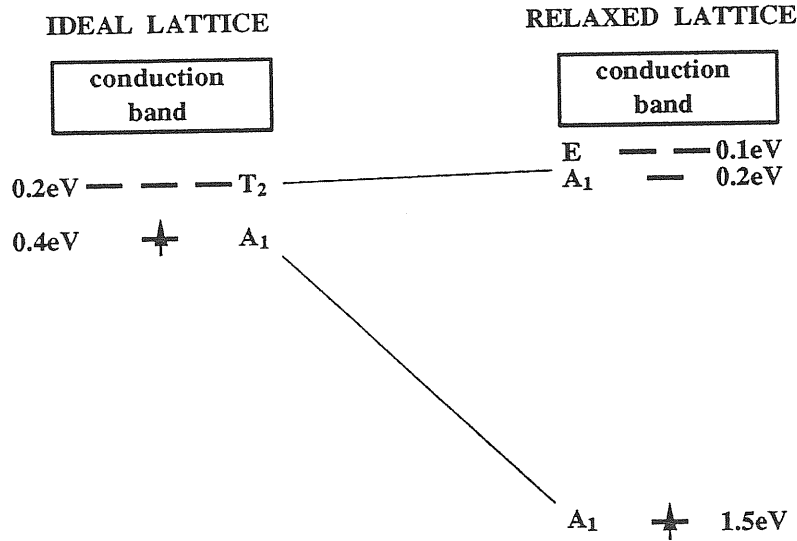
IDEAL LATTICE   RELAXED LATTICE

```
┌──────────────┐              ┌──────────────┐
│  conduction  │              │  conduction  │
│     band     │              │     band     │
└──────────────┘              └──────────────┘

                               E  — —0.1eV
0.2eV — — —T₂ ─────────────    A₁   —  0.2eV

0.4eV    ⥮    A₁

                               A₁    ⥮   1.5eV
```

Figure 4.2: Core exciton levels structure in the ideal and in the relaxed geometry. The energies indicate the distance of the levels from the conduction band edge.

move away one from each other along the (111) direction. The displacements of the excited core atom and of the (111) carbon atom from the ideal sites are equal to 10.4 % and to 11.5 % of the bond length respectively. The other nearest-neighbor atoms move by 2.4 %.

Fig. 4.2 shows the core exciton level structure both for the ideal and for the relaxed geometry. We computed the level structure using the KS Hamiltonian which corresponds to the lowest core-exciton BO surface.

In the ideal lattice the exited core carbon atom induces two defect states in the crystal band gap. The lower state lies 0.4 eV below the bottom of the conduction bands. This state, which in the lowest core-exciton BO surface is occupied by the unpaired electron, is non-degenerate and belongs to the A_1 representation of the T_d point group. The higher state lies 0.2 eV below the bottom of the conduction bands. It is 3-fold degenerate and belongs to the T_2 representation.

The ionic relaxation localizes on the stretched bond the non-degenerate state, which falls down in the gap 1.5 eV below the bottom of the conduction bands. Instead the 3-fold degenerate level remains close to the conduction band edge. However, since the ionic relaxation reduces the symmetry from
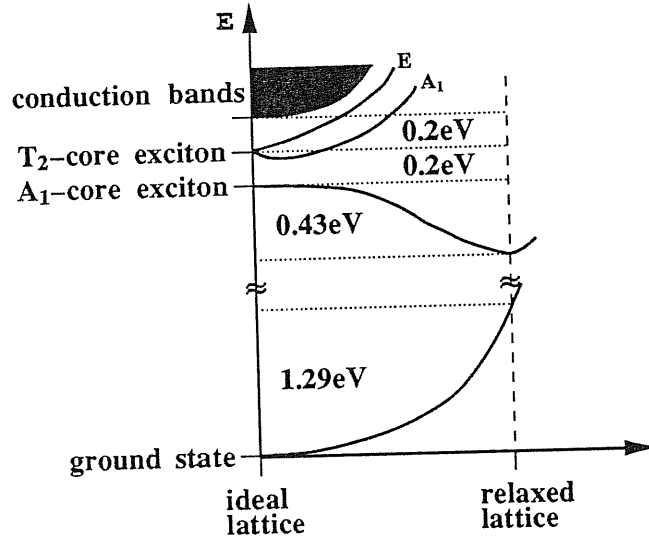
37

Figure 4.3: Configurational diagram of the diamond BO surfaces corresponding to the ground state, to the A_1 and the T_2 core exciton states.

T_d to C_{3v}, the 3-fold degenerate level is split into a 2-fold degenerate level belonging to the E representation of the C_{3v} group and in a non-degenerate level belonging to the A_1 representation (see Fig. 4.2).

Finally in Fig. 4.3 we show the relaxation energy associated with the self-trapping distortion on the different BO surfaces. On the lowest core exciton BO surface the relaxation energy is equal to -.43 eV. On the ground state BO surface the self-trapping distortion increases the energy by 1.29 eV. In Fig. 4.3 the higher core exciton BO surfaces are also shown. Their qualitative features can be deduced just using symmetry arguments and the positions of the KS eigenvalues.

Our calculation indicates that the ionic and the electronic structure of the core-exciton is similar to that of the nitrogen impurity. This proves that the equivalent core approximation holds at least at a qualitative level. However the relaxation energy and especially the distance of the A_1 electron level from the bottom of the conduction band are smaller in the case of the core exciton.

The core exciton level structure with the atoms in the ideal lattice positions was previously computed in DFT-LDA [18], using a linear-combinations-of-atomic-orbitals method and Gaussian orbitals [33]. Hydrogen terminated.

carbon clusters were used to mimic the infinite diamond crystal. The largest calculation was performed with a $C_{29}H_{30}$ cluster. The results of Ref. [18] show that the A_1 and the T_2 levels lies .2 and at .8 eV below the conduction band edge, respectively. This substantially overestimates the spacing between the A_1 and the T_2 levels compared to our calculation. A possible cause of disagreement between our calculation and that of Ref. [18] is the small cluster size used in the latter.

4.5.2 Comparison with experiments

We now show that our results allow to obtain a consistent interpretation of the experimental data of Ref.s [17, 21]. Our model is based on the following steps: (i) During the absorption the ions are in the ideal lattice position. The A_1 level is totally symmetric. Thus a dipole transition from a $1s$ core level to the A_1 valence level is forbidden. The absorption to the T_2 level is instead allowed. In our calculation the T_2 is .2 eV lower than the conduction band edge in agreement with the position the core exciton peak in the X ray absorption spectra [17, 21]. (ii) On the T_2 BO surface the lattice undergoes a Jahn-Teller distortion which lowers the energy up to the avoided crossing with the A_1 level (see Fig. 4.3). (iii) Since the LO phonon energy in diamond (0.16 eV) is comparable with the energy spacing between the A_1 and T_2 energy surfaces, the system can easily perform a non-adiabatic transition from the T_2 to the A_1 level. (iv) On the A_1 level the core exciton self-traps strongly distorting the atomic lattice. (v) The self-trapping distortion induces a Stokes shift in the emitted photon energy. If the ionic relaxation were complete the Stokes shift would be equal (see Fig. 4.3) to the sum of the energy dissipated in the T_2-A_1 non adiabatic transition (.2 eV), of the self trapping relaxation energy (.43 eV) and of the ground state distortion energy (1.29 eV), i.e. to 1.9 eV. In Ref.[21] the shift between the peak position in the X-ray absorption and emission spectra is about 1 eV, but the emission peak shows also a very large sideband which corresponds to Stokes shifts of up to 5 eV. As pointed out in Ref. [21] this large sideband probably indicates an uncompleted relaxation of the atomic lattice to the minimum of the A_1 BO surface. Indeed the core exciton lifetime is expected to be comparable to the phonon period. In this case the atomic lattice would perform only few damped oscillations around the minimum energy structure during the life of the core exciton.
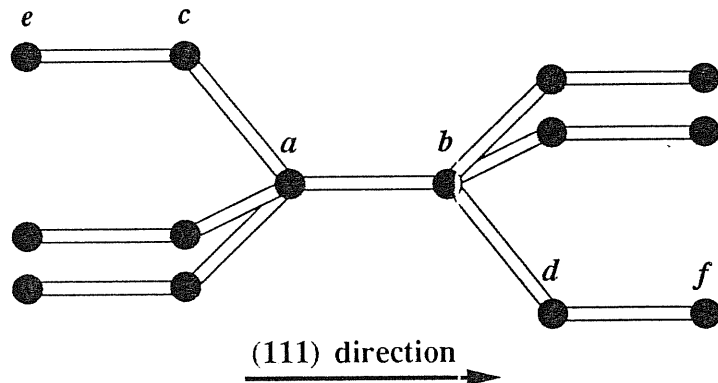
Figure 4.4: Schematic representation of the ideal diamond structure around a crystal bond.

4.6 Valence exciton and biexciton: BO potential energy surfaces

In this Section we describe the DFT-LDA BO potential energy surfaces of the valence exciton and biexciton. To this purpose it is useful to define a configurational coordinate Q as:

$$Q = \frac{d - d_0}{d_0} \tag{4.8}$$

where d is the length of one bond in the supercell along the (111) direction and d_0 is the equilibrium bond distance. In Fig. 4.4 we label the atoms around a crystal bond in the ideal diamond structure. In the following the $(a.b)$-bond, i.e. the bond between the atoms a and b, is used to define the configurational coordinate Q.

First we consider the BO surface corresponding to the valence biexciton. In order to see if self-trapping occurs, we broke the translational symmetry of the ideal structure by giving a symmetric outward displacement along the (111) direction to the a and b atoms. This correspond to a positive value for the Q coordinate. On the biexciton BO surface already a small trial displacement of this type is sufficient to give rise a strong outwards force in the (111) direction which acts to separate the atoms a and b even further. For instance for $Q = 0.048$ the force is equal to 0.024 a.u.. A full
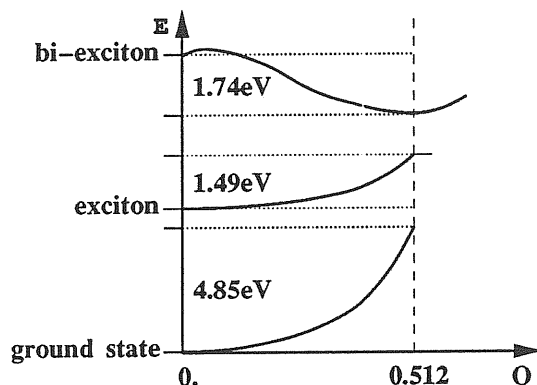
Figure 4.5: Configurational diagram of the diamond BO surfaces corresponding to the ground state the valence exciton and the valence biexciton.

relaxation of the 64 atoms in the super-cell enhances the local distortion and at the minimum Q is equal to 0.512. Thus DFT-LDA predicts self-trapping of the valence biexciton. The self-trapping energy E_{st}, defined as the total energy difference between the relaxed and the ideal ionic structure, is equal to -1.74 eV. Note that E_{st} is much larger than the binding energy of the Wannier excitons (0.07 eV) which is neglected in our treatment.

Then we consider the single exciton BO surfaces. On this BO surface we verified that the energy is minimum when the atom are in the ideal ionic structure. Thus, in agreements with experiments, the valence exciton does not self-trap within DFT-LDA.

Finally we computed how the ionic distortion associated with the biexcitonic self-trapping raises the energy on the ground state and single exciton BO surfaces. We found that the energy obtained with the atoms in the distorted configuration is larger by 4.85 eV and 1.49 eV respectively with respect to the energy obtained with the atoms in the ideal positions. The previous results are summarized in the configurational diagram reported in Fig. 4.5. In the ideal structure, i.e. for $Q = 0$, the three BO surfaces are separated by an energy difference equal to the gap between the valence and conduction bands. In our calculation the gap is equal to 4.00 eV, whereas the experimental gap of diamond is equal to 5.48 eV. It is well known that DFT-LDA underestimate the experimental gaps of semiconductors. A pointed in Sec. 4.3 this underestimation is due to a gap discontinuity of the exact DFT
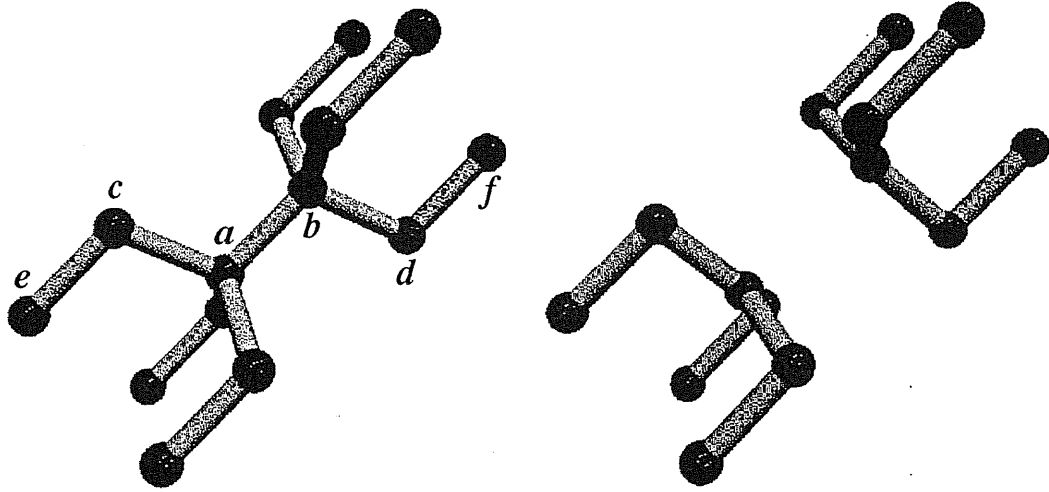
41

Figure 4.6: Ideal and self-trapped biexciton ionic structure. In the self-trapping distortion the displacements of the atoms not shown are smaller than 0.9% of the diamond bond-length.

exchange and correlation energy, which is not taken into account in the LDA. Note that the DFT-LDA energy differences on the same BO surface reported in Fig. 4.5 are reliable since they are not affected by the gap discontinuity, whereas the DFT-LDA energy differences between different BO surfaces have to be corrected for the gap discontinuity. Thus in the subsequent analysis we will use the experimental value of the energy gap.

4.7   Self-trapped biexciton

4.7.1   Ionic and electronic structure

In Fig. 4.6 we compare the ideal and the relaxed ionic structure of the valence biexciton. In the relaxed structure the (a,b)-bond is broken. The a and b atoms connected by the broken bond relax outwards in a symmetric way changing the hybridization of their backbonds from sp^3 to sp^2, i.e. producing a kind of local graphitization.

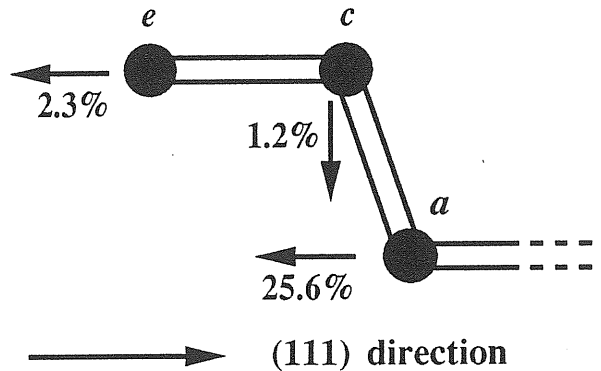In Fig. 4.7 we report schematically the displacements of the atoms around

Figure 4.7: Displacement with respect to the ideal position in unit of bond length in the self-trapped biexciton.

the broken bond in units of the equilibrium bond-length. Only inequivalent atoms are shown. The atoms which are not reported in Fig.s 4.6 and 4.7 move by less then .9%. The displacements of the c atoms decrease the length of the the sp^2 (c,a)-bonds. A perfect planar hybridization and the bond-length of graphite would be realized with a displacement of the a and c atoms in the directions shown in Fig. 4.7 equal to 33.3% and 2.1% respectively to be compared with the actual values of 25.6% and 1.2% of Fig. 4.7. Finally note that the bonds along the (111) direction between the atoms c and e stretch.

In Fig. 4.8 we show the level structure of the biexciton after the ionic relaxation. The two conduction electrons occupy a doubly filled level at 1.7 eV below the bottom of the conduction bands. The empty level of the two holes is situated 1.6 eV above the top of the valence bands. No other deep state falls in the gap during the ionic distortion.

In Fig. 4.9 we show the isocontour plots of the square modulus of the hole and of the electron wave-functions. Both the electron and hole wave-functions are well localized on the broken bond. To give a numerical estimate of the degree of localization we defined I_{loc} as:

$$I_{loc} = \int_{loc} < \psi|\mathbf{r} >< \mathbf{r}|\psi > d^3r \qquad (4.9)$$

where the KS orbitals $|\psi >$ is normalized on the super-cell and the integral is performed inside two spheres of radius 2.5 a.u. centered on the atoms a and b (the equilibrium bond length of diamond is 2.91 a.u.). We computed I_{loc} using

43

```
┌─────────────────┐
│   conduction    │
│      band       │
└─────────────────┘

      1.7eV
      ─↓↑─


      ─────
      1.6eV
┌─────────────────┐
│    valence      │
│      band       │
└─────────────────┘
```
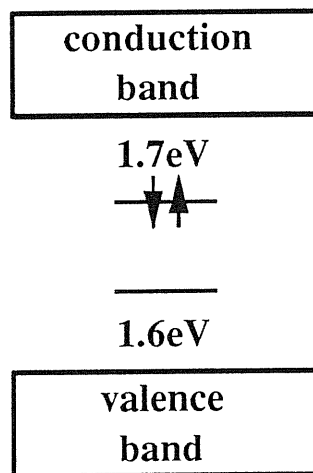
Figure 4.8: Hole and electron deep levels position in the self-trapped biexciton.
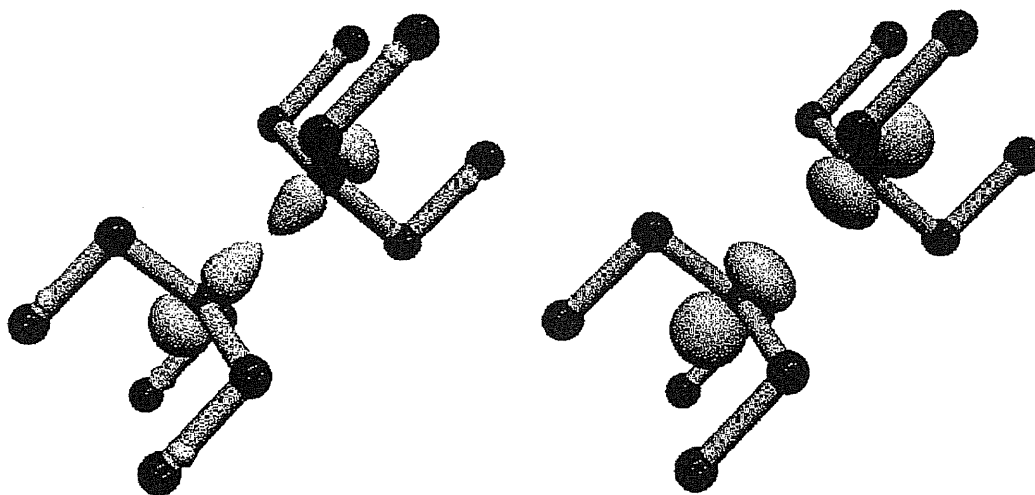

Figure 4.9: Isocontour plots of the the square modulus of the hole (right panel) and electron (left-panel) wave-function. The wave-functions are normalized on the super cell and the isocontour level is equal to 0.01 $(a.u)^{-3}$.
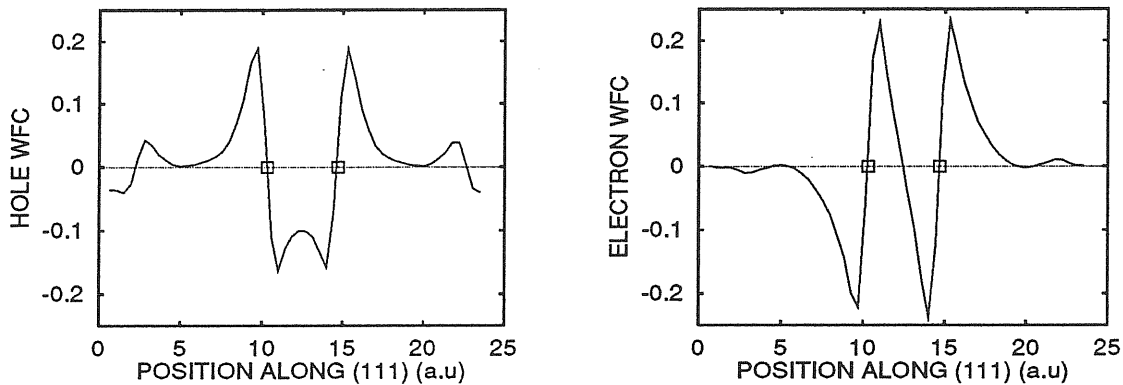
44

Figure 4.10: Hole and electron wave-functions along the (111) direction. The squares show the position of atoms a and b.

the hole and electron excitonic wave-functions. We obtained $I_{loc} = 0.32$ and $I_{loc} = 0.49$ for the hole and the electron respectively. For comparison a typical value for a delocalized valence wave-function would be $I_{loc} \simeq 0.05$. Since the super cell is finite, the I_{loc} of the delocalized state is non zero, nevertheless it is one order on magnitude smaller than the I_{loc} of the localized excitonic states. The values of I_{loc} indicate that in the biexciton the holes are less localized than the electrons. This fact is consistent with the different behavior of the of the boron and of the nitrogen impurities and it can be related to the width of valence and conduction bands as explained in Sec. 4.2. A closer inspection of Fig. 4.9 shows that the hole probability density is mostly localized on the broken bond but has some weaker localization also on the the (111) oriented bonds (e,c). As previously noted these bonds are stretched with respect to the ideal structure.

From Fig. 4.9 the hybridization of the excitonic wave-functions can be deduced. As expected from the local graphitic-like structure of the defect, the hole and the electron states are a superposition of p_z atomic orbitals oriented along the (111) direction. The superposition has bonding or antibonding character for the holes or for the electrons respectively. The symmetry of the exciton states is more clearly seen in Fig. 4.10, where we plot the hole and electron wave-functions along the line connecting the atoms a and b. The wave-functions are zero on the a and b atoms since they are combinations of p atomic orbitals, and the even or odd parity of the wave-functions with
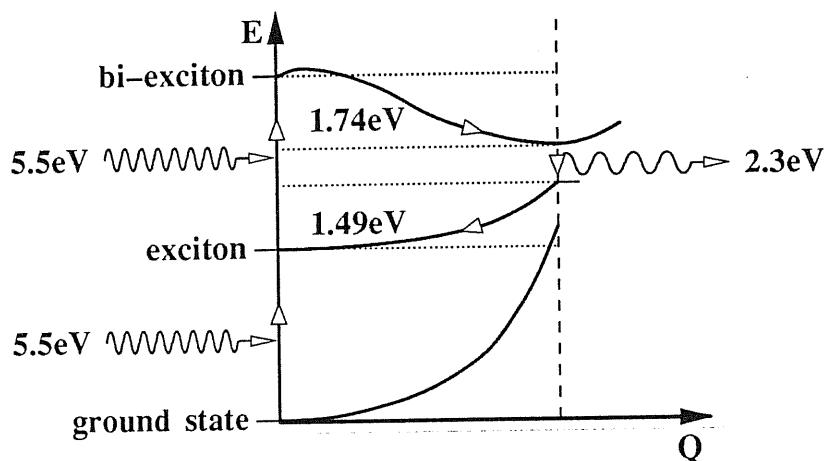
45

Figure 4.11: Stimulated-absorption spontaneous-emission cycle of self-trapping biexciton.

respect to the exchange of the two atoms reflects their bonding or antibonding character.

4.7.2 Experimental implications

Similarly to what it is found in the case of core exciton the first consequence of the valence biexciton self-trapping is a large Stokes shift in the stimulated-absorption spontaneous-emission cycle. This is schematically illustrated in Fig. 4.11. In an optical transition from the excitonic BO surface to the biexcitonic BO surface the energy of the absorbed photon is at least equal to the energy gap of the ideal crystal, i.e. 5.5 eV. On the biexcitonic BO surface the crystal can relax to the self-trapped configuration. This process is accompanied by an energy transfer of 1.74 eV to the ionic degrees of freedom. In the distorted configuration the system decays vertically by spontaneous emission to the excitonic BO surface. On the excitonic BO surface the energy in correspondence of this distorted configuration is 1.49 eV above the minimum. Hence the energy of the emitted photon is equal to $E_{ph} = (5.5\text{-}1.74\text{-}1.49)$ eV $= 2.3$ eV. Then on the excitonic BO surface the system relaxes back to the ideal structure by transferring 1.49 eV to the ionic degrees of freedom.

The gap of diamond is indirect, i.e. the difference Δk between the high-

est valence state k-vector and the lowest conduction state k-vector is non zero. Since the k-vector of a 5.5 eV photon is negligible with respect to Δk, the direct optical absorption at the minimum gap energy is forbidden by the k-vector conservation rule. An allowed photon absorption is then assisted by a simultaneous emission or absorption of a phonon, whose k-vector assures total momentum conservation. For the same reason in the ideal diamond crystal the spontaneous decay of an exciton is phonon assisted and the exciton radiative life time is very long with respect to that of direct gap semiconductors. However, once the biexciton self-traps, the translational symmetry is broken and the direct spontaneous emission becomes allowed. Thus the radiative life time of the self-trapped biexciton is much smaller than the one of the delocalized exciton. The biexciton radiative life time τ in the dipole approximation is given by:

$$\tau = \frac{3}{4} \frac{\hbar^2 c^3 m^2}{e^2 \mathbf{p}^2 \Delta E} \tag{4.10}$$

where c is the speed of light, e and m are the electron charge and mass, $\Delta E = 2.3 eV$ is the emitted photon energy and $\mathbf{p} = <\Psi_{be}|\hat{\mathbf{p}}|\Psi_{ex}>$ is the expectation value of the momentum operator between the biexcitonic and the excitonic total wave-functions. $\mathbf{p}$ can be estimated as:

$$\mathbf{p} = <\psi_e| - \frac{1}{\hbar}\nabla |\psi_h> \tag{4.11}$$

where $|\psi_e>$ and $|\psi_h>$ are the doubly occupied electron level and the empty hole level of the LDA wave-functions of the self-trapped biexciton. With this approximation we eventually obtained $\tau \sim 7$ ns. This time is orders of magnitude smaller than the decay time of the Wannier exciton, nevertheless it is also orders of magnitude larger than the typical time of the ionic relaxation which occurs on the time scale of the phonons, i.e. in fractions of a ps.

Now we discuss the experimental conditions under which it is possible to observe biexcitonic self-trapping. Since the self-trapped biexciton is a fusion of two excitons on one crystal bond, the formation of self-trapped biexciton requires a high excitonic density on a finite region of space. To realize this condition it is possible either to excite directly bond states of Wannier excitons, or to create a high density electron-hole plasma, e.g. by strong light irradiation. In the second case many self-trapped biexcitons could be

produced. This raises some interesting implications. If many self-trapped biexcitons are created, they could cluster on planes producing a macroscopic graphitization. Moreover, since the process of self-trapping is associated with a relevant energy transfer from the electronic to the ionic degrees of freedom in a high density electron hole plasma the self-trapping could heat up the crystal up to melting in fractions of a ps, i.e in the characteristic time of the ionic relaxation. Note that the behavior of the diamond electron hole plasma has technological implications in the design of diamond based electro-optical devices, which could operate under high excitation regime.

Finally we note that recently melting of the GaAs crystal under high laser irradiation have been observed to occur in fractions of a ps [34]. In Ref. [34] this phenomenon have been ascribed to the changing in the binding properties due to the electronic excitations. Our study on diamond suggests that in a sub-picosecond melting experiment the self-trapping could play an important role. We expect that the electron-ion coupling should be smaller in GaAs than in diamond, since, contrary to case of diamond, in GaAs there are no experimental indications of single carrier self-trapping. However in GaAs excitonic self-trapping could be sustained in presence of a high density electron-hole plasma.

4.8 Conclusion

We have shown that there are experimental and theoretical facts which suggest the occurrence of self-trapping process in diamond. In particular the symmetry breaking distortion observed experimentally in the nitrogen impurity can be interpreted as a self-trapping localization of the donor electron. Moreover the occurrence of $1s$ core exciton self-trapping was recently invoked to explained a Stokes shift between the absorption and the emission peaks observed experimentally in the K-edge spectra.

Led by this considerations we have studied the excited-state BO potential energy surfaces of crystalline diamond using an ab-initio molecular dynamics scheme and calculating the electronic structure in the framework of DFT-LDA.

Our calculation reproduces the self-trapping of the core exciton and provides a coherent description of the absorption, self-trapping and emission processes which compares well with the experimental data.

48

Moreover we predict the self-trapping of the valence biexciton. Indeed we have found that, as in the nitrogen impurity and in the core exciton, two excitons localize themselves on a single crystalline bond which is thus broken with a total energy gain of the order of 2 eV. The process is accompanied by a large local relaxation of the lattice, producing a kind of local graphitization. The ionic relaxation implies a strong Stokes shift in the stimulated-absorption spontaneous emission cycle of about 3 eV, which could be observed experimentally. The implications of our finding for the behavior of a high density electron hole plasma in diamond have been discussed.

Chapter 5

Quantum molecular dynamics simulations with linear system-size scaling

The evaluation of the BO potential energy and of the ionic forces for DFT-LDA quantum molecular dynamics requires the knowledge of the occupied eigenstates of the KS Hamiltonian. The occupied eigenstates can be obtained either by self-consistent diagonalization of the KS Hamiltonian or by minimizing the DFT-LDA energy functional $E[\{\psi\}, \mathbf{R}]$ with respect to the wave-functions $\{\psi\}$.

Both self-consistent diagonalization and iterative minimization imply an overall scaling of the computational effort which grows as the third power of the number of electronic states, and thus as the cube of the number of atoms in the systems. This unfavorable scaling is a major limitation to the use of ab-initio DFT-LDA techniques for systems containing more than a few hundred electrons. Simplified quantum approaches such as tight-binding (TB) molecular dynamics [52, 53] still require a computational effort that grows as the cube of the number of atoms, but with a smaller prefactor than in fully self-consistent DFT-LDA calculations. Hence TB molecular dynamics is limited to systems containing up to few thousand electrons.

Let us analyse in detail the computational cost of an electronic energy minimization step. We consider two different approaches for the minimization of the electronic energy: the constrained minimization methods and the unconstrained minimization methods. In the constrained minimization meth-

ods, which we introduced in Chapter 2, the single particle wave-functions are required to be orthonormal at each step of the minimization and the orthonormalization is assured by a set of Lagrangian multipliers. In unconstrained methods the orbitals are allowed to overlap: this requires the evaluation of the inverse of the overlap matrix S among occupied orbitals as an essential ingredient of the calculation [35, 36]. Both constrained and unconstrained methods require the evaluation of $H|\phi_i>$ for the N occupied electronic states giving $O(NM)$ operations, where M is the dimension of the basis set [37]. M is proportional to the number of atoms and thus to N. In constrained methods the coefficients in the equation for the Lagrangian multipliers require the evaluation of N^2 scalar products among the N occupied states for a total of $O(N^2M)$ operations. Then the solution of this equation requires additional $O(N^3)$ operations. In unconstrained methods the calculation of the overlap matrix S and of its inverse requires $O(N^2M)$ and $O(N^3)$ operations, respectively.

The primary reason for the $O(N^3)$ behavior relies on the delocalized character of the wave-functions $|\phi_i>$. If each wave-function could be localized in a finite region of space independent of the system size, the cost of most of the above calculations would be reduced to $O(N)$. The only exceptions are the explicit solution of the equation for the Lagrange multipliers and the evaluation of the inverse of S, which in general are still $O(N^3)$. The idea of forcing the wave-functions to be localized in given regions of space to construct an $O(N)$ scheme was first suggested in Ref. [35] and subsequently applied in Ref.s [38, 39, 40, 41, 42].

The localization constraint does not introduce any approximation if the construction of localized wave-functions amounts to a unitary transformation in the space of the occupied eigenstates. This is the case of a periodic insulator for which exponentially localized Wannier functions can be constructed. In the general case imposing a fixed localization can be considered as a variational approximation for the electronic wave-functions. The accuracy of this approximation can be controlled in a systematic way by varying the size of the localization region.

In order to reduce to $O(N)$ operations also the explicit solution of the equation for the Lagrange multipliers or the evaluation of the inverse of S, in principle one should resort to assumptions on the form of the overlap matrix. For example, if the off diagonal elements of S could be made appropriately small, with respect to the diagonal elements, then the matrix could

be inverted iteratively with a number of operations which is independent of the system size. However the problem of imposing *explicit* orthogonalization constraints or of inverting S can be solved without any assumption or approximation. In fact, one can define a novel unconstrained functional containing only the S matrix but not its inverse. Nevertheless such functional has exactly the same minimum as the Kohn-Sham density functional. This idea was introduced in Ref. [39]. Although this formulation is very general, the scheme has been applied so far only to TB molecular dynamics [39, 42, 43].

Others $O(N)$ methods, not based on the direct evaluation of the occupied orbitals have been proposed in the literature. Such schemes are based instead on the direct calculation either of the one electron Green's function [44] or of the density matrix [46, 47, 49]. Real space localization constraints are used also in these methods to obtain an $O(N)$ scheme. So far these approaches have been applied to TB Hamiltonians. Their generalization to DFT-LDA calculations [45], in which the dimension of the basis set is much larger than the number of occupied states, appears to be very costly since they imply the knowledge of the full spectrum (occupied and empty states) of the Hamiltonian matrix.

In this Chapter we present a detailed discussion of the $O(N)$ method introduced in Ref. [39], following closely a long report [42]. In Sec. 5.1 we introduce the novel unconstrained energy functional. In Sec. 5.2 we discuss numerical results obtained with this functional for first principles calculations within DFT-LDA. In Sec. 5.3 we demonstrate that an algorithm with linear system-size scaling can be obtained when the functional introduced in Sec. 5.1 is minimized with respect to localized orbitals. Sec.s 5.4 and 5.5 contain the results for the minimization of tight binding Hamiltonians and for molecular dynamics simulations, respectively. Summary and conclusions are given in Sec. 5.6.

5.1 An energy functional with implicit orthogonalization constraints

5.1.1 Definition and characterization of the energy functional

In Chapter 2 we have introduced the energy functional used in standard constrained minimization methods. In such methods the single particle wave-functions are orthonormal. In the following we indicate with $\{\psi\}$ a set of orthonormal wave-functions and with $E^{\perp}[\{\psi\}]$ the constrained DFT energy functional defined in Eq. 2.7.

In unconstrained minimization methods the single particle wave-functions are allowed to overlap. In the following we indicate with $\{\phi\}$ a set of overlapping wave-functions and with $\mathbf{S}$ their overlap matrix. In the standard approach (see e.g. [35, 36]), the unconstrained energy functional requires the inverse of $\mathbf{S}$ in the definitions of the kinetic energy and of the density. The absolute minimum of the standard unconstrained functional coincides with that of $E^{\perp}[\{\psi\}]$.

In this Section we present the novel unconstrained functional introduced in Ref. [39]. Its main features are:

(i) It does not require the inverse of the overlap matrix, contrary to the case of the standard unconstrained functional.

(ii) The absolute minimum of the novel unconstrained functional coincides with that of $E^{\perp}[\{\psi\}]$.

(iii) At the minimum the single particle wave-functions are orthonormal.

To prove and to illustrate the above statements we introduce the following notation. We define an energy functional $E[\mathbf{A}, \{\phi\}]$ as:

$$E[\mathbf{A}, \{\phi\}] = 2(\sum_{ij}^{N/2} A_{ij} < \phi_i| -\frac{1}{2}\nabla^2|\phi_j > +F[\tilde{\rho}]) + \eta(N - \int d\mathbf{r}\tilde{\rho}(\mathbf{r})) \quad (5.1)$$

where $\{\phi\}$ are $N/2$ overlapping orbitals, $\mathbf{A}$ is a $(N/2 \times N/2)$ real matrix, $\tilde{\rho}(\mathbf{r}) = \tilde{\rho}[\mathbf{A}, \{\phi\}](\mathbf{r}) = 2\sum_{ij}^{N/2} A_{ij}\phi_j(\mathbf{r})\phi_i(\mathbf{r})$, $F[\tilde{\rho}]$ is the sum of the Hartree, exchange-correlation and external potential energy functionals, and η is a constant to be specified. The factor 2 accounts for the electronic occupation numbers, which are assumed to be all equal. For simplicity we consider real

orbitals. According to the choice of the matrix $\mathbf{A}$ in Eq. (5.1), one can obtain either the standard or the novel unconstrained functionals.

If $\mathbf{A} = \mathbf{S}^{-1}$, where $S_{ij} = <\phi_i|\phi_j>$, we obtain the standard unconstrained functional $E[\mathbf{S}^{-1}, \{\phi\}]$ [35, 36]. In this case $\tilde{\rho}[\mathbf{S}^{-1}]$ is the single particle charge density $\rho(\mathbf{r})$ and the term multiplying η is zero. In particular, if the wavefunctions are orthonormal then $\mathbf{S}^{-1} = \mathbf{I}$, where $\mathbf{I}$ is the identity matrix, and $E[\mathbf{S}^{-1}, \{\psi\}]$ becomes equal to $E^{\perp}[\{\psi\}]$.

In general, it is easy to prove that the absolute minimum of $E[\mathbf{S}^{-1}, \{\phi\}]$ coincides with that of $E^{\perp}[\{\psi\}]$. For this purpose we recall that, if $\mathbf{S}^{-1}$ is not ill defined, then for any given set of overlapping orbitals $\{\phi\}$ it is possible to construct a set of orthonormal orbitals $\{\psi\}$ by using the Löwdin transformation [50], i.e. $\psi_i = \sum_j S_{ij}^{-1/2} \phi_j$. Since $E^{\perp}[\mathbf{S}^{-1/2}\phi] = E[\mathbf{S}^{-1}, \{\phi\}]$, it follows that:

$$\min_{\{\psi\}} E^{\perp}[\{\psi\}] = \min_{\{\phi\}} E[\mathbf{S}^{-1}, \{\phi\}] = E_0. \qquad (5.2)$$

If instead $\mathbf{A} = \mathbf{Q}$, where

$$\mathbf{Q} = \sum_{n=0}^{\mathcal{N}} (\mathbf{I} - \mathbf{S})^n \qquad (5.3)$$

and $\mathcal{N}$ is odd, we obtain the novel unconstrained functional $E[\mathbf{Q}, \{\phi\}]$ introduced in Ref. [39]. $\mathbf{Q}$ is the truncated series expansion of $\mathbf{S}^{-1}$ in powers of $(\mathbf{I} - \mathbf{S})$. We note that similarly to $E^{\perp}[\{\psi\}]$ and $E[\mathbf{S}^{-1}, \{\phi\}]$, $E[\mathbf{Q}, \{\phi\}]$ is invariant under unitary transformations in the subspace of the occupied states.

We now prove the three statements given above concerning the properties of $E[\mathbf{Q}, \{\phi\}]$.

(i) $E[\mathbf{Q}, \{\phi\}]$ *does not require the inverse of* $\mathbf{S}$. This is evident from the definition of $E[\mathbf{Q}, \{\phi\}]$.

(ii) *The absolute minimum of* $E[\mathbf{Q}, \{\phi\}]$ *is* E_0. First we notice that, if the orbitals are orthonormal, then $\mathbf{S} = \mathbf{Q} = \mathbf{I}$. Consequently $E[\mathbf{Q}, \{\psi\}] = E^{\perp}[\{\psi\}]$. In the general case, since $\{\psi\}$ is a subset of $\{\phi\}$, $\min_{\{\psi\}} E[\mathbf{Q}, \{\psi\}] \geq \min_{\{\phi\}} E[\mathbf{Q}, \{\phi\}]$ and therefore:

$$\min_{\{\psi\}} E^{\perp}[\{\psi\}] \geq \min_{\{\phi\}} E[\mathbf{Q}, \{\phi\}]. \qquad (5.4)$$

This shows that E_0 is an upper bound to $\min_{\{\phi\}} E[\mathbf{Q}, \{\phi\}]$.

We now prove that E_0 is also a lower bound. For this purpose let us consider the difference between the functionals $E[\mathbf{Q}, \{\phi\}]$ and $E[\mathbf{S}^{-1}, \{\phi\}]$ i.e.

$$\Delta E = E[\mathbf{Q}, \{\phi\}] - E[\mathbf{S}^{-1}, \{\phi\}] = \int_0^1 \frac{\partial E[\mathbf{A}(\lambda), \{\phi\}]}{\partial \lambda} d\lambda \qquad (5.5)$$

where $\mathbf{A}(\lambda) = \lambda(\mathbf{Q}-\mathbf{S}^{-1})+\mathbf{S}^{-1}$. Using in Eq. (5.5) the definition of $E[\mathbf{A}, \{\phi\}]$ given in Eq. (5.1) we obtain:

$$\Delta E = 2 \sum_{ij}^{N/2} < \phi_j | \overline{H}_{KS} - \eta | \phi_i > (Q_{ij} - S_{ij}^{-1}) \qquad (5.6)$$

where $\overline{H}_{KS} = -\frac{1}{2}\nabla^2 + \overline{V}_{KS}$, with $\overline{V}_{KS} = \int_0^1 d\lambda V_{KS}[\tilde{\rho}(\lambda)]$ and $V_{KS}[\tilde{\rho}] = \frac{\delta F}{\delta \tilde{\rho}}$. Here $\overline{H}_{KS}$ is a Kohn-Sham Hamiltonian, in which the self-consistent potential is averaged over the integration path (λ) of Eq. (5.5). Since in a numerical calculation the wave-functions and the operators are represented in a finite Hilbert space, it is always possible to choose η large enough that the operator $(\overline{H}_{KS} - \eta)$ is negative definite. Then also the ($N/2 \times N/2$) matrix $< \phi_j | \overline{H}_{KS} - \eta | \phi_i >$ is negative definite. Using in the definition of $\mathbf{Q}$ the expression for a sum of a geometric series, we obtain:

$$(\mathbf{Q} - \mathbf{S}^{-1}) = -\mathbf{S}^{-1}(\mathbf{I} - \mathbf{S})^{\mathcal{N}+1} = -(\mathbf{I} - \mathbf{S})^{\mathcal{N}+1}\mathbf{S}^{-1}. \qquad (5.7)$$

If $\mathcal{N}$ is odd, $(\mathbf{Q} - \mathbf{S}^{-1})$ is a non positive definite matrix since $\mathbf{S}$, $\mathbf{S}^{-1}$ and $(\mathbf{I} - \mathbf{S})^{\mathcal{N}+1}$ are commuting non negative definite matrices. Therefore if η and $\mathcal{N}$ fulfill the above requirements, ΔE is non negative since it is equal to the trace of the product of a negative and of a non positive definite matrix. As a consequence, for each set of $\{\phi\}$ it follows that:

$$E[\mathbf{Q}, \{\phi\}] \geq E[\mathbf{S}^{-1}, \{\phi\}]. \qquad (5.8)$$

In this equation the equality sign holds if and only if $(\mathbf{Q} - \mathbf{S})^{-1} = 0$ and therefore if and only if $\mathbf{S} = \mathbf{I}$. Eq.(5.8) shows that E_0 is a lower bound to $\min_{\{\phi\}} E[\mathbf{Q}, \{\phi\}]$.

From Eqs. 5.2, 5.4 and 5.8 we have

$$\min_{\{\psi\}} E^{\perp}[\{\psi\}] = \min_{\{\phi\}} E[\mathbf{Q}, \{\phi\}] = \min_{\{\phi\}} E[\mathbf{S}^{-1}, \{\phi\}] = E_0. \qquad (5.9)$$

This proves that *the energy functional $E[\mathbf{Q}]$ has the Kohn-Sham ground state energy (E_0) as its absolute minimum*, if η and $\mathcal{N}$ fulfill the requirements discussed above.

(iii) *At the minimum of $E[\mathbf{Q}, \{\phi\}]$ the single particle wave-functions are orthonormal.* As discussed in the previous point, if $\{\phi\}$ are not orthonormal, then $E[\mathbf{Q}, \{\phi\}] > E[\mathbf{S}^{-1}, \{\phi\}]$. Thus, if the wave-functions which minimize $E[\mathbf{Q}, \{\phi\}]$ are not orthonormal, then $\min_{\{\phi\}} E[\mathbf{Q}, \{\phi\}] > \min_{\{\phi\}} E[\mathbf{S}^{-1}, \{\phi\}]$. This is in contrast with Eq. (5.9). Hence it follows that *the minimization of $E[\mathbf{Q}]$ yields orthonormal orbitals.*

The choice of η which makes $(\overline{H}_{KS} - \eta)$ negative definite deserves some comments. If the Hamiltonian of the system does not depend on ρ, a value for η larger than ϵ_{max}, i.e. the maximum eigenvalue of the Hamiltonian, insures that $\Delta E \geq 0$. Within LDA, one can prove that

$$H_{KS}[\hat{\rho}[\mathbf{Q}]] \leq H_H[\rho], \qquad (5.10)$$

where $H_H[\rho] = [-\frac{1}{2}\nabla^2 + V_H[\rho] + V_{ext}]$, V_H and V_{ext} are the Hartree and external potential, respectively, and $\rho = \hat{\rho}[\mathbf{S}^{-1}]$. This follows from the property $\hat{\rho}[\mathbf{Q}](\mathbf{r}) \leq \rho(\mathbf{r})$, valid for each point $\mathbf{r}$, and from the explicit LDA expression of the exchange and correlation energy as a function of $\rho(\mathbf{r})$. Within, e.g., a plane wave implementation with a finite cutoff, H_H has an upper bound. This insures the existence of η such that $\Delta E \geq 0$. However in practical calculations one can choose η smaller than the upper bound of H_H; indeed for practical purposes it is not necessary to require E_0 to be the absolute minimum of $E[\mathbf{Q}]$, but it is sufficient to require it to be a local minimum of $E[\mathbf{Q}]$; the constant η which fulfills this weaker condition is in general much smaller that the upper bound of H_H, as we will discuss in the next Section.

5.1.2   Iterative minimization of the energy functional

In this Section we discuss the choices of η appropriate in practical applications and the convergence rate of iterative minimizations of $E[\mathbf{Q}]$ with $\mathcal{N} = 1$, compared to that of $E^\perp$. For non self consistent Hamiltonians, we will show that if η is larger than the Fermi energy, then E_0 is a local minimum of $E[\mathbf{Q}]$; furthermore if a value of η is chosen, which is close to the Fermi energy, the minimum of $E[\mathbf{Q}]$ and that of $E^\perp$ can be obtained with the same computational efficiency.

The asymptotic convergence rate of iterative minimizations of a functional $E[\{\phi\}]$ can be estimated by expanding it around its minimum E_0, up to second order in the variation of the wave-functions $\{\phi\}$. As discussed, e.g., in the Appendix, in the minimization asymptotic regime the number of integration steps to reach convergence is directly related to the ratio between the maximum and the minimum eigenvalues of the quadratic form which results from the second order expansion of $(E - E_0)$.

We consider a non self-consistent Hamiltonian (H) and we relate its eigenvalues $(\{\epsilon\})$ to those of the quadratic expansion of $(E[\mathbf{Q}] - E_0)$. Since $E[\mathbf{Q}]$ is invariant under unitary transformations in the subspace of occupied states, a generic variation of the wave-function with respect to the ground state can be written as :

$$|\phi_i> = |\chi_i^0> + |\Delta_i>, \tag{5.11}$$

with

$$|\Delta_i> = \sum_{l \in [\mathcal{TOT}]} c_l^i |\chi_l^0> . \tag{5.12}$$

Here $|\chi_l^0>$ are the eigenstates of H, and the indices i and l belong to the set of occupied states and to the set of occupied plus empty states, respectively. We denote with $[\mathcal{OCC}]$ and $[\mathcal{EMP}]$ the sets of occupied and empty states, and with $[\mathcal{TOT}]$ the union of the two sets. c_l^i are expansion coefficients of $|\Delta_i>$ over the eigenstates of H. If Eq. 5.11 is substituted into the expression of $\Delta E = E[\mathbf{Q}] - E_0$, the first order term vanishes, showing that for each value of η the orbitals $|\chi_i^0>$ make $E[\mathbf{Q}]$ stationary. The stationary point is in particular an absolute minimum if $\eta \geq \epsilon_{max}$, as shown in the previous Section. One is then left with a second order term, which can be recast as follows:

$$\Delta E = \sum_{m \in [\mathcal{EMP}]} \sum_{i \in [\mathcal{OCC}]} 2[\epsilon_m - \epsilon_i](c_m^i)^2 + \sum_{ij \in [\mathcal{OCC}]} 8[\eta - \frac{(\epsilon_i + \epsilon_j)}{2}][\frac{1}{\sqrt{2}}(c_j^i + c_i^j)]^2 \tag{5.13}$$

From Eq. 5.13 it is seen that the quadratic form ΔE has two sets of normal modes. The first set has eigenvalues $k_{(mi)} = 2[\epsilon_m - \epsilon_i]$, which are always positive and independent of η; they correspond to the coordinates c_m^i. These modes are associated with an increase of the total energy when the orbitals acquire non zero components on empty eigenstates of H. They are the same as the normal modes of $(E^\perp - E_0)$, calculated in Ref. [11]. The second set

57

of normal modes of ΔE has eigenvalues $\bar{k}_{(ij)} = 8[\eta - \frac{(\epsilon_i + \epsilon_j)}{2}]$; they correspond to the coordinates $[\frac{1}{\sqrt{2}}(c_j^i + c_i^j)]$. These modes are associated with a change of $E[\mathbf{Q}]$ due to the overlap of the electronic wave-functions; they are indeed associated with the orthogonality constraints implicitly included in the definition of $E[\mathbf{Q}]$ and they are not present in $(E^\perp - E_0)$.

For η larger than the highest occupied eigenvalue of H, $\epsilon_{N/2}$ (i.e. the Fermi energy), the $\bar{k}_{(ij)}$ are positive and thus E_0 is a local minimum of $E[\mathbf{Q}]$. $\eta \geq \epsilon_{N/2}$ is a weaker condition than the one required to prove Eq. (5.9); it is however a sufficient condition to insure that the minimization of $E[\mathbf{Q}]$ leads to the correct ground state energy, provided a reasonable starting point for the minimization is chosen. This will be shown also with numerical examples in the next Section.

The minimizations of $E[\mathbf{Q}]$ and $E^\perp$ can be obtained with the same efficiency provided the weaker condition on η is adopted. For example one can choose $\eta \simeq \epsilon_{N/2+1}$. Under such a condition the ratio between the maximum and the minimum eigenvalues of the expansion of $(E[\mathbf{Q}] - E_0)$ and of $(E^\perp - E_0)$ is the same in most systems. Indeed the eigenvalues $\bar{k}$ lie in the interval defined by the eigenvalues k, if the spread in energy of the excited states of H is four times smaller than the valence band width. This condition is satisfied in most systems of interest. This means that in practice iterative minimizations of $E[\mathbf{Q}]$ and MD simulations with $E[\mathbf{Q}]$ can be performed with the same efficiency as the corresponding calculations with $E^\perp$. However, if η is chosen so that E_0 is an absolute minimum of $E[\mathbf{Q}]$, the time step used in MD simulations, which is proportional [11, 5] to the square root of the maximum eigenvalue of ΔE (Eq. 5.13), is reduced by a factor of two with respect to that used in standard calculations.

The functional $E[\mathbf{Q}]$ has clear advantages over standard energy functionals when conjugate and preconditioned conjugate gradient minimization procedures are used: the complication of imposing orthonormality constraints is avoided, and contrary to ordinary unconstrained methods an automatic control of the $\mathbf{S}$ matrix is provided, since at the minimum $\mathbf{S} = \mathbf{I}$. Furthermore, when the mass preconditioning introduced in Sec. 2.3 is used, the integration of the electronic equation of motion does not imply any extra work, at variance with integration schemes with explicit orthogonalization constraints.

5.1.3 Relationship with other functionals

The total energy minimization scheme which we introduced in Ref. [39] is related to other approaches recently proposed in the literature for electronic structure calculations with linear system-size scaling. In particular Ordejón et al. [41] derived the same functional as that of Eqs. 1 and 3 for $\mathcal{N} = 1$ for non self-consistent Hamiltonians. Their derivation is based on a Lagrangian formulation with explicit orthogonalization constraints, where the Lagrange multipliers (λ_{ij}) are approximated by an expression which is exact only at the minimum, i.e. $\lambda_{ij} = <\phi_i|H|\phi_j>$. The approach presented by Ordejón et al. [41] is similar to that of Wang and Teter [38], although in Ref. [38] constraints are introduced by means of a penalty function. However the minimum of the Wang and Teter functional is E_0 only if the weight of the penalty function goes to infinity, at variance with our and Ordejón et al.'s functionals which at the minimum is always equal to E_0.

Instead of using an orbital formulation, Li, Nunes and Vanderbilt [46] and Daw [47] proposed a functional for total energy minimizations within a density matrix formulation. In this case one minimizes the energy functional with respect to the density matrix, which must fulfill the idempotency condition. This condition is enforced by minimizing the total energy with respect to a *purified* version of the density matrix [46, 51] ($\tilde{\rho}(r, r')$), constructed from a trial density matrix $\rho(r, r')$ in such a way that its eigenvalues lie on the interval [0,1]. The energy functional $E[Q]$ (Eq. 1,3) for non self-consistent Hamiltonians can be re-derived within the formulation of Ref. [46] if $\rho(r, r')$ is expressed in terms of the occupied single particle wave-functions, i.e. $\rho(r, r') = \sum_{i \in [occ]} \phi_i(r)\phi_i(r')$, and a purification transformation is chosen such that $\tilde{\rho} = I - (I - \rho)^{\mathcal{N}+1}$. This transformation forces the eigenvalues of $\tilde{\rho}$ to be less than 1 only if $\mathcal{N}$ is odd; one does not need to force the eigenvalues to be positive, as done in Ref. [46], since by construction $\rho(r, r') = \sum_{i \in [occ]} \phi_i(r)\phi_i(r')$ has a number of non zero eigenvalues equal to the number of occupied states.

5.2 Numerical results of first principles calculations

The validity of the minimization scheme presented in Sec. 5.1 was tested numerically for KS Hamiltonians within LDA, by computing the ground state energy of Si in the diamond structure. We used an expansion coefficient $\mathcal{N} = 1$ to define the $\mathbf{Q}$ matrix entering the energy functional (see Eq. 3). We chose η smaller that the maximum eigenvalue of H_{KS}; this choice insures the iterative minimization to properly converge to the ground state energy E_0, unless a pathological starting point for the electronic orbitals is chosen.

$E[\mathbf{Q}]$ was minimized by steepest descent; the derivative of the functional with respect to the single particle orbitals is given by:

$$\frac{\partial E[\mathbf{Q}]}{\partial \phi_i} = 4 \sum_j^{N/2} [(H_{KS} - \eta)|\phi_j > (2\delta_{ji} - S_{ji}) - |\phi_j >< \phi_j|(H_{KS} - \eta)|\phi_i >]$$

(5.14)

The orbitals were expanded in PW with a kinetic energy cutoff (E_{cut}) of 12 Ry and the interaction between ionic cores and valence electrons was described by a norm conserving pseudopotential [28] expressed in a separable form [31]. The calculation was started from orbitals set up from random numbers, with η set at 3.0 Ry above the top of the valence band. In Fig. 5.1 we report $E^{\perp}$ and $E[\mathbf{Q}]$ as a function of the number of iterations; it is seen that the minimizations of the two functionals require the same number of iterations and leads to the same energy. Fig. 5.2 shows the integral of the charge density during the minimization procedure. For $\mathcal{N} = 1$, $\Delta N = N - \int dr \tilde{\rho}(\mathbf{r}) = N - Tr(\mathbf{QS})$ is given by

$$\Delta N = Tr((\mathbf{I} - \mathbf{S})^2).$$

(5.15)

This is a positive quantity which goes to zero as the orbitals become orthonormal. In our calculation the difference ΔN between the total number of electrons and the integrated charge reaches a value very close to zero ($\simeq 10^{-6}$) after 10 iterations, showing that the single particle wave-functions are orthonormal already well before reaching the minimum.
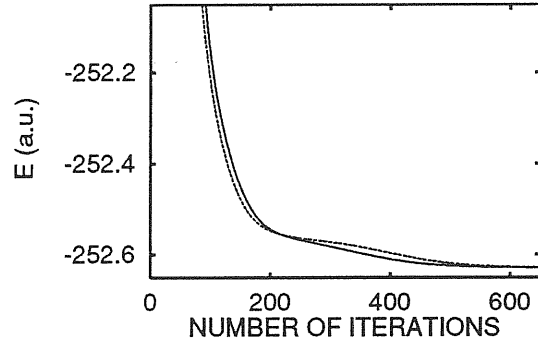
60

Figure 5.1: Total energy (E) as a function of the number of iterations for a steepest descent minimization of 64 Si atoms in the diamond structure, described within LDA with a PW basis set. The solid and dotted lines correspond to the minimization of $E[\mathbf{Q}]$ and $E^{\perp}$ (see text), respectively. $\mathbf{Q}$ was defined with $\mathcal{N} = 1$. Each run was started from the same set of random Fourier coefficients.
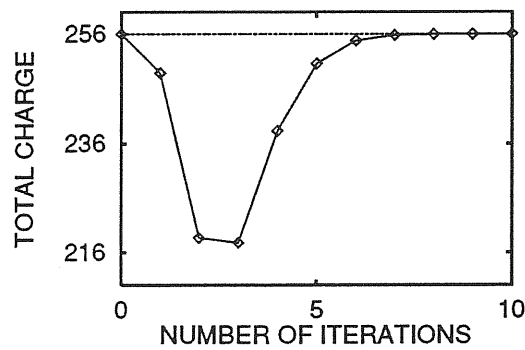

Figure 5.2: Total electronic charge as a function of the number of iterations for the energy minimizations reported in Fig. 5.1. The total number of electrons in the system is 256.

5.3 Localized orbitals and an algorithm with linear system-size scaling

We now turn to the discussion of the approach introduced in Sec. 5.1 within a localized orbital (LO) formulation [35]. Within such a formulation, each single particle wave-function is constrained to be localized in an appropriate region of space, which we call localization region (LR): the electronic orbitals are free to vary inside and are zero outside the LR. Different single particle orbitals can be associated to the same LR, e.g. two doubly occupied orbitals per LR for C and Si, which have four valence electrons. The extension of a LR is determined by the bonding properties of the atomic species composing the system, and it is the same unrespective of the size of the system which is simulated. The choice of the centers of the LRs is arbitrary. In all of our calculations (see next Section) we centered the LRs on atomic sites; this choice is physically unbiased, i.e. it can be adopted for a generic system whose bonding properties are totally unknown, and allows for a solution which satisfies charge neutrality conditions. If one wants to take advantage of known properties of the system, LRs can for example be centered on atomic bonds or on positions compatible with the symmetry of the Wannier functions, if these can be defined. This is however difficult to do, e.g. at each step of a MD simulation, where the evolution of the bonding properties as a function of time is not known. One could also treat the centers of the LRs as variational parameters and optimize their locations during the calculation.

We now consider the minimization of $E[\mathbf{Q}]$ with respect to LO ($\{\phi^L\}$). When the orbitals are localized, S_{ij}, and $< \phi_i^L | H_{KS} | \phi_j^L >$ are sparse matrices which have non zero elements only if i and j belong to overlapping LRs. The evaluation of $E[\mathbf{Q}]$ (Eqs. 1,3) as well as of $\frac{\partial E[\mathbf{Q}]}{\partial \phi_i^L}$ (Eq. 12) implies only the calculation of matrix products containing S_{ij} and $< \phi_i^L | H_{KS} | \phi_j^L >$. No orthogonalization or $\mathbf{S}$ inversion is needed. Thus at each step, the minimization of $E[\mathbf{Q}]$ can be performed with a number of operations which is proportional to the system size.

When localization constraints are imposed, the variational freedom of the minimization procedure is reduced. The energy obtained by minimizing a functional with respect to LOs is then larger than the absolute minimum (E_0) obtained with no constraints on the single particle wave-functions. In particular, the minimum of $E[\mathbf{Q}]$ with respect to LO $\{\phi^L\}$ does not coincide

with that of $E[\mathbf{S}^{-1}]$, and the LO which minimize $E[\mathbf{Q}]$ are in general not orthonormal. This is easily seen as follows. Whereas Eq. 5.4 and 5.8 hold also for LO, Eq. 5.2 is no longer valid when localization constraints are imposed. Indeed the transformation from $\{\psi\}$ to $\{\phi\}$ with $\mathbf{S}^{-1/2}$ does not preserve the size of the LR, i.e. it does not map functions localized in a given region onto functions localized in the *same* region of space. Therefore Eq. 5.9 does not hold but is replaced by

$$\min_{\{\psi^L\}} E^\perp \geq \min_{\{\phi^L\}} E[\mathbf{Q}] \geq \min_{\{\phi^L\}} E[\mathbf{S}^{-1}] \geq E_0, \qquad (5.16)$$

where the LR for the $\{\psi^L\}$ and $\{\phi^L\}$ are the same. Since in Eq. (5.16) the equality is in general not satisfied, at the minimum $\mathbf{S}$ is different from $\mathbf{I}$, contrary to the case of extended orbitals.

The variational quality of the results obtained by minimizing $E[\mathbf{Q}]$, i.e. the difference $[\min_{\{\phi^L\}} E[\mathbf{Q}] - E_0]$, depends upon (i) the order $\mathcal{N}$ chosen for the definition of the $\mathbf{Q}$ matrix and (ii) the size of the LR. For $\mathbf{S} \leq 2\mathbf{I}$, it is easy to see that $E[\mathbf{Q}(\mathcal{N} - 2)] \geq E[\mathbf{Q}(\mathcal{N})]$. Therefore by increasing $\mathcal{N}$ in the definition of $\mathbf{Q}$, one obtains an improvement of the total energy. This leads as well to an increase of the number of operations needed in the computation of $\mathbf{Q}$ (see Eq. 3). Most importantly, in order to improve the quality of the results one can choose to increase the size of the localization region. We note that the number of non zero elements of $\mathbf{S}$ is proportional to $n_{LR}N$, where n_{LR} is the average number of regions overlapping with a given one. Instead the number of degrees of freedom needed to define the $N/2$ single particle orbitals is proportional to mN, where m is the number of points belonging to a LR, e.g. the number of points where the wave-function is non zero. The ratio n_{LR}/m strongly depends on the basis set chosen to set up the Hamiltonian. The optimal choice of $\mathcal{N}$ and of size of the LRs, e.g. of the parameters determining the efficiency and accuracy of the computation, crucially depends upon the chosen basis set.

In calculations where $m \gg n_{LR}$, the computer time for the $\mathbf{S}$ inversion amounts to a small fraction of the total time also for relatively large systems (e.g. systems with up to a few thousand electrons in LDA calculations with PW basis). On the contrary for computations with small basis sets, such as those with TB Hamiltonians, the computer time for the $\mathbf{S}$ inversion constitutes a considerable part of the total time already for small systems (i.e. containing a few tens of atoms).

5.4 Minimization of TB Hamiltonians

The LO formulation was tested numerically using TB Hamiltonians [52, 53] with the convention $\varepsilon_s + \varepsilon_p = 0$. We performed calculations for Si and C in different aggregation states. In calculations for crystalline structures, we considered non zero hopping terms only between first neighbors. We chose a number of LRs equal to the number of atoms and we centered each LR at an atomic site (I). In a TB picture a LR can be identified with the set of atoms belonging to it. For each site I, we label the set of atoms which belong to a LR with LR_I. C and Si atoms have four valence electrons and there are two doubly occupied states for each atom in the system. We then associated two states to each LR: The two wave-functions of the LR centered in I have non zero components on the atoms belonging to the set LR_I and zero components (expansion coefficients) on the atoms which do not belong to LR_I. The expansion coefficients of the single particle orbitals are treated as variational parameters in our calculations. The total number of expansion coefficients grows linearly with the size of the system.

We tested two different shapes of the LR. In one case an atom is defined as belonging to LR_I if its distance to the site I is less than or equal to a given radius r_c (in other words, an euclidean metric is used to define the shape of the LR). In the second case, we took advantage of the form the TB Hamiltonian and we considered an atom as belonging to LR_I if it is connected to the site I by a number of non zero hopping terms less than or equal to a given number of shells N_h.

In all calculations $E[\mathbf{Q}]$ was minimized with respect to ϕ_L by a conjugate gradient (CG) procedure. The gradients $\frac{\partial E[\mathbf{Q}]}{\partial \phi_i^L}$ are simply obtained by projecting Eq. (12) onto the LR where ϕ_i^L is defined. For non self-consistent Hamiltonians, the line minimization required in a CG procedure reduces to the minimization of a quartic polynomial in the variation of the wave-function, along the conjugate direction. In our calculation the line minimization is performed exactly by evaluating the coefficients of the quartic polynomial.

We found that when localization constraints are imposed, $E[\mathbf{Q}]$ can have local minima and metastable states, where the system may be trapped for a long time during the minimization procedure, before reaching a minimum. This problem can be overcome if an appropriate choice of the initial guess
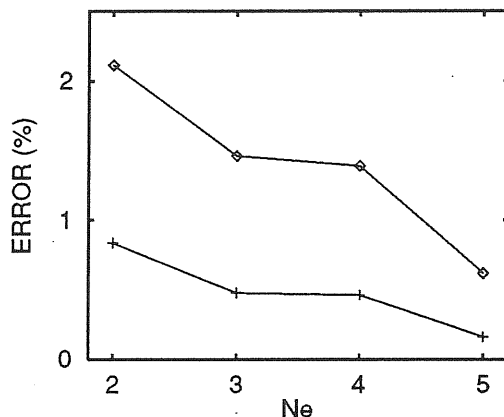
Figure 5.3: Percentage error on the cohesive energy of Si (diamond structure) as a function of the number of shells (N_e) in the localization region, computed with a TB Hamiltonian (see text). Diamonds and crosses refer to minimizations of $E[\mathbf{Q}]$ with $\mathbf{Q}[\mathcal{N} = 1]$ and $\mathbf{Q}[\mathcal{N} = 3]$, respectively. The LRs were defined using an euclidean metric (see text). The errors were evaluated with respect to a computation with extended orbitals.

for the iterative diagonalization is made. In all of our calculations we used starting wave-functions with non zero components only on the site I where they were centered; furthermore orbital components were the same for each I. This choice allowed to avoid local minima and metastable state traps for a wide class of ionic configurations. The problem of being trapped in metastable states or local minima involves only electronic minimizations; it does not concern MD simulations, where the ground state orbitals of a given step can be used as guess wave-functions for the following step.

Fig. 5.3 shows the percentage error on the cohesive energy E_c of Si in the diamond structure, as a function of the size of the LR, computed with respect to a calculation performed with extended orbitals. All computations were carried out at the same fixed volume, with 216 atom supercells, simple cubic periodic boundary conditions and the Γ point only for the supercell Brillouin zone (BZ) sampling. E_c was evaluated with $\mathbf{Q}[\mathcal{N} = 1]$ and $\mathbf{Q}[\mathcal{N} = 3]$ and with $\eta = 3$ eV. The shape of the LR was first chosen using an euclidean metric. We denote with N_e the number of shells included in a LR, defined according to such a metric. It is seen that E_c converges rapidly as a function

of N_e, with both $\mathcal{N} = 1$ and 3. Already with $N_e = 2$ (17 atoms belong to a LR) the results are very good, i.e. E_c is higher than the result obtained with extended orbitals by only 2.1% and 0.8% for $\mathcal{N} = 1$ and 3, respectively. For $\mathcal{N} = 1$, the error on the total charge ΔN (see Eq. 13) which gives the deviation from orthonormality due to localization constraints is in general very small; already for $N_e = 2$ we found it to be 0.2%. We note that when going from $N_e = 3$ (29 atoms in a LR) to $N_e = 4$ (35 atoms in a LR), we obtained the smallest variation of E_c. Indeed the atoms added to a LR when including also the fourth neighbor shell are not connected by hopping terms to those defining a LR when $N_e = 3$. This suggests that a definition of LR based on hopping terms is more physical than one based on the euclidean metric. We repeated the calculations with $\mathcal{N} = 1$ by choosing the LRs according to the hopping parameters and by setting the number of hopping shells N_h at 3. (For the diamond lattice, the definition of LRs using the two metrics are different for N_h and N_e larger than two). The choice $N_h = 3$ amounts to considering 41 atoms in a LR. The percentage error (0.7 %) on E_c is very close to that obtained with $N_e = 5$ (0.6 %), although the number of atoms in a given LR is bigger (47). The choice of the shape of the LRs according to the hopping parameters is superior to that of the euclidean metric and it is especially so when energy differences between different structures are to be computed. This is the definition which was adopted in all subsequent calculations for C.

Results for carbon in different crystal structures are presented in Tables 5.1 and 5.2 and in Fig. 5.4. We chose systems with different bonding and electronic properties: a sp^3 bonded insulator, diamond, a sp^2 bonded semi-metal, planar graphite, and a sp bonded metal, a non dimerized C chain. Table 5.1 shows the binding energy of the three structures as a function of the size of the LR. The calculations were performed with $E[Q(\mathcal{N} = 1)]$. The errors for $N_h = 2$ and $N_h = 3$ are of the same order of those found in the case of silicon, and in particular we found that already for $N_h = 2$ the LO formulation and a direct diagonalization scheme are in good accord. In Fig. 5.4 we compare the total energy of the three C systems as a function of the lattice parameter, as obtained by direct diagonalization of the Hamiltonian and by minimizing $E[Q(\mathcal{N} = 1)]$ with respect to LO, with $N_h = 2$. The agreement between the two calculations is again very good for the three systems, in spite of their different bonding and electronic properties. The percentage difference between the computed equilibrium properties (lattice

Crystal structure	r_0	$\mathbf{E}_c \; [N_h = 2]$	$\mathbf{E}_c \; [N_h = 3]$	$\mathbf{E}_c \; [N_h = \infty]$
Diamond	1.54	7.16	7.23	7.26
2D-graphite	1.42	7.09	7.19	7.28
1D-chain	1.25	5.62	5.75	5.93

Table 5.1: Cohesive energy E_c (eV) of different forms of solid carbon computed at a given lattice constant r_0 (Å) as a function of the number of shells (N_h) included in the LR. The calculations were performed with a TB Hamiltonian, with supercells containing 216, 128 and 100 atoms for diamond, two-dimensional graphite and the linear chain, respectively.

Crystal structure	δr_0 (%)	δE_c (%)	δB (%)
Diamond	0.2	1.4	1.0
2D-graphite	0.4	2.5	1.4
1D-chain	0.5	4.7	2.7

Table 5.2: Percentage errors on the equilibrium lattice parameters (δr_0), cohesive energy (δE_c) and bulk modulus (δB) of diamond, graphite and a carbon linear chain, as obtained by minimizing E[Q] with Q[$\mathcal{N} = 1$] and $N_h = 2$, described within a TB framework. The errors were evaluated with respect to a computation with extended orbitals.
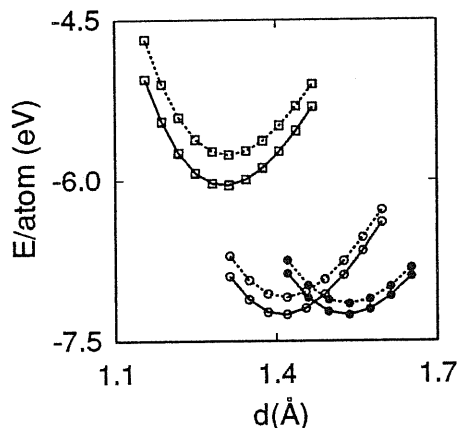
67

Figure 5.4: TB total energy (E) of diamond (dots), bidimensional graphite (open circles) and a carbon linear chain (squares) as a function of interatomic distance (d), computed with supercells containing 216, 128 and 100 atoms, respectively. The dotted lines were obtained by minimizing $E[\mathbf{Q}]$ with $\mathbf{Q}[\mathcal{N} = 1]$, and by using localization regions with $N_h = 2$. The solid lines were instead obtained by diagonalizing the Hamiltonian.

constant, cohesive energy and bulk modulus) are given in Table 5.2.

5.5 Molecular Dynamics with TB Hamiltonians

By using the functional $E[\mathbf{Q}]$ and localized orbitals one can set up a MD scheme in which the computational cost of each step scales linearly with the system size. According to the Helmann-Feynman theorem, see Sec. 3.2, one can obtain the forces acting on a given atom I by computing $\mathbf{F}_I = -\frac{\partial}{\partial \mathbf{R}_I} E[\mathbf{Q}; \{\phi_L\}, \{\mathbf{R}_I\}]$; here $(\mathbf{R}_I)$ denotes ionic positions and $\{\phi_L\}$ are the localized orbitals which minimize $E[\mathbf{Q}]$. The general expression of the ionic forces is given by $\mathbf{F}_I = -2\sum_{i,j}^{N/2} Q_{ij} < \phi_i|\frac{\partial V}{\partial \mathbf{R}_I}|\phi_j >$, where V indicates the external potential in a LDA calculation and the Hamiltonian in a TB calculation. In practical computations it is convenient to first calculate the

auxiliary wave-function

$$|\overline{\phi_i}> = \sum_j^{N/2} Q_{ij}|\phi_j>$$

(5.17)

and then to evaluate the expression of $\mathbf{F}_I$ as follows:

$$\mathbf{F}_I = -2\sum_i^{N/2} < \phi_i|\frac{\partial V}{\partial \mathbf{R}_I}|\overline{\phi_i}> .$$

(5.18)

The ground state wave-functions $\{\phi_L\}$ can be obtained either by evolving the electronic states according to a Car-Parrinello [4] dynamics (see, e.g. Ref. [39]), or by minimizing the energy functional $E[\mathbf{Q}]$ at each ionic move. In our simulations, we determined the sets LR_I at each ionic step; consequently the sites belonging to a set vary as a function of time, when, e.g. the atoms are diffusing or changing their local coordination. This implies an abrupt modification of the basis functions used for the expansion of $\{\phi_L\}$ and therefore a discontinuity of $\{\phi_L\}$ as a function of the ionic positions. In correspondence to any change of the sets LR_I, $E[\mathbf{Q}]$ must be minimized with respect to the electronic degrees of freedom; we therefore chose to minimize the energy functional at each ionic step, unrespective of whether the LR changes at a given step. The minimizations were performed with a conjugate gradient procedure where we used as initial guess for the orbitals the linear extrapolation of the minimized wave-functions of the two previous ionic steps, as suggested in Ref. [36].

In order to test the accuracy and efficiency of the LO scheme for different classes of systems, we performed MD simulations for a crystalline insulator, i.e. diamond at low temperature, and for a liquid metal, i.e. liquid carbon at $T \simeq 5000K$. As for the calculations for C presented in the previous Section, we adopted LRs centered on atoms, which include up to second shell of neighbors and whose shape is determined by the hopping parameters.

We first discuss the case of crystalline diamond, when the sets LR_I do not vary in time. We found that for diamond our MD scheme allows for a correct description of the total energy oscillations, around equilibrium, consistently with what obtained [39] for Si. We performed two simulations, one with a 64 atom and the other with a 1000 atom supercell. In both cases we started from a ionic configuration with zero velocities, generated by giving a random displacement to the atoms up to .03 Å with respect to their equilibrium
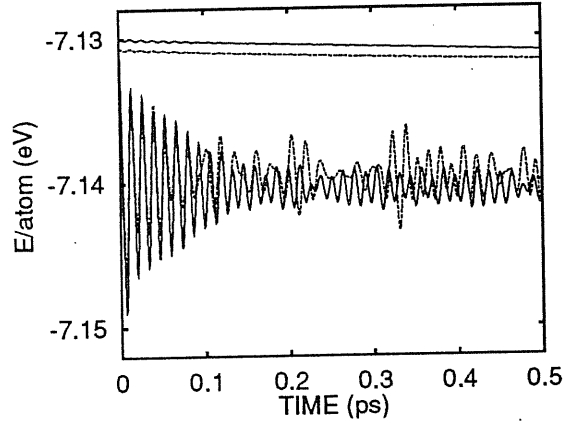
69

Figure 5.5: Potential energy (lower part) and the sum of the potential and kinetic energy (upper part) as a function of simulation time for crystalline C in the diamond structure at 70 K. The dotted and solid lines refer to two calculations with 64 atom and 1000 atom supercells respectively. In both cases we used $Q[\mathcal{N} = 1]$ and $N_h = 2$; the LRs were computed for the configuration at 0 K and held fixed during the simulation.

positions. The integration time step (Δt) used in the simulations was 30 a.u. and the number of CG iterations per ionic move was 10. In Fig. 5.5 we show the potential energy (E) and the sum of the kinetic (E_{kin}) and potential energy of the system as a function of the simulation time. It is seen that the same energy drift $\Delta(E + E_{kin})/E_{kin}$ (0.1 in 0.5 ps) was found for the two simulations. This shows that the number of CG iterations to obtain a given accuracy in the energy conservation does not depend on the size of the system and that the overall scaling of the computational scheme is therefore linear. Finally we evaluated the relative error on the ionic forces $\mathbf{F}_I$ introduced by localization constraints as $\frac{\Delta F}{F} = \frac{\overline{\sum_I |\mathbf{F}_I^{loc} - \mathbf{F}_I^{ext}|}}{\overline{\sum_I |\mathbf{F}_I^{ext}|}}$, where the overline indicates time averages, and the upperscripts *loc* and *ext* refer to calculations performed with localized and extended states, respectively. This error was found to be $\simeq 6\%$ in crystalline diamond at room temperature.

We note that if extended states are used, the number of iterations needed to have the same conservation of energy as the one reported in Fig. 5.5 is smaller than 10. Nevertheless our MD scheme applied to ordered systems becomes more efficient than direct diagonalization of the Hamiltonian already
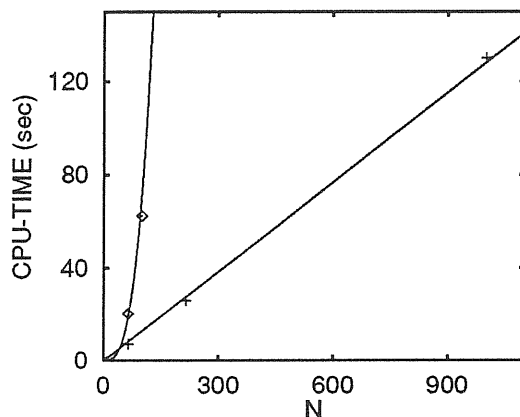
70

Figure 5.6: CPU time per ionic step (30 a.u.) as a function of the number N of atoms in the system, for a TB-MD simulation of C diamond at low temperature (see text). Squares and crosses indicate the CPU time in a direct diagonalization based scheme and in our MD approach (with 10 CG iterations per ionic move), respectively. Calculations were carried out on a Silicon Graphics Iris Indigo 4000.

for small systems, i.e. for systems containing more than 40 atoms. This can be seen in Fig. 5.6 where we compare the efficiency of our approach to that of direct diagonalization based MD schemes.

We now analyze a MD simulation run during which the sets LR_I change as a function of time. In Fig. 5.7 we show the potential energy for an oscillation of crystalline diamond around equilibrium, computed with extended (E^{ext}, dotted line) and with localized (E^{loc}, solid line) orbitals as a function of simulation time (t). The two energies have been computed for the same ionic trajectories, generated by a simulation with localized orbitals. The MD run shown in Fig. 5.7 is the same as the one reported in Fig. 5.5 but now the LRs are allowed to vary in time. At $t = \mathbf{t1}$, the evolution of the ionic positions makes the number of atoms belonging to given localization regions to increase. At $t = \mathbf{t2}$, the ionic configuration is such to restore the localization regions as they were at $t \leq \mathbf{t1}$. Since at $t = \mathbf{t1}, \mathbf{t2}$ an abrupt modification of the basis functions used for the expansion of $\{\phi_L\}$ occurs, the potential energy E^{loc} is discontinuous and its derivative with respect to ionic positions is not well defined. However ionic forces can still be defined by neglecting the
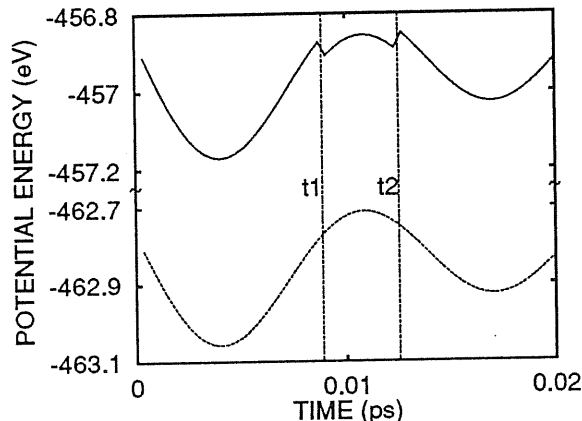
Figure 5.7: Potential energy for an oscillation of crystalline diamond around equilibrium, computed with extended (dotted line) and with localized (solid line) orbitals as a function of simulation time. The two energy curves have been computed for the same ionic trajectories, generated by a simulation with localized orbitals. The LO calculation is the same as the one carried out in Fig. 5.5, but here the LRs are allowed to vary during the simulation.

discontinuity in E and by evaluating either the left or the right derivatives of the potential energy. The numerical values of the left and right derivatives are in fact the same within a very small error. This error is negligible, being much smaller than the one introduced by localization constraints. This can be seen in Fig. 5.8 where we compare forces obtained in calculation with extended and localized orbitals by plotting $dE^{ext}/dt = \sum_I \mathbf{F}_I^{ext} \cdot \mathbf{v}_I$ (dotted line) and $dE^{loc}/dt = \sum_I \mathbf{F}_I^{loc} \cdot \mathbf{v}_I$ (solid line). On the scale of the picture no discontinuity is observable in dE^{loc}/dt at $t = t1, t2$.

We now turn to the discussion of the simulation of liquid C, during which many changes of LR_I were observed. We generated a diffusive state at $T \simeq 5000$ K starting from a diamond network prepared at a macroscopic density of 2 grcm^{-3}; we then heated the system by means of a Nose'-Hoover thermostat. We used a 64 atom cell with simple cubic periodic boundary conditions and only the Γ point to sample the BZ. We used a cutoff radius of 2.45 Å for the hopping parameters entering the TB Hamiltonian and for the two body repulsive potential [53] (i.e. the cutoff distances r_m and d_m of Ref. [53] are set at 2.45 Å). Equilibration of the system was performed in the canonical

72

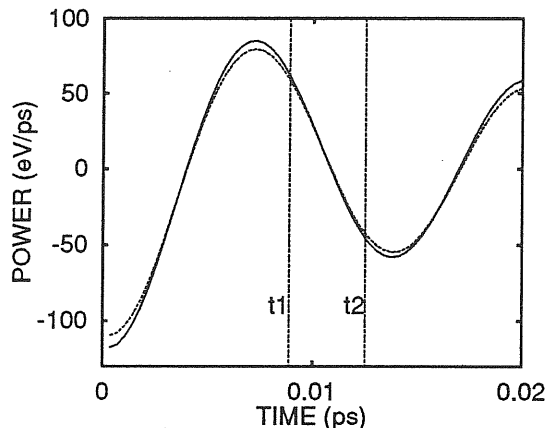Figure 5.8: Time derivatives $dE^{ext}/dt = \sum_I \mathbf{F}_I^{ext} \cdot \mathbf{v}_I$ (dotted line) and dE^{loc}/dt $= \sum_I \mathbf{F}_I^{loc} \cdot \mathbf{v}_I$ (solid line) of the potential energy curves reported in Fig. 5.7 (see text).

ensemble and temporal averages were taken over 3.8 ps. The same simulation was repeated twice: once with our MD scheme and once by using direct diagonalization at each step. The radial distribution function $g(r)$ and the partial atomic coordinations obtained in the two cases are shown in Fig. 5.9 and Table 5.3, respectively. The agreement between the two descriptions is excellent, showing that the LO scheme is accurate even for a difficult case such as a disordered system with differently coordinated atoms and metallic properties. The self-diffusion coefficients obtained in the two cases are 0.4 10^{-4} cm^{2}sec^{-1} and 0.6 10^{-4} cm^{2}sec^{-1}, respectively. The difference between the cohesive energies computed within the extended orbitals and the LO formulation for given ionic configurations is of the order of 2%, similarly to what found for crystalline structures.

In the simulation for the liquid with LO, we used $\Delta t = 5$ a.u. and we performed 50 iterations per ionic move, in order to minimize $E[\mathbf{Q}]$. This number is much larger than that needed for ordered systems, such as crystalline diamond. Consequently in the case of liquid C our scheme becomes advantageous with respect to direct diagonalization when the number of atoms is larger than 200.

N_c	$N_h = 2$	$N_h = \infty$
1-fold	5	4
2-fold	38	42
3-fold	53	50
4-fold	4	4

Table 5.3: Percentage number of differently coordinated sites (N_c) in liquid C computed as averages over a TB-MD simulation of 3.8 ps. The results of the LO formulation with $N_h = 2$ and $\mathcal{N} = 1$ are compared to those of a direct diagonalization scheme ($N_h = \infty$).
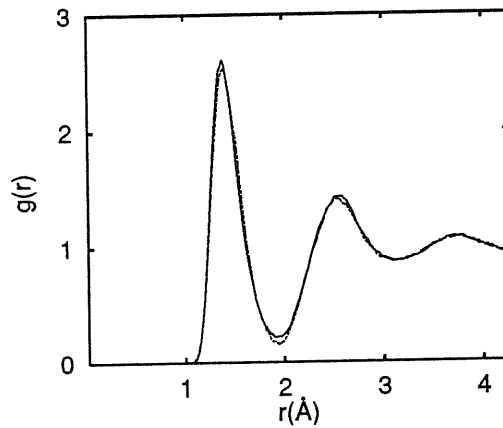

Figure 5.9: Radial distribution function g(r) of liquid C (see text) computed as average over a TB-MD simulation of 3.8 ps. The results of the LO formulation with $N_h = 2$ and $\mathcal{N} = 1$ (dotted line) are compared to those of a direct diagonalization scheme (solid line). The average number of atoms in a LR is 18.

5.6   Conclusions

We have presented an approach to total energy minimizations and molecular dynamics simulations whose computational workload is linear as a function of the system size. This favorable scaling is obtained by using an energy functional whose minimization does not imply either explicit orthogonalization of the electronic orbitals or inversion of an overlap matrix, together with a localized orbital formulation. The use of LOs reduces the evaluation of the energy functional and of its functional derivative to the calculation of products of sparse matrices.

The performances and efficiency of the method have been illustrated with several numerical examples for semiconducting and metallic systems. In particular we have presented molecular dynamics simulations for liquid carbon at 5000 K, showing that even for the case of a disordered metallic system the description provided by the LO formulation is reliable and very accurate. We have also shown that tight binding molecular dynamics simulations with 1000 atoms are easily feasible on small workstations, implying a one day run to obtain 0.5 ps.

Chapter 6

C_{60} impacts on a semiconducting surface

Since the discovery [54] of the unique stability of C_{60} molecules against surface induced fragmentation, the investigation of fullerene interactions with solid substrates has become an exciting field of research [54]-[63]. Collisions of C_{60} on several surfaces have been reported to induce no fragmentation of the impinging molecules, for initial kinetic energies (E_k) up to a few hundred eV [54]. This property is unprecedented in molecular-ion surface-induced phenomena and has earned C_{60} the name of *resilient* molecule.

Of particular interest is the case of C_{60} impacts on semiconducting surfaces which can form covalent bonds with the cluster. The study of these bonds is a challenging problem, from a fundamental point of view. Furthermore such an investigation is an essential prerequisite for the understanding of fullerene deposition on non-metallic substrates. These deposition processes have recently been proposed [63] as a valuable way of synthesizing thin films which would retain specific characteristics of the incident clusters.

In order to understand the physics of C_{60} collisions on solid substrates, it is crucial to reveal the processes occurring *at* the surface. Whereas these processes are difficult to probe experimentally [54], they can be investigated by computer simulations. Recently, simulations of C_{60} impacts on a hydrogenated diamond surface have been performed by using both classical potentials [56] and tight binding (TB) Hamiltonians [61]. The comparison between the results of the two studies and experiments [61, 62] indicates that a quantum mechanical (QM) treatment is necessary in order to have an

accurate description of the cluster-surface interactions.

Realistic simulations of C_{60} interactions with a surface require cells with number of atoms of the order of a thousand. Until recently QM computations for systems of this size have not been possible because of the computer time required by conventional algorithms, which grows as the cube of the number of atoms in the system (N). Indeed the only QM study reported to date [61] has been limited to small MD cells.

This situation has changed with the introduction of methods for electronic structure calculations and MD simulations, which are based on algorithms whose computational workload grows linearly with the system size. These methods are usually referred to as $O(N)$ methods. These approaches have opened the way to QM-MD simulations of systems much bigger than previously accessible, and therefore to the study of problems usually out of reach for QM calculations.

In this Chapter we present QM-MD simulations of C_{60} impacts on a semiconducting surface as a function of the molecule incident energy, carried out with the $O(N)$ method described in Chapter 5, and with MD cells containing 1140 atoms. Interatomic forces are described according to a tight binding (TB) Hamiltonian [53], derived from first principles calculations. We considered the clean (2×1) reconstructed diamond (111) surface. This surface can be expected to form bonds with the impinging C_{60}, since its uppermost layer contains three fold coordinated π bonded atoms. It therefore represents a good candidate for the study of covalent bonds between the fullerene and a semiconducting substrate. The results of our calculations are in very good agreement with experiments carried out under the same impact conditions [54, 55, 57, 58, 59]. Furthermore they allow us to characterize in detail the microscopic processes occurring during the collision and thus to identify three different impact regimes as a function of C_{60} incident energy. Finally, we found a relation between the cluster reactivity to the surface and the presence of defects in the cluster. This observation gives us insight into the deposition mechanisms of C_{60} on semiconducting substrates.

The results presented in this Chapter are also reported in Ref. [43].

The Chapter is organized as follows. In Sec. 6.1 the details of the simulations are reported. In Sec. 6.2 we discuss the results of our simulations, and Sec. 6.3 is devoted to the conclusions.

6.1 $O(N)$ quantum molecular dynamics: description of the simulations

In our calculations, we used the $O(N)$ method described in Chapter 5. This approach is based on an energy functional with implicit orthogonalization constraints and on a localized orbital formulation. We adopted the TB Hamiltonian proposed by Xu et al. [53]. We used a cutoff radius of 2.30 Å for the hopping parameters of TB Hamiltonian and for the two body repulsive potential. As suggested in Ref. [53], in order to control the charge transfer in the presence of dangling bonds, we have considered in the total energy a Hubbard-like term equal to $(1/2)U(q_I - 4)^2$, where q_i is the total charge at the atomic site I and U=8eV. Indeed in simulations performed with U=0 we observed unphysical charge transfers, as large as one electron on some sites.

The localized orbitals were centered on atomic sites, extending up to second neighbors (in the notation of Chapter 5, $N_h = 2$). At each MD ionic step the electronic energy was minimized with a conjugate gradient procedure, by performing 15 iterations per ionic move and by extrapolating linearly the input wave-function from the two previous ionic steps. The time steps used for the integration of the equations of motion varied from 15 to 6 a.u. according to the incident kinetic energy E_k.

We simulated neutral C_{60} molecules colliding with a Pandey reconstructed C(111) surface at initial energies E_k= 60, 80, 120, 150, 180, 210, 240, 300, 400 eV. Each of the nine runs lasted from 0.3 to 1 ps. The efficiency of the $O(N)$ algorithm allowed us to carry out all the calculations on workstations. C_{60} impinged upon the surface at normal incidence, oriented in such a way that a double bond between two hexagons faced a Pandey chain of the surface. The C(111) substrate was represented by a slab composed of twelve layers, each containing ninety C atoms. The dimensions of a layer were 22.72× 21.86 Å in the x and y direction, respectively. The slab was terminated on each side by a reconstructed surface, and periodic boundary conditions were applied along x and y. Nine surface layers were allowed to move during the simulations. According to the size of our MD cell and to the number of mobile layers, we estimate that the shock wave produced by a collision of C_{60} with the substrate is echoed back to the impact region about 0.2 ps after the impact. This is the time interval during which we observe the formation

of bonds between the cluster and the surface. Therefore the characterization of the three impact energy regimes proposed in the following is not affected by finite size effects.

Before starting the simulation of C_{60} collisions on the surface, we optimized the slab and the molecule geometries independently. Our results for the surface reconstruction compare well both with those of a conventional calculation using the same TB Hamiltonian [64] and extended orbital, and with the findings of first principles computations [65]. For example, we find that the average bond distance in the surface chains is 1.44 Å and that the change in bond length between the second and third layer is 6%; the corresponding values reported in Ref. [64] are 1.48 Å and 6%, whereas those of Ref. [65] are 1.44 Å and 8%. However our calculation seems to overestimate the dimerization of the surface chains (4% versus 0.2% in Ref. [64] and 1.4% in Ref. [65]). The two characteristic bond lengths of C_{60} calculated within the localized orbital formulation differed by 5% (single bond) and 2.5% (double bond) from those optimized with extended orbital. Also in this case the TB results [66] are in good agreement with those of first principles calculations [67]. We note that the differences between the localized orbital and the extended orbital formulations can be systematically reduced by using localized orbitals which extend up to third neighbors ($N_h=3$). For example in the case of C_{60} with $N_h=3$ the errors are 1.1% (single bond) and 0.7% (double bond). We believe that calculations with $N_h=2$ are sufficiently accurate for the purpose of the present investigation.

6.2 Results of the simulations

The results of the simulations allow the identification of three impact regimes, as a function of the fullerene incident kinetic energy E_k: a low energy regime for $E_k \leq 120$eV, a medium energy regime for 150eV$\leq E_k \leq$210eV and a high energy regime for $E_{kin} \geq 240$eV.

As shown in the next subsections, the energy regimes can be defined according to the modification in the C_{60} ionic structure and to the bonding properties between the cluster and the surface. In particular in the low energy regime, the molecule bounces off the surface without ever forming bonds, and recovers its original shape after severe distortions. In the medium energy regime, C_{60} forms covalent bonds with the surface. The cluster can be either

adsorbed on or leave the substrate, preserving its original cage structure with few coordination defects. In the high energy regime the molecule cage structure opens and pieces of the broken cage form stable bonds with the substrate.

6.2.1 Bond formation between the cluster and the surface

We now analyze the occurrence of covalent bonding between the cluster and the surface during the MD simulation. Throughout the Chapter we use a cutoff distance of 1.9 Å to define bonds and atomic coordination.

In the low energy regime, i.e. in the simulations with E_k=60, 80 and 120 eV, the molecule does not form any bond with the surface. The minimum distance between C_{60} atoms and the substrate (**D**) is approximately constant during the collision and very close to 2 Å, as seen in Fig. 6.1, where we show **D** as a function of the simulation time (**t**). In all the three cases after the impact the molecule leaves the surface.

In the medium energy regime, i.e. in the simulations with E_k=150, 180 and 210 eV, the C_{60} bonds to the surface. Indeed, after some oscillations around 2 Å, **D** suddenly decreases to a value of about 1.5 Å, i.e. to a distance typical of sp^3 like bonds, as it is seen from Fig. 6.1. Not surprisingly the surface atoms involved in the bonding belong to the topmost layer, containing three-fold coordinated sites in the Pandey reconstruction. In Fig. 6.2 we show the number of bonds (**Nb**) between C_{60} and the surface as a function of the simulation time. In this energy regime **Nb** depends weakly on E_k. For E_k=150 eV, these bonds are stable after the impact and the cluster is adsorbed on the surface. This is also seen in Fig. 6.3 where a snapshots of the simulation 1.00 ps after the impact is shown. For E_k=180 and 210 eV, the C_{60}-surface bonds break after the collision and the molecule leaves the substrate as shown in Fig.s 6.1 and 6.2. We recall that in collision experiments on a graphite substrate [55, 59] a decrease in scattering intensities around 140 eV has been found , which has been ascribed to the adsorption of intact C_{60} [55].

Finally in the high energy regime, i.e. in the simulations with E_k=240, 300 and 400 eV, we observe the formation of several bonds between C_{60} and the surface is observed. Their average number increases with the incident
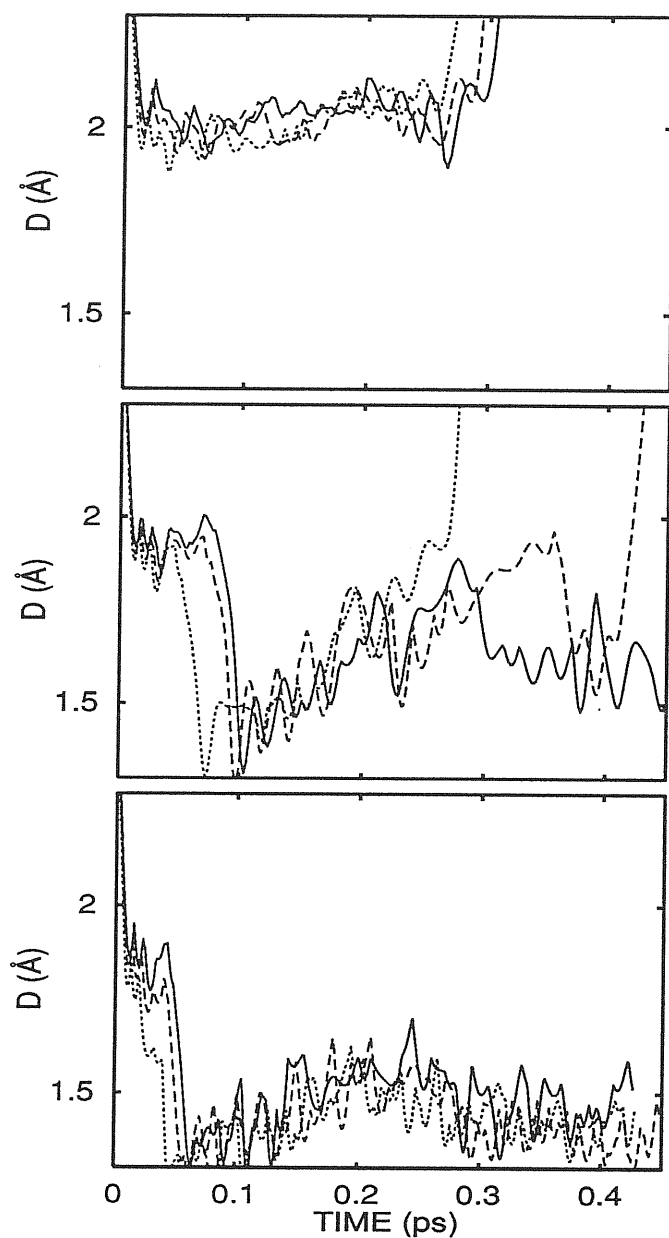
80

Figure 6.1: Minimum distance (**D**) between C_{60} and the surface as a function of the simulation time in the low (upper panel), medium (middle panel) and high (lower panel) energy range. Solid, dashed and dotted lines correspond to E_k= 60, 80 and 120 eV (upper panel), to E_k= 150, 180 and 210 eV (middle panel), and to E_k= 240, 300 and 400 eV (lower panel).
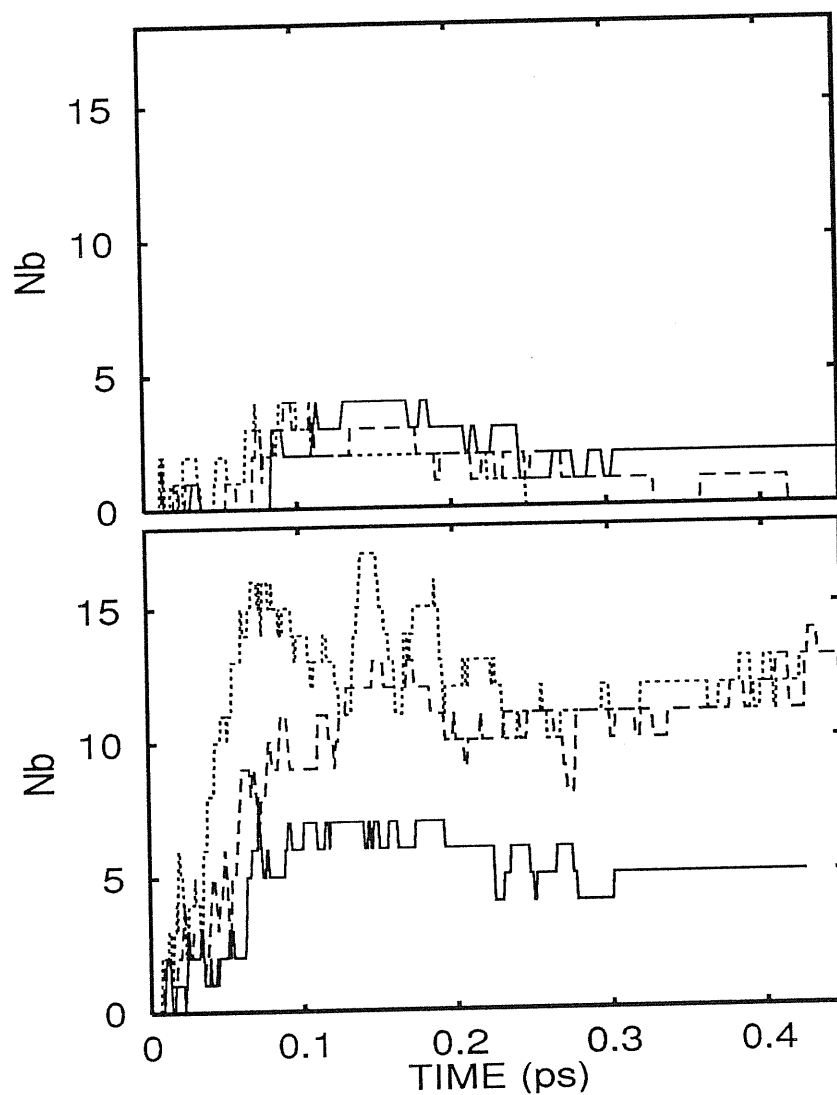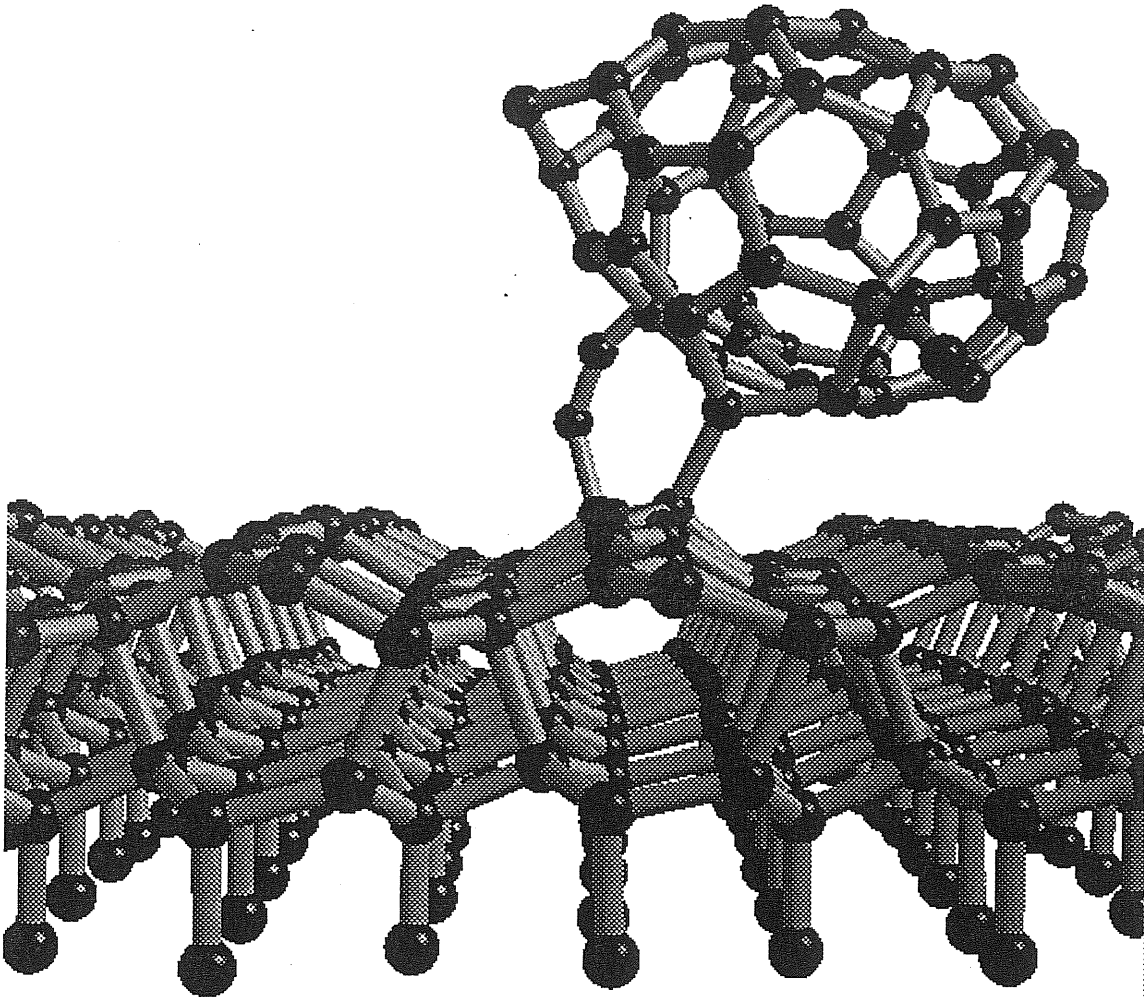
Figure 6.2: Number of bonds (**Nb**) between C_{60} and the surface as a function of the simulation time in the medium (upper panel), and high (lower panel) energy range. Solid, dashed and dotted lines correspond to $E_k = 150$, 180 and 210 eV (upper panel), and to $E_k = 240$, 300 and 400 eV (lower panel).

Figure 6.3: Snapshot of the uppermost five layers of the slab and of C_{60} for $E_k=150$ and at $t=1.00$ ps.

83

energy, as it is shown in Fig. 6.2. In this regime the surface atoms involved in the bonding belong also to the second surface layer, containing four-fold coordinated sites.

6.2.2 Modification in the cluster structure

We now turn to the discussion of the modification in the fullerene structure induced by the collision.

In the low energy regime the impact provokes large distortions in the fullerene cage: the cluster height is decreased from 7.0 to 3.9, 3.4 and 3.1Å , for E_k= 60, 80 and 120 eV, respectively, and the flattened molecule adapts its shape to that of the reconstructed surface. This is also seen in the snapshot of the simulation with E_k=120 eV reported in Fig. 6.4. For E_k=120 eV, a few bonds of the molecule are broken during the collision, whereas no bond breaking is observed at lower energies. This can be seen in Fig. 6.5 which displays the number of 2-fold and 3-fold coordinated sites of C_{60} as a function of t. In this energy regime, after the impact the cluster leaves the surface with its original shape, without any defect.

In the medium energy regime the molecule does not only suffer large distortions upon impact on the surface, but also some bonds of the C_{60} cage are broken during the collision, resulting in the formation of twofold coordinated sites, as it is seen in Fig. 6.5. After the collision, the topology of the molecule is still that of a cage, although defects are present with respect to the original shape (see Fig.s 6.3 and 6.5).

In the high energy regime many bonds break within the molecule (see Fig. 6.5) and the cage structure of the fullerene can no longer be identified. A disordered structure is formed and adsorbed on the substrate as it is seen in Fig. 6.6, where we show a snapshot of the simulation with E_k=300 eV for t=.33ps. After the 300 and 400 eV collisions, some of the C_{60} atoms form twofold coordinated chain structures. Note that the formation of such chains was observed also in MD studies of fullerene melting [68].

In the medium and high energy regime we observed the formation of cluster-surface bonds also after some oscillations of the molecule on the surface, i.e. when the speeds the C_{60} atoms was decreased by orders of magnitude with respect to the initial incident speeds. Instead in the low energy regime the cluster is totally inert to the surface. Thus the formation of cluster-surface bonds is not related to the speed of the cluster atom which
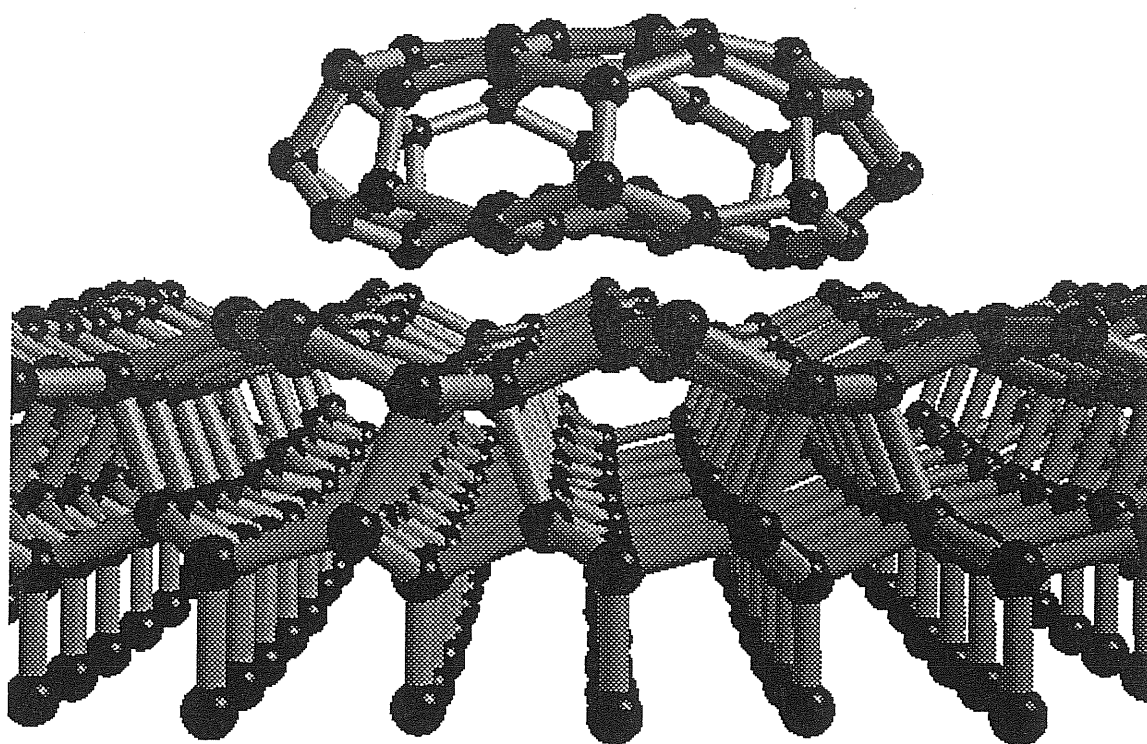
84

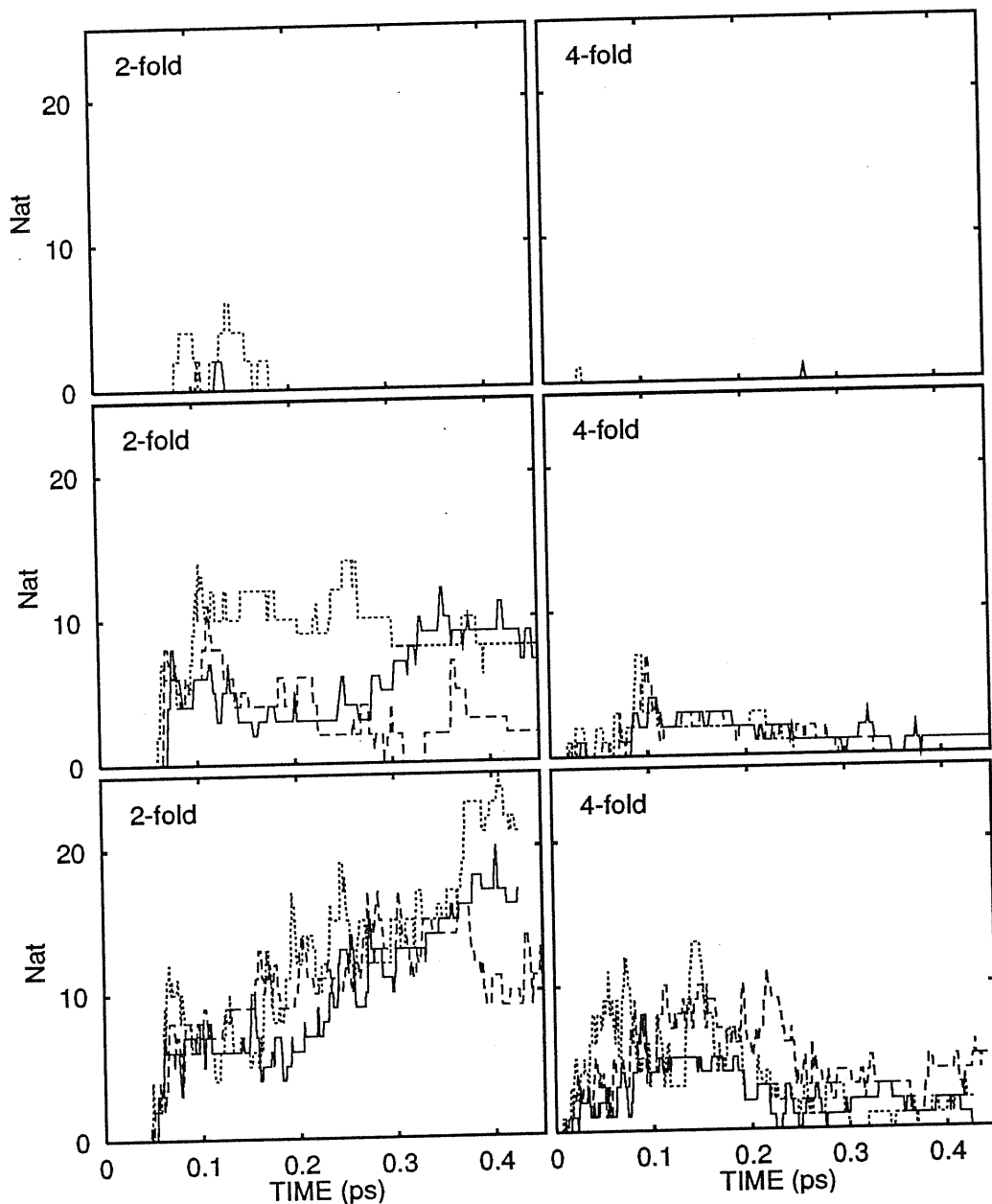Figure 6.4: Snapshot of the uppermost five layers of the slab and of C_{60} for $E_k=120$ and at $t=0.14$ ps.

Figure 6.5: Twofold and fourfold coordinated C_{60} atoms (N_{at}) as a function of the simulation time in the low (upper panel), medium (middle panel) and high (lower panel) energy range. Solid, dashed and dotted lines correspond to E_k= 60, 80 and 120 eV (upper panel), to E_k= 150, 180 and 210 eV (middle panel), and to E_k= 240, 300 and 400 eV (lower panel).
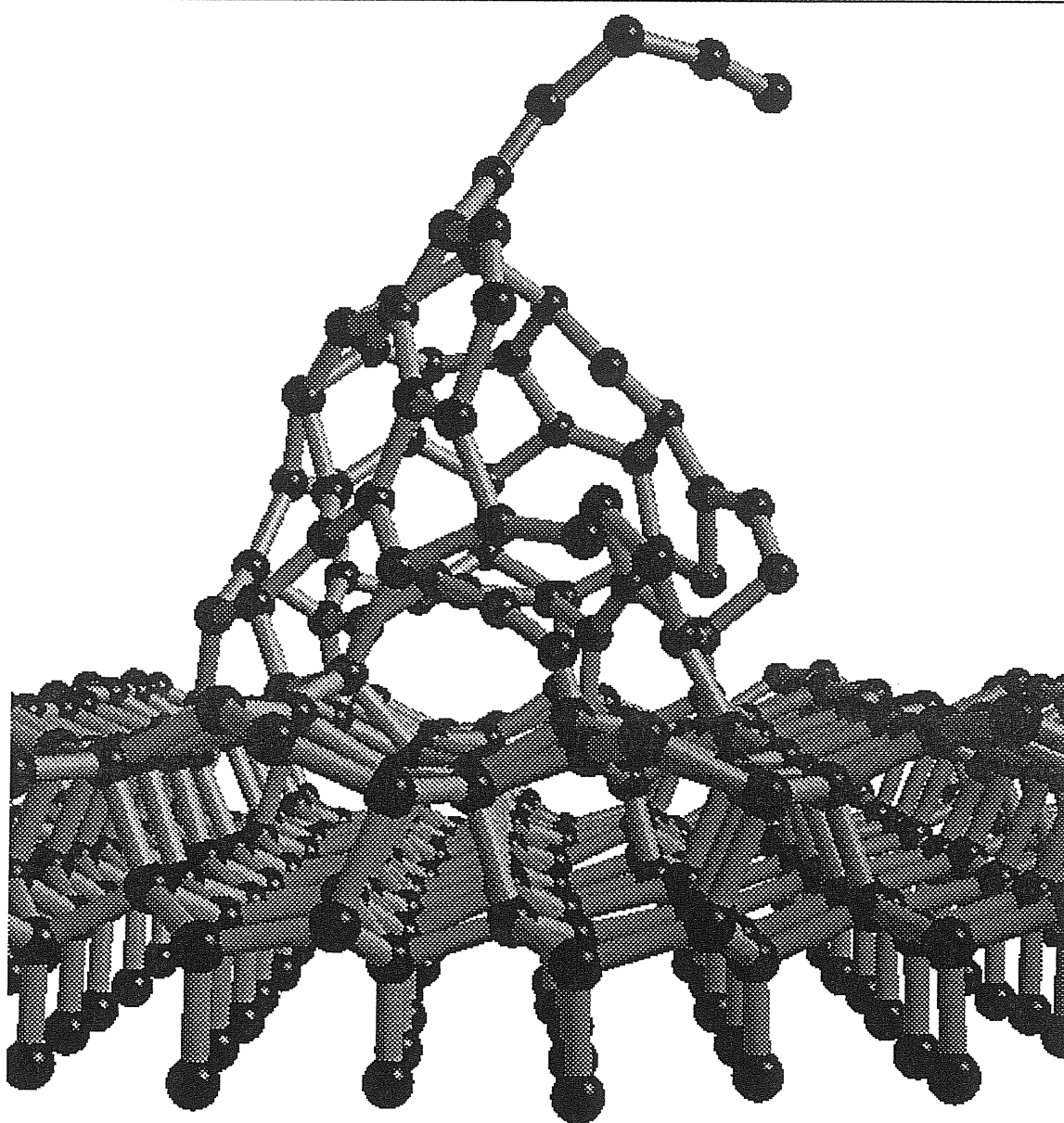
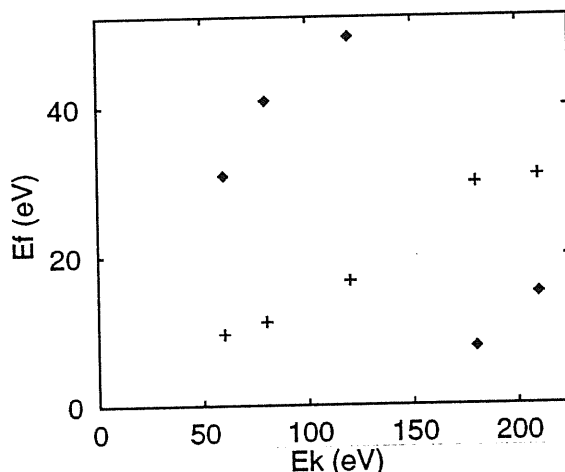Figure 6.6: Snapshot of the uppermost five layers of the slab and of C_{60} for E_k=300 and at t=0.33 ps.

Figure 6.7: Final energies (E_f) of C_{60} bouncing on the surface as a function of E_k: diamonds and crosses indicate the kinetic energy of the centre of mass (E_{cm}) and the internal kinetic energy of the molecule (E_{in}), respectively.

forms the bond but to the reactivity of the C_{60} molecule. From our simulations there is a close relationship between the C_{60} reactivity with the surface and the presence of defects in the molecule. We expect that this fact might characterize deposition processes of the fullerene on other semiconducting surfaces. Therefore the variety of STM images produced by covalently bonded C_{60} on, e.g., Si(111) [60], might correspond to molecules with different types of defects.

6.2.3 Outgoing clusters

In this subsection we analyse the ionic kinetic state of the cluster after the collision when the cluster bounces off the surface.

In Fig. 6.7 we show the translational kinetic energy E_{cm}, i.e. the kinetic energy of the centre of mass, and the internal kinetic energy E_{in}, i.e. the kinetic energy with respect to the center of mass, of the outgoing molecule as a function of the incident energy E_k.

In the low energy range, E_{cm} shows a clear dependence upon E_k. In particular E_{cm} is proportional to E_k for incident energies in the two collisions $E_k=60$ and 80 eV. Note that in these simulations no bonds of the cluster are broken.
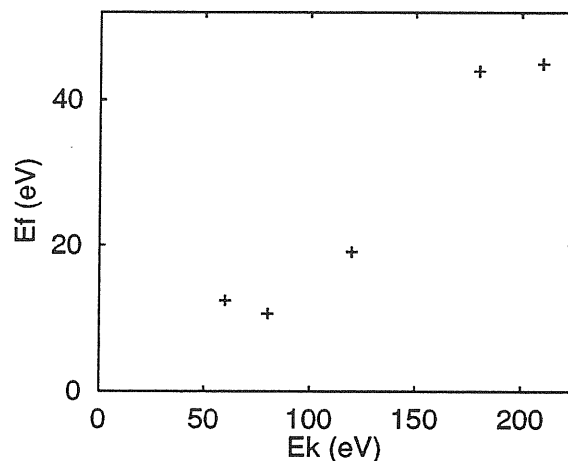
Figure 6.8: Final kinetic energies (E_f) of the slab after the collision.

In the medium energy range when the molecule leaves the substrate, i.e. for E_k=180 and 210 eV, E_{cm} is equal to 8 and 15 eV, respectively. Our findings compare well with those of Ref. [55], where the E_{cm} of fullerene ions scattered from graphite is found to be distributed between 10 and 20 eV and nearly independent of the impact energy, for E_k larger than 140 eV.

Whenever C_{60} left the surface, we did not observe any fragmentation of the molecule. However a rupture may be expected to occur some time after a collision if the internal energy E_{in} of the bouncing molecule (see Fig. 6.7) exceeds its stability threshold. MD investigations of fullerene melting [68] have shown that C_{60} becomes unstable when its internal kinetic energy (E_{in}) is between 30 and 40 eV.

6.2.4   Behavior of the surface

We conclude the analysis of the MD simulations with the description of the surface behavior.

In the low and medium range the topology of the reconstructed surface is unaffected by the collision, although a considerable fraction of E_{in} is transferred from the molecule to the slab, as it is seen in Fig. 6.8, where we show the kinetic energy of the slab after the collisions in which the cluster leaves the surface. In the medium energy range only the three fold coordinated atoms of the topmost layer bond to C_{60} atoms (see Fig. 6.3).

In the high energy range the fourfold coordinated surface atoms (belonging to the second layer) are also involved in bonding to the molecule. However they remain fourfold coordinated since their bonds with the third layer atoms are broken. This bond breaking induces a local surface deconstruction from a π bonded chain geometry towards a (1×1) ideal arrangement (see Fig. 6.6).

6.3 Conclusion

In summary, we have identified three impact energy regimes of C_{60} collisions on C(111). For $E_{in} \leq 120$ eV, the molecule bounces off the surface without ever forming bonds, and recovers its original shape after severe distortions. In a second regime, C_{60} forms covalent bonds with the surface. The cluster can be either adsorbed on or leave the substrate, with defects in its original structure. The energy at which we observe absorption (150 eV) corresponds to the energy at which a decrease of fullerene ions scattered from graphite is observed experimentally. In the third regime ($E_k \geq 240$ eV) the molecule breaks after the impact and pieces of the broken cage form stable bonds with the substrate, which can induce a local surface deconstruction. The formation of bonds between C(111) and the fullerene is always accompanied by the formation of defects in the molecule. When the molecule bounces off the surface, the kinetic energy of its centre of mass shows a clear dependence on its incident energy in the low energy range; on the contrary E_{cm} depends weakly on E_{in} in the medium energy range and acquires values in agreement with those measured under the same impact conditions. Finally we have shown that QM simulations for systems containing thousands of atoms, so far not possible with conventional methods, are now feasible by using $O(N)$ approaches. In the simulations reported in this work, the gain in computer time with respect to conventional $O(N^3)$ methods is estimated to be of the order of 1000.

Appendix

Acceleration schemes for ab-initio molecular dynamics and electronic structure calculations

In this Appendix we reproduce a reprint of Ref. [5].

Acceleration Schemes for Ab-Initio Molecular Dynamics and Electronic Structure Calculations

F. Tassone[a,c] F. Mauri[a,b] and R. Car[a,b]

(a) Institut Romand de Recherche Numerique en Physique des Materiaux (IRRMA)

PHB-Ecublens, CH-1015 Lausanne ,Switzerland

(b) Dept. of Condensed Matter Physics, University of Geneva,

CH-1211 Geneva, Switzerland

(c) Scuola Normale Superiore, P.za dei Cavalieri 7, I-56126 Pisa,Italy

Abstract

We study the convergence and the stability of fictitious dynamical methods for electrons. First, we show that a particular damped second-order dynamics has a much faster rate of convergence to the ground-state than first-order steepest descent algorithms while retaining their numerical cost per time step. Our damped dynamics has efficiency comparable to that of conjugate gradient methods in typical electronic minimization problems. Then, we analyse the factors that limit the size of the integration time step in approaches based on plane-wave expansions. The maximum allowed time step is dictated by the highest frequency components of the fictitious electronic dynamics. These can result either from the large wavevector components of the kinetic energy or from the small wavevector components of the Coulomb potential giving rise to the so called *charge sloshing* problem. We show how to eliminate large wavevector instabilities by adopting a preconditioning scheme that is implemented here for the first-time in the context of Car-Parrinello ab-initio molecular dynamics simulations of the ionic motion. We also show how to solve the charge-sloshing problem when this is present. We substantiate our theoretical analysis with numerical tests on a number of different silicon and carbon systems having both insulating and metallic character.

71.10+x, 71.20Ad

I. INTRODUCTION

The introduction of a fictitious dynamics for the electrons[1,2] with driving forces obtained from the total energy within density functional theory (DFT)[3] has provided a convenient approach to minimize the total energy of condensed matter systems and to perform ab-initio molecular dynamics simulations of the ionic motion. These techniques have been applied successfully to a variety of insulating, semiconducting, and metallic systems involving a large number of atoms in the context of structural optimization problems at zero temperature and of dynamical simulations of the atomic motion at finite temperature[4].

It is a subject of current interest to study the factors that limit the efficiency of fictitious dynamical methods for electrons in order to improve their numerical efficiency. This depends on the choice made for the dynamics and on the size of the time step that can be used to integrate numerically the equations of motion.

When discussing how to choose a specific dynamics, it is convenient to consider total energy minimization separately from molecular dynamics. It has been shown by Car and Parrinello that to simulate the classical adiabatic motion of the atoms it is useful to adopt a second-order Newtonian dynamics also for the electronic degrees of freedom, since this exploits optimally the concept of continuous simultaneous evolution of electronic and atomic degrees of freedom[1,2]. Newtonian dynamics conserves energy. Different approaches should be used to minimize the electronic energy, as it is required to start a molecular dynamics simulation or to solve an optimization problem at zero temperature. The simplest approach to minimization is provided by steepest-descent dynamics, which can be viewed as a dynamics of the first-order in the time-derivative[2]. Steepest-descent dynamics, which requires only knowledge of the gradients of the energy functional, is not very efficient particularly in metallic situations. Better schemes require some knowledge also of the second derivatives of the energy functional either explicitly or implicitly. Conjugate gradient methods have been developed in this context[5-7,10] and have been shown to be superior to steepest-descent methods, particularly when the full energy functional was used in the line minimizations and full account was taken of the orthonormality constraints on the wavefunctions[10].

In this paper we show that a minor modification of a steepest-descent algorithm, namely replacing first-order dynamics with a specific damped second-order dynamics, improves substantially the rate of convergence of the wavefunctions to the ground-state. The resulting scheme, which we call damped molecular dynamics, has efficiency comparable to that of the best conjugate gradient algorithms when used in typical electronic minimization problems, with the additional advantage of having basically the same numerical complexity of simple steepest-descent algorithms.

We then investigate what determines the maximum allowed time step for numerical integration when using steepest-descent (SD), damped (D) or Newtonian molecular dynamics (MD). In all cases the time step is limited by the need to integrate the high frequency components of the fictitious dynamics. These arise either from the large wavevector components of the electronic kinetic energy or from the small wavevector components of the Hartree

energy due to the divergence of the Coulomb potential at small wavevector. In the latter case the related numerical instability is usually referred to as the 'charge sloshing' problem and it is expected to become serious when the size of the system becomes very large.

The large wavevector instability can be eliminated by preconditioning the equations of motion since at large wavevectors the wavefunctions are dominated by the kinetic energy and are to a large extent free-particle like. Indeed, it was already suggested earlier by several authors that this property could be used to speedup iterative schemes for electronic minimization. In particular, Ref. (11) proposed an analytical integration scheme for the large wavevector components of the wavefunctions within second-order dynamics. This scheme was subsequently extended in Ref. (12) to first-order steepest-descent equations. Since this approach can be less stable than standard steepest-descent algorithms[6] we will not discuss it any further. A successful preconditioning scheme in the context of conjugate-gradient minimization of the electronic total energy has been proposed in Ref. (7). This has same similarities with the quasi-Newton step proposed in Ref. (8) and with the residual minimization/direct inversion in the iterative subspace describe in Ref. (9).

In this paper, we propose a preconditioning scheme which is appropriate to all the dynamical methods referred to above, namely SD, D, and MD dynamics. It consists in properly scaling the fictitious masses associated to the large wavevector components of the electronic wavefunctions, in order to compress the high frequency spectrum of the electronic dynamics and to use a larger integration time step. Our preconditioning method is similar in spirit to those of Ref. (7) but it is formulated as a modification of the differential equations leading to SD, D, and MD dynamics. In particular, we apply it here for the first time to the Car-Parrinello MD equations, which provide an efficient approach for ab-initio molecular dynamics simulations of the ionic motion. In this context our preconditioning scheme allows to use a timestep which is two to three times larger than in previous applications of this method, resulting in a considerable saving of computational time.

We now turn our attention to the 'charge sloshing' problem. This has been discussed previously in the context of self-consistent diagonalization of the Kohn-Sham Hamiltonian[13]. The onset of this kind of instability depends on the algorithms used and is expected to occur at significantly large sizes in the context of fictitious dynamical methods since in these approaches the wavefunctions change little over a single timestep. Indeed recent MD simulations for metallic liquid silicon have shown *no sign* of a 'sloshing' instability up to cubic cells containing 216 silicon atoms[14]. However one expects that for sufficiently large cells the 'sloshing' instability should appear, although a quantitative theoretical analysis of it in the context of fictitious dynamical methods for electrons has been so far missing. 'Sloshing' instabilities have been found numerically within some iterative schemes for electronic minimization in the case of systems having a long linear dimension[7]. In this paper we present a theoretical analysis of the 'charge sloshing' problem in the context of SD, D, and MD equations of motion. We find that the 'sloshing' instability is absent for insulators, but it is present for metals. This is in accord with previous results of Ref. (13). A practical scheme to control the sloshing instability is discussed in the paper.

iii

To summarize, we improve the numerical efficiency of fictitious dynamical methods for electrons in several ways. Firstly, we replace steepest descent dynamics by a more efficient damped second order dynamics to minimize the total energy. Secondly, by preconditioning the fictitious electronic masses we increase the integration time step for total energy minimization and for simulation of the adiabatic ionic dynamics. Thirdly, we show that in the context of fictitious dynamical methods the so called 'charge sloshing' problem, which is expected to arise for large systems, is less serious than expected. We support our theoretical analysis with detailed numerical tests on several systems involving Si and C atoms.

The paper is organized as follows. In Sec. II we discuss first-order SD dynamics and second-order conservative MD dynamics for the electronic degrees of freedom. In Sec. III we introduce a damped second-order dynamics which is substantially more efficient than SD and is competitive with the best conjugate gradient schemes for electron minimization. In Sec. IV we discuss large wavevector instabilities and the 'charge sloshing' problem. In Sec. V we discuss the preconditioning of large wavevector components. In Sec. VI we present some details of the numerical implementation. Finally, in Sec. VII we present the results of realistic numerical tests on silicon and carbon systems. Sec. VIII is devoted to our conclusions.

II. FICTITIOUS DYNAMICS FOR THE ELECTRONS

Dynamical methods for minimizing the electronic total energy and for simulating the adiabatic motion of the atoms are based on a fictitious dynamics of the electronic degrees of freedom. Within these approaches the forces acting on the electronic degrees of freedom are derived from the total electronic energy $E[\{\psi\}]$ in the DFT-LDA form:

$$E[\{\psi\}] = E_{kin}[\{\psi\}] + E_{ext}[\rho] + E_h[\rho] + E_{xc}[\rho],\qquad(1)$$

where E_{kin}, E_{ext}, E_h, and E_{xc} denote kinetic, external potential, Hartree and exchange-correlation energy, respectively[3]. The local density approximation is adopted for the latter[3]. The electronic charge density ρ is given by:

$$\rho(\mathbf{r}) = 2 < \psi_i|\mathbf{r} >< \mathbf{r}|\psi_i >,\qquad(2)$$

For reasons of numerical simplicity we adopt here a total energy functional based on a non self-consistent tight-binding Hamiltonian. where the occupied orbitals $|\psi_i>$ are orthonormal. The factor of 2 accounts for the occupation numbers, which here and in the following are supposed to be all equal to 2. Summation over repeated indices is understood.

In order to ensure the orthonormalization of the electronic orbitals during a dynamical evolution it is convenient to add appropriate forces of constraints. These do not perform work on the electronic system, and can be conveniently calculated in terms of Lagrangian multipliers. The corresponding equations of motion for the first order dynamics are:

$$\mu|\dot{\psi}_i> = -\frac{1}{2}\frac{\delta E[\{\psi\}]}{\delta\psi_i} + \Lambda_{ij}|\psi_j>, \tag{3}$$

and those for the second order dynamics are:

$$\mu|\ddot{\psi}_i> = -\frac{1}{2}\frac{\delta E[\{\psi\}]}{\delta\psi_i} + \Lambda_{ij}|\psi_j>. \tag{4}$$

where we have assumed that the wavefunctions $|\psi>$ are real. Here and in the following the indices i and j run over the occupied states only. The symmetric matrix Λ_{ij} of the Lagrange multipliers enforces the orthonormality condition, i.e. $<\psi_i|\psi_j> = \delta_{ij}$. The derivatives of $E[\{\psi\}]$ with respect to the $|\psi_i>$ define the Kohn-Sham Hamiltonian:

$$\frac{1}{2}\frac{\delta E[\{\psi\}]}{\delta\psi_i} = 2\hat{H}_{KS}|\psi_i>. \tag{5}$$

The parameter μ is a fictitious electronic mass. It is used to tune the speed of the electronic dynamics and does not describe any other physical property. When the ions are held fixed, this mass can be included in the definition of the time step and it is irrelevant. However when we allow the ions to move, the ratio between μ and the physical ionic masses is important since it defines the relative speed of the ionic and of the fictitious electronic motion.

Now let us suppose that the wavefunctions are close to the minimum of the energy $E[\{\psi^{(0)}\}]$,

$$|\psi_i> = |\psi_i^{(0)}> +|\delta\psi_i>, \tag{6}$$

where $|\psi_i^{(0)}>$ are the wavefunctions at the minimum and $|\delta\psi_i>$ are the corresponding deviations. We notice that $|\delta\psi_i>$ have to fulfill the orthonormality condition to linear order, i.e. $<\psi_i^{(0)}|\delta\psi_j> = 0$. To linear order in $|\delta\psi_i>$, the Lagrange multipliers Λ_{ij} are the same for first and second order dynamics, and are given by

$$\Lambda_{ij} = 2<\psi_i|H_{KS}|\psi_j>. \tag{7}$$

Thus, by retaining only the terms up to linear order in $|\delta\psi_i>$ in the equations of motion (3) and (4) we obtain:

$$|\delta\dot{\psi}_i> = -\hat{K}_{ij}|\delta\psi_j> \tag{8}$$

and

$$|\delta\ddot{\psi}_i> = -\hat{K}_{ij}|\delta\psi_j>, \tag{9}$$

respectively. Here $\hat{K}_{ij}$ is a linear operator, which acts on the single-particle Hilbert space and which has the *same* form for *both* first- and second-order dynamics. In the following we will use the notation $\hat{\mathbf{K}}$ to indicate a matrix of operators having for elements the $\hat{K}_{ij}$. Notice that $\hat{\mathbf{K}}$ is a positive definite linear operator since Eqs. (8) and (9) result from a quadratic expansion of $E[\{\psi\}]$ in $|\delta\psi_i>$ about the minimum $E[\{\psi_0\}]$, i.e.:

$$E[\{\psi\}] - E[\{\psi_0\}] = \mu < \delta\psi_i |\hat{K}_{ij}| \delta\psi_j > +O(\delta\psi^3). \tag{10}$$

The equations of motion (8) and (9) can be formally integrated yielding:

$$|\delta\psi_i(t) >= \left(exp(-\hat{K}t)\right)_{ij} |\delta\psi_j(0) > \tag{11}$$

and

$$|\delta\psi_i(t) >= (cos\sqrt{\hat{K}}t)_{ij}|\delta\psi_j(0) > +(\hat{K}^{-1/2}sin\sqrt{\hat{K}}t)_{ij}|\delta\dot{\psi}_j(0) > , \tag{12}$$

respectively. In the case of first order evolution the wavefunctions decay exponentially towards the minimum $E[\psi_0]$, while in the second order evolution they perform small oscillations around it. These motions take place with characteristic decay rates and frequencies which are equal to the eigenvalues K_α of the operator $\hat{K}$ and to the square root $\sqrt{K_\alpha}$ of these eigenvalues for first and second order dynamics, respectively.

In numerical implementations the electronic states are expanded on a finite basis set, so that only a finite number of eigenfrequencies and eigenmodes occur. Let K_{min} and K_{max} be the minimum and maximum eigenvalues of $\hat{K}$. The maximum allowed time-step for numerical integration is proportional to the smallest period of the system, i.e. to $1/K_{max}$ or to $1/\sqrt{K_{max}}$ for first and second order dynamics, respectively.

In the case of first order dynamics, the minimum eigenvalue dominates the long-time behavior of the decay to the ground-state, so that a rough estimate of the convergence time is given by $1/K_{min}$. Recalling that the size of the time step is proportional to $1/K_{max}$, one finds that the number n_{O1} of integration steps needed to converge satisfies the condition:

$$n_{O1} \propto K_{max}/K_{min}. \tag{13}$$

In the case of second order dynamics we usually start a simulation from an electronic configuration close to the minimum of the electronic energy. Then if the ionic and the electronic frequencies are well decoupled[1,2], the electrons remain adiabatically close to the instantaneous energy minimum during the ionic evolution. Let ω_{ion} be a typical ionic frequency. The adiabatic condition requires it to be much smaller than the minimum electronic frequency i.e.

$$\omega_{ion} << \sqrt{K_{min}}. \tag{14}$$

A meaningful measure of the simulation's workload is given by the number of time steps necessary to integrate a full ionic oscillation. Thus, recalling that the time step is inversely proportional to $\sqrt{K_{max}}$, we find that the number n_{O2} of steps necessary to integrate a typical ionic oscillation satisfies the following condition:

$$n_{O2} \propto \sqrt{K_{max}/K_{min}}. \tag{15}$$

III. DAMPED SECOND ORDER DYNAMICS FOR MINIMIZATION

In the previous section we showed that the number of iterations necessary to minimize the electronic energy within steepest descent dynamics is proportional to K_{max}/K_{min}. In this section we present an improved *minimization* dynamics in which the typical number of iterations is instead proportional to $\sqrt{K_{max}/K_{min}}$, i.e. a number significantly smaller than K_{max}/K_{min}. We attain this goal by inserting in Eq. (4) a damping term as follows:

$$\mu|\ddot{\psi}_i> = -\frac{1}{2}\frac{\delta E[\{\psi\}]}{\delta\psi_i} - 2\gamma\mu|\dot{\psi}_i> +\Lambda_{ij}|\psi_j> \tag{16}$$

This equation defines a damped second order dynamics. As in the previous section we study the resulting motion close to the energy minimum. We find that the deviations of the wavefunctions from the minimum are subject to damped oscillations given by:

$$|\delta\psi_i(t)> = exp(i\hat{W}_+ t)_{ij}|\psi_j^{(+)}> +exp(i\hat{W}_- t)_{ij}|\psi_j^{(-)}> \tag{17}$$

Here $|\psi_j^{(+)}>$ and $|\psi_j^{(-)}>$ are determined by the initial conditions, and

$$\hat{W}_\pm = i\gamma 1 \pm \sqrt{\hat{K} - \gamma^2 1} \tag{18}$$

The real part of $\hat{W}_\pm$ gives the frequencies of the oscillatory motion, while its imaginary part gives the decay rate to the minimum. In order to maximize the rate of convergence, we must use the maximum value of γ for which the argument of the square root remains positive. This optimal value of γ is given by

$$\gamma_{opt} = \sqrt{K_{min}}, \tag{19}$$

since this value corresponds to critical damping of the smallest eigenvalue of $\hat{K}$. In this case the imaginary part of all the eigenvalues of $\hat{W}_\pm$ is equal to γ_{opt} and the time of convergence to the minimum is of the order of $1/\sqrt{K_{min}}$. The integration time step is related to the maximum norm of the eigenvalues of $\hat{W}_\pm$, which is equal to $\sqrt{K_{max}}$. Thus, the number of integration steps necessary for minimization is given by:

$$n_{DO2} \propto \sqrt{\frac{K_{max}}{K_{min}}} \propto \sqrt{n_{O1}}. \tag{20}$$

From this formula we see that a relevant gain of efficiency is obtained when using damped dynamics instead than steepest-descent dynamics to minimize the electronic energy. The gain is particularly important when a large number of iterations is needed to converge to the ground-state, which is typically the case of metallic systems.

IV. SECOND ORDER EXPANSION OF THE LDA ENERGY FUNCTIONAL

In this section we compute explicitly the eigenvalues of the operator **K**. For this purpose we consider the expansion of the energy functional around its minimum $\psi^{(0)}$ up to second order in $\delta\psi$. This is given by:

$$E[\{\psi\}] - E[\{\psi^{(0)}\}] = 2 < \delta\psi_i|H_{KS}|\delta\psi_i > -2 < \delta\psi_i|\delta\psi_j >< \psi_i^{(0)}|H_{KS}|\psi_j^{(0)} > \tag{21}$$

$$+ \int dr \int dr' \delta\rho(r) \left[\frac{\delta^2 E_h}{\delta\rho(r)\delta\rho(r')} + \frac{\delta^2 E_{xc}}{\delta\rho(r)\delta\rho(r')} \right] \delta\rho(r') + O(\{\delta\psi^3\}).$$

The second term on the r.h.s. of this equation comes from the Lagrange multipliers (see Eq. (7)), and

$$\delta\rho(r) = 4 < \psi_i^{(0)}|r >< r|\delta\psi_i > \tag{22}$$

gives the variation of the electronic density to first order in $\{\delta\psi\}$. We recall that $\{\psi\}$ and $\{\delta\psi\}$ are supposed to be real.

A. Non self-consistent case

If we neglect the last two terms in Eq. (21), i.e. the terms corresponding to variations of the Hartree and exchange-correlation potentials, we recover the expansion of the total energy appropriate to a non-selfconsistent Hamiltonian. Then we can expand the $\psi^{(0)}$ and $\delta\psi$ in terms of the the real eigenvectors $|\chi_l^0 >$ of H_{KS}, which have eigenvalues ε_l. Since the total energy is invariant under unitary transformations in the subspace of occupied states, we can suppose without loss of generality:

$$|\psi_i^{(0)} >= |\chi_i^0 >,$$

$$|\delta\psi_i >= \sum_k c_k^i |\chi_k^0 >, \tag{23}$$

where c_k^i are real coefficients. Here and in the following the indices i and k refer to occupied and unoccupied states, respectively. Hence, as shown in Ref. (15), we obtain for δE_{nsc}, i.e. the second-order variation of the energy in which the selfconsistency of the potential is not taken in account:

$$\delta E_{nsc} = 2 \sum_{ik} (c_k^i)^2 (\varepsilon_k - \varepsilon_i). \tag{24}$$

where ε_i and ε_k are respectively the occupied and the unoccupied eigenvalues of H_{KS}. By comparing Eq. (24) with Eq. (10) we see that the eigenvalues of $\hat{K}$ are given by

$$K_{(i,k)} = 2\frac{\varepsilon_k - \varepsilon_i}{\mu} \tag{25}$$

and the lowest eigenvalue of $\hat{K}$ is given by $K_{min} = 2E_{gap}/\mu$, in terms of the energy gap E_{gap} separating the lowest unoccupied from the highest occupied electronic level.

In the case of an insulator, the energy gap has a finite positive value which, above a certain size, is independent of the simulation cell. In the case of a metal instead, the energy gap is still finite and positive for a finite sized system but it is no longer independent of the simulation cell. In fact the energy gap and K_{min} tend to zero for a cell size going to infinity. However, many properties of interest do not require an infinite energy resolution for the states around the Fermi energy. Typically a small but finite energy resolution E_{err} is sufficient. E_{err} does not depend on the size of the system, and $K_{err} = 2E_{err}/\mu$ replaces K_{min} in Eq.s (13),(20) and (19) to estimate the convergence rates n_{O1}, n_{DO2} and the optimal damping parameter γ_{opt}. Since E_{err} is much smaller than a typical energy gap of an insulator, the number of iterations needed for ground state convergence is much larger in metals than in insulators. For the same reason, a perfectly adiabatic separation between ionic and electronic motions is not possible for metals. However, as shown in Ref. (16) a satisfactory solution to this problem, in the context of Car-Parrinello simulations, can be obtained by using two Nose' thermostats to control separately the respective temperatures of the ions and of the electrons.

When expanding the wavefunctions in terms of plane-waves, we can define an effective cut-off energy E_{cut} given (in a.u.) by $q_{max}^2/2$, where q_{max} is the largest wavevector in the basis set. The band of empty states is usually much larger than the band of occupied states. Thus when in Eq. (25) the index k refers to the highest unoccupied states, the eigenvalues $K_{(i,k)}$ of $\hat{K}$ have a negligible dependence on the occupied state index i. Furthermore, since the highest unoccupied states are free-particle like, the energy difference $\varepsilon_k - \varepsilon_i$ is dominated by the kinetic energy of the state k, i.e.

$$\varepsilon_k - \varepsilon_i \sim q^2/2, \qquad (26)$$

where q is the wavevector associated to the state k. The maximum eigenvalue of $\hat{K}$ is therefore approximately given by $K_{max} \simeq 2(q_{max}^2/2)/\mu = 2E_{cut}/\mu$. It is this eigenvalue that limits the maximum allowed time step for numerical integration in a non self-consistent case: the numerical integration becomes unstable and the time step has to go to zero when E_{cut} goes to infinity.

B. Self-consistent case: charge sloshing

We now consider the terms of Eq. (21) that we neglected in the previous subsection in order to see if they affect the maximum eigenvalue of $\hat{K}$. In this case $\hat{K}$ is not diagonal in the representation of the c_k^i and, for an arbitrary system, it is not possible to diagonalize it analytically. Thus we need some simplifying assumptions. Let us consider a crystal of given periodicity and use a supercell containing an arbitrary number of replicas of the crystal unit cell. In this case the $\{\psi_0\}$ are linear combinations of Bloch-functions with the crystal

periodicity whereas the fluctuations $\{\delta\psi\}$ may have all the wavelengths compatible with the supercell. In other words we are restricting the periodicity of the unperturbed state but not the periodicity of the fluctuations. Based on the above simplifying assumption we find that charge sloshing affects differently metallic and non-metallic systems. A numerical example presented in Sec. VII suggests that this result should hold also for non-periodic systems.

In order to find out whether the maximum eigenvalue of $\hat{K}$ diverges when the supercell size tends to infinity, we restrict our analysis to the Hartree term since the LDA exchange-correlation energy is well behaved and typically has a negligible effect compared to the kinetic energy on the maximum eigenvalue of $\hat{K}$. The second order variation of the Hartree energy is given by:

$$\delta E_H = \int dr \int dr' \delta\rho(\mathbf{r}) \frac{1}{|\mathbf{r}-\mathbf{r}'|} \delta\rho(\mathbf{r}') = \sum_G \sum_p \frac{4\pi}{\Omega|\mathbf{p}+\mathbf{G}|^2} |\delta\rho(\mathbf{p}+\mathbf{G})|^2. \tag{27}$$

Here $\mathbf{p}$ is a vector belonging to the first Brillouin Zone of the crystal, $\mathbf{G}$ is a vector of the reciprocal lattice of the crystal and the sums extend over all the non-zero wavevectors $\mathbf{p}+\mathbf{G} = \mathbf{q}-\mathbf{q}'$ where $\mathbf{q}$ and $\mathbf{q}'$ are two generic plane-waves of the basis set used to represent the electron wavefunctions in the supercell of volume Ω. $\delta\rho(\mathbf{p}+\mathbf{G})$ is the Fourier Transform (FT) of $\delta\rho(\mathbf{r})$.

When a linear dimension L of the supercell becomes very large, $(\mathbf{p}+\mathbf{G})_{min} = (\mathbf{p})_{min}$, i.e. the smallest nonzero $\mathbf{q}-\mathbf{q}'$ vector, tends to zero like $1/L$. If, correspondingly, the maximum eigenvalue of $\hat{K}$ diverges, we have the so-called 'charge sloshing' scenario. To study the effect of $\mathbf{p}_{min}$ on the maximum eigenvalue of $\hat{K}$ we consider only the terms with $\mathbf{G} = 0$ in Eq. (27). Then since $\delta\rho(\mathbf{r})$ is real, $|\delta\rho(\mathbf{p})| = |\delta\rho(-\mathbf{p})|$ and $\delta E_H(\mathbf{G} = 0)$ can be written as:

$$\delta E_H(\mathbf{G} = 0) = \sum_{\mathbf{p}, p_x > 0} \frac{8\pi}{\Omega p^2} |\delta\rho(\mathbf{p})|^2, \tag{28}$$

where

$$\delta\rho(\mathbf{p}) = \sum_{ik} 4(< \chi_i^0|cos(\mathbf{pr})|\chi_k^0 > c_k^i + i < \chi_i^0|sin(\mathbf{pr})|\chi_k^0 > c_k^i) \tag{29}$$

Notice that Eq. (28) is a quadratic form in terms of the c_k^i. The real coefficients c_k^i can be considered as the components of a real vector $|c>$. Similarly we can introduce two real vectors $|A(\mathbf{p})>$ and $|B(\mathbf{p})>$ whose components, labelled by the composite index (ik), are given by $< \chi_i^0|cos(\mathbf{pr})|\chi_k^0 >$ and by $< \chi_i^0|sin(\mathbf{pr})|\chi_k^0 >$, respectively. In this notation $\delta\rho(\mathbf{p}) = 4(< c|A(\mathbf{p}) > + i < c|B(\mathbf{p}) >)$ and Eq. (28) becomes:

$$\delta E_H(\mathbf{G} = 0) = \sum_{\mathbf{p}, p_x > 0} \frac{8\pi}{\Omega p^2}(< c|A(\mathbf{p}) >< A(\mathbf{p})|c > + < c|B(\mathbf{p}) >< B(\mathbf{p})|c >). \tag{30}$$

Using the fact that the χ_i^0 are eigenstates of a periodic crystal, it is easy to show[17] that the vectors $|A(\mathbf{p})>$ and $|B(\mathbf{p})>$ constitute an orthogonal set:

x

$$< A(p)|A(p') > = \delta_{p,p'}\frac{\Omega}{2}S(p)$$

$$< B(p)|B(p') > = \delta_{p,p'}\frac{\Omega}{2}S(p) \tag{31}$$

$$< B(p)|A(p') > = 0$$

where $p_x, p'_x > 0$ and the 'static structure factor' $S(p)$ is defined by:

$$S(p) = \frac{1}{\Omega}\sum_{ik} < \chi_i^0|e^{-ipr}|\chi_k^0 >< \chi_k^0|e^{+ipr}|\chi_i^0 > . \tag{32}$$

Hence $|A(p) >$ and $|B(p) >$ are the vectors that diagonalize the quadratic form in Eq. (30). The corresponding eigenvalues of $\hat{K}$ are given by:

$$K_{A(p)} = K_{B(p)} = \frac{128\pi}{\mu\Omega p^2} < A(p)|A(p) > = \frac{128\pi}{\mu\Omega p^2} < B(p)|B(p) > = \frac{64\pi}{\mu}\frac{S(p)}{p^2} \tag{33}$$

Therefore, when a linear dimension L of the supercell tends to infinity and, correspondingly, p_{min} goes to zero, $K_{A(p_{min})}$ and $K_{B(p_{min})}$ do not diverge if $S(p)$ is of order $O(p^2)$.

We now consider a jellium model as a representative metallic system. In this case the χ_i^0 are plane waves and one finds[18]: $S(p) = p[1 - (p/p_F)^2/12]p_F^2/8\pi^2$, where p_F is the Fermi momentum, and $p < 2p_F$. As a consequence for L going to infinity, $K_{A(p_{min})}$ and $K_{B(p_{min})}$ diverge as L and the time step for numerical integration has to be reduced accordingly: this is a charge sloshing situation.

When the system is a periodic insulator one finds instead that $S(p)$ goes to zero as p^2 (see Appendix). As a consequence for L going to infinity, $K_{A(p_{min})}$ and $K_{B(p_{min})}$ tend to a constant and the time step for numerical integration is independent of L: charge sloshing is absent here.

We stress that the above conclusions apply only if we consider small fluctuations around the ground-state: this is the typical case of ab-initio molecular dynamics simulations of the ionic motion. However, in the initial steps of an electronic minimization procedure, the wavefunctions may be far from the ground-state. In this case it is possible to observe sloshing effects also in periodic systems having an insulating ground-state.

Since charge-sloshing is a consequence of the singularity of the Coulomb potential at small p, a simple way of eliminating charge-sloshing instabilities consists in replacing the Coulomb potential $4\pi/p^2$ with a Yukawa potential $4\pi/(p^2 + \alpha^2)$, where $2\pi/\alpha$ is a typical decay length of the order of the system size L_{min} that corresponds to the onset of the sloshing instability. In the case of an insulator we can use this technique to stabilize the numerical integration during the initial steps of an electronic minimization run. Then when we are sufficiently close to the ground-state we can set $\alpha = 0$ and converge to the exact ground-state. We will show with a numerical example in a subsequent section that this technique allows us to converge to the exact ground-state of a disordered insulating system with a number of steps independent of the system size. In the case of a metal it is not possible to set α equal to zero not even in the proximity of the ground-state. However we notice that

L_{min} is usually much larger than the typical screening length of a metal. The results of a numerical simulation for a large but finite metallic system should not change appreciably if the Coulomb potential is replaced by a Yukawa potential that is equal to the Coulomb potential for distances smaller than L_{min}.

V. PRECONDITIONING THE EQUATIONS OF MOTION

The numerical efficiency of all the fictitious dynamical methods previously introduced can be improved by preconditioning the dynamics in order to reduce the ratio K_{max}/K_{min}. This can be achieved by replacing the constant fictitious mass parameter μ in Eqs. (3,4, 16). with an arbitrary positive definite operator $\hat{\mu}$. The resulting increased arbitrariness in the choice of $\hat{\mu}$ can be exploited to compress the highest frequency components of the spectrum of the fictitious electron dynamics. Recalling that these are due basically to the high energy unoccupied states which are free-particle like (see Eq. (26)), we choose an operator $\hat{\mu}$ which is diagonal in q-space with eigenvalues $\mu(q)$ given by:

$$\mu(q) = \mu_0 \qquad \text{if } \tfrac{1}{2}q^2 < E_p$$
$$\mu(q) = \mu_0 \frac{q^2}{2E_p} \quad \text{if } \tfrac{1}{2}q^2 > E_p \tag{34}$$

Below a certain cutoff energy E_p, it is worth considering a constant mass μ_0, because the low energy eigenstates have a relevant potential energy contribution and are not free-particle like. The preconditioning cut-off E_p therefore represents the threshold above which the states are dominated by the kinetic energy.

It is easy to show that the solutions of the preconditioned equations of motions for small displacements, are still given by Eqs. (11,12,17) if the operator $\hat{K}$ is replaced by the operator $\hat{\tilde{K}}$ characteristic of the preconditioned dynamics. All the relations (13), (15), (20) found for first and second order dynamics with and without damping hold therefore also in the case of the preconditioned dynamics but, in the latter case, K_{max} and K_{min} have to be replaced by the maximum and minimum eigenvalues of $\hat{\tilde{K}}$, i.e. by $\tilde{K}_{max}$ and $\tilde{K}_{min}$.

The preconditioning cut-off E_p that minimizes the ratio $\tilde{K}_{max}/\tilde{K}_{min}$ is called the optimal preconditioning cutoff. It depends strongly on the atomic species, i.e. on the pseudopotentials and on the plane-wave cutoff that are used in the calculation. It depends only negligibly on the physical environment. Thus, for a given atomic species, it is possible to find the optimal preconditioning cutoff by performing calculations on a simple reference system. We present a typical example in Sec. VII.

VI. NUMERICAL IMPLEMENTATION

In our numerical implementation we adopt the standard procedures described in Refs. (2, 4) to integrate the equations of motion for first and second order dynamics. In the case of

damped second order dynamics we follow the procedure introduced in Ref. (16) to integrate Car-Parrinello dynamics in presence of a friction term. We obtain for first, second order and damped dynamics, respectively:

$$|\psi_i(t+\Delta)> = |\psi_i(t)> -2\hat{\mu}^{-1}\hat{H}_{KS}|\psi_i>\Delta + X_{ij}\hat{\mu}^{-1}|\psi_j(t)> \tag{35}$$

$$|\psi_i(t+\Delta)> = -|\psi_i(t-\Delta)> +2|\psi_i(t)> -2\hat{\mu}^{-1}\hat{H}_{KS}|\psi_i>\Delta^2 + X_{ij}\hat{\mu}^{-1}|\psi_j(t)> \tag{36}$$

$$|\psi_i(t+\Delta)> = |\psi_i(t-\Delta)> +$$

$$+ \left(|\psi_i(t)> -|\psi_i(t-\Delta)> -\hat{\mu}^{-1}\hat{H}_{KS}|\psi_i>\frac{\Delta^2}{2}\right)\frac{2}{1+\gamma\Delta} + X_{ij}\hat{\mu}^{-1}|\psi_j(t)> \tag{37}$$

where Δ is the integration time step and X_{ij} is a symmetric matrix equal to $\Lambda_{ij}\Delta$ for first order dynamics, equal to $\Lambda_{ij}\Delta^2$ for conservative second order dynamics, and equal to $\Lambda_{ij}\Delta^2/(1+\gamma\Delta)$ for damped second order dynamics. The matrix $\mathbf{X}$ is found by imposing the orthonormality of the wavefunctions at time $t+\Delta$:

$$<\psi_i(t+\Delta)|\psi_j(t+\Delta)> = \delta_{ij} \tag{38}$$

We notice that the inversion of the mass operator $\hat{\mu}$ is straightforward in q space where it is diagonal. For the calculation of X_{ij} we define the wavefunctions $|\bar{\psi}_i(t+\Delta)>$ as the r.h.s. of the Eq. (35,36,37) without the orthonormalization terms $X_{ij}\hat{\mu}^{-1}|\psi_j(t)>$. Then Eq. (38) becomes:

$$\mathbf{X}\mathbf{M}\mathbf{X}^\dagger + \mathbf{B}\mathbf{X}^\dagger + \mathbf{X}\mathbf{B}^\dagger = \mathbf{1} - \mathbf{A} \tag{39}$$

where the matrices $\mathbf{M},\mathbf{B},\mathbf{A}$ are given respectively by:

$$M_{ij} = <\psi_i(t)|\hat{\mu}^{-2}|\psi_j(t)> \tag{40}$$

$$B_{ij} = <\bar{\psi}_i(t+\Delta)|\hat{\mu}^{-1}|\psi_j(t)> \tag{41}$$

$$A_{ij} = <\bar{\psi}_i(t+\Delta)|\bar{\psi}_j(t+\Delta)>. \tag{42}$$

The scalar products are easily evaluated in q-space where the mass operator $\hat{\mu}$ is diagonal.

Eq. (39) is formally identical to the matrix equation that expresses the orthonormality condition for Car-Parrinello dynamics when using Vanderbilt's ultrasoft pseudopotentials[19]. It can be solved as described in Ref. (19). The matrix $\mathbf{B}$ can be conveniently split into a symmetric part $\mathbf{B_s}$ and an antisymmetric part $\mathbf{B_a}$. The antisymmetric part $\mathbf{B_a}$ is first order in Δ, while $\mathbf{X}$ and $\mathbf{1} - \mathbf{A}$ are first (second) order in Δ for first (second) order dynamics. Using these properties, we can solve Eq. (39) iteratively in terms of increasing powers of Δ (Δ^2):

$$\mathbf{B_s X}^{(n+1)} + \mathbf{X}^{(n+1)} \mathbf{B_s} = 1 - \mathbf{A} - \mathbf{X}^{(n)} \mathbf{M X}^{(n)} - \mathbf{B_a X}^{(n)} + \mathbf{X}^{(n)} \mathbf{B_a} \tag{43}$$

Here $\mathbf{X}^{(0)}$ is the solution of the equation:

$$\mathbf{B_s X}^{(0)} + \mathbf{X}^{(0)} \mathbf{B_s} = 1 - \mathbf{A} \tag{44}$$

and the l.h.s of the Eq. (43,44) is inverted after transforming to the basis where $\mathbf{B_s}$ is diagonal.

An alternative approach based on an unconstrained total energy functional which avoids explicit orthonormalization has been recently proposed in Refs. (24, 25). The electronic mass preconditioning scheme discussed in the present paper can be easily applied to the unconstrained energy functional method without any overload.

In some applications of fictitious dynamical methods for electrons the orthonormalization of the electronic wavefunctions can be achieved via a Gram-Schmidt procedure. We stress that this approach is not justified in connection with the mass preconditioning scheme described above. Indeed if the Gram-Schmidt orthogonalization procedure is used within preconditioned steepest-descent dynamics, one is not guaranteed that the energy will decrease at any integration step for a sufficiently small time step. The origin of this instability is related to the non-holonomic character of the constraints imposed via a Gram-Schmidt procedure. We found that this instability is rather severe in practical numerical applications, where it spoils all the efficiency gains of the mass preconditioning scheme.

VII. NUMERICAL RESULTS

We tested the different dynamical schemes described above on various physical systems within a DFT-LDA formulation. In particular we considered Si and C systems. We used pseudopotentials of the Bachelet-Hamann-Schlüter type[20], with s and p non-locality in the Kleinmann-Bylander form[21]. The cut-off for the plane-wave expansion of the electronic orbitals was 12 Ry for silicon, and 35 Ry for carbon. We carried out all the calculations at the Γ point of the Brillouin zone only. Moreover, in order to compare the dynamical schemes with conjugate gradient minimization, we used a tight-binding energy functional for carbon[22].

A. preconditioning

We start by presenting the results obtained with preconditioning. In order to determine the optimal preconditioning cut-off E_p we had to minimize the ratio $\bar{K}_{max}/\bar{K}_{min}$. We measured $\bar{K}_{max}$ and $\bar{K}_{min}$ within first order and second order dynamics, by giving a small displacement to the system from its energy minimum. In the case of first order dynamics, the numerical integration of Eq. (35), becomes unstable and results in an exponential increase of the energy, when $\Delta > 2/\bar{K}_{max}$. Therefore the maximum allowed integration time

step provides an accurate way of estimating $\bar{K}_{max}$. $\bar{K}_{min}$, i.e. the lowest eigenvalue of $\hat{\bar{K}}$, gives instead the slowest rate of decay of the energy. This rate is conveniently sampled at large times, i.e. when only the slowest exponential is left in the decay.

We report in Fig. (1) the ratio $\bar{K}_{max}/\bar{K}_{min}$ as a function of E_p for a Si$_3$ molecule. We notice that for the highest E_p values the ratio decreases linearly with decreasing E_p. The behavior of the ratio $\bar{K}_{max}/\bar{K}_{min}$ in this range is explained by the following considerations. First, the minimum frequency is unchanged, since it is related to the lowest excited state which has small components at high q. Second, all the excited modes at energies higher than E_p are compressed to the same maximum frequency $2E_p/\mu_0$, as long as they are kinetically dominated. Instead, in the range of low preconditioning cut-offs E_p, the minimum frequency $\bar{K}_{min}$ decreases and the highest excited modes become less efficiently compressed. Thus a minimum value of the ratio $\bar{K}_{max}/\bar{K}_{min}$ is found, as we can see in Fig. (1). This minimum occurs at $E_p=1$ Ry. The corresponding reduction of the ratio $\bar{K}_{max}/\bar{K}_{min}$ is of a factor of 5 compared to the non-preconditioned case. We obtained very similar results for a sample of crystalline silicon in the diamond structure, where the optimal E_p was also close to 1 Ry.

In the case of second order dynamics $\sqrt{\bar{K}_{max}}$ and $\sqrt{\bar{K}_{min}}$ can be found as the maximum and minimum frequencies of the power spectrum of the fictitious electronic dynamics. This is easily evaluated by computing the velocity autocorrelation function corresponding to the wavefunction dynamics. The power spectrum of the velocity autocorrelation function corresponding to the electronic fictitious dynamics is given in Fig. (2) for the case of the Si$_3$ molecule. In particular we show results obtained with optimal preconditioning ($E_p = 1$ Ry) and unpreconditioned dynamics. In calculating the spectra we chose the value of μ_0 in such a way that the lowest frequency $\sqrt{\bar{K}_{min}}$ of the preconditioned dynamics coincided with $\sqrt{K_{min}}$, i.e. the lowest frequency of the dynamics without preconditioning. This is achieved by setting $\mu_0=260$ a.u. when the mass associated to the dynamics without preconditioning is $\mu=300$ a.u.. The significant compression of the high frequency modes resulting from preconditioning is clearly evident in Fig. (2).

For a sample of crystalline carbon in the diamond structure we found an optimal value of E_p equal to 2.7 Ry. This reduced by a factor of 9 the ratio $\bar{K}_{max}/\bar{K}_{min}$ compared to the unpreconditioned case. In this case in order to make the lowest frequencies $\sqrt{\bar{K}_{min}}$ and $\sqrt{K_{min}}$ to coincide, the mass μ of the unpreconditioned dynamics had to be rescaled by a factor of 0.93 in order to obtain the mass μ_0 of the preconditioned dynamics.

We notice that in a different context the authors of Ref. (7) proposed to use a preconditioning cutoff E_p equal to the expectation value of the kinetic energy divided by the number of electrons. In the cases discussed above this corresponds to a value of $E_p = 0.8$ Ry and $E_p = 2$ Ry for Si and C, respectively. These values are close to the optimal values of E_p.

B. Ionic Molecular Dynamics

In order to test the effect of preconditioning on ab-initio molecular dynamics simulations of the ionic motion, we considered the coupled set of equations given by Eq. (4) for the electronic degrees of freedom and by

$$M_i \ddot{\mathbf{R}}_i = -\frac{\delta E[\{\psi\}, \mathbf{R}]}{\delta \mathbf{R}_i} \tag{45}$$

for the ionic coordinates $\mathbf{R}_i$. Here M_i are the physical ionic masses and the mass μ in Eq. (4) has to be replaced by the mass operator $\hat{\mu}$ in the preconditioned case. Eq. (4) and (45) reproduce the adiabatic dynamics of the ions when the appropriate decoupling condition, Eq. (14) discussed in Sec. II, is satisfied[1,2]. We considered the vibrational motion of a Si_3 molecule during a time span of about 0.3 ps. In the unpreconditioned case we used a time step $\Delta=7$ a.u. to integrate the equations of motion. This is close to the maximum allowed time step for a fictitious electronic mass $\mu=300$ a.u.. Preconditioning allowed to increase this time step to $\Delta=15$ a.u. for a mass $\mu_0=260$ a.u. and a preconditioning cut-off $E_p=1$ Ry. In spite of the significantly larger time step the preconditioned dynamics proceeded adiabatically in the same way as the one without precontioning. In particular, any systematic energy transfer from the ionic system to the electronic one was absent. We plot in Fig. (3) the temporal evolution of the ionic kinetic energy and of the longest side of the Si_3 molecule as a function of time in both the preconditioned and the unpreconditioned cases. Differences between the two dynamics are not noticeable.

C. Damped dynamics in Insulators

In order to assess the efficiency of the various minimization dynamics discussed in this work, we considered a 64 atom amorphous Si sample generated by ab-initio molecular dynamics[23]. We notice that this system has a finite gap, and therefore a non-zero $\bar{K}_{min}$. In all our total energy minimizations we used the same set of starting trial wavefunctions. These were obtained by minimizing the total energy with a very small energy cut-off E_{cut} of 2 Ry. We then minimized the total energy with a cut-off of 12 Ry using four types of dynamics, namely steepest descent and second order damped dynamics both without and with optimal preconditioning. We report the results in Fig. (4). In particular, we found that, when using the optimal value γ_{opt} of Eq. (19), the rate of convergence of second order damped dynamics is faster than that of steepest descent dynamics by the amount expected from the theoretical analysis in Sec. III. Preconditioning accelerated further the rate of convergence, so that finally the rate of convergence of preconditioned second order damped dynamics was 14 times faster than the one of unpreconditioned steepest descent.

We determined the value γ_{opt} by a rough estimate of $\bar{K}_{min}$ based on steepest descent dynamics. In particular, a 3 point fit of the exponential decay of the total energy gives:

$$\gamma_{opt}\Delta \sim \sqrt{\frac{1}{2}ln\left(\frac{E_1 - E_2}{E_2 - E_3}\right)} \qquad (46)$$

where E_1 E_2 E_3 are the energies at three successive steps of steepest descent. We waited until only the slowest exponential was left in the decay. If faster exponentials are still present, Eq. (46) overestimates $\gamma_{opt}\Delta$. In a practical calculation, we therefore suggest to start the minimization with a few steps of steepest descent and to use Eq. (46) to obtain an upper bound for the optimal $\gamma\Delta$. Then, we suggest to proceed with the damped second order minimization, readjusting $\gamma\Delta$ in order to achieve the optimal limit of critical damping. As we can see from Fig. (4), it is indeed convenient to use steepest descent in the first steps of minimization when the highest frequency components dominate the deviation of the energy from the minimum. Subsequently, when only the slowest frequencies are left, damped dynamics becomes much more convenient, especially in those cases of utterly slow convergence rate.

D. Damped dynamics in Metallic Systems

In order to test the efficiency of our damped dynamical scheme for minimization in the case of metallic systems we applied it to liquid silicon which is a metal. We use a 64 atom sample generated by ab-initio molecular dynamics[14]. As explained in Sec. IV, the damping constant γ can be fixed on the basis of the required energy resolution E_{err}, for which we chose here a value of about $20meV$. We minimized the total energy with a cutoff of 12 Ry using four types of dynamics, similarly to what we did in the insulating case. Again the starting trial wavefunctions were obtained by a minimization using a small cutoff of 2 Ry. We report the results in Fig. (5). Notice that in the present metallic case, steepest descent dynamics is particularly inefficient, while damped dynamics is very effective, since it improves by many orders of magnitude the convergence rate of steepest descent. A further gain results from preconditioning.

E. Comparison with Conjugate Gradient Minimization

In this subsection we compare our damped dynamical method with a conjugate gradient minimization scheme. The standard conjugate gradient procedure, described e.g. in Ref. (5), cannot be directly applied to a constrained functional, unless some additional simplifying assumptions are invoked which can reduce the minimization efficiency[6,7]. To fully exploit the power of the conjugate gradient procedure the authors of Ref. (10) proposed to use an unconstrained energy functional. We adopt the same procedure of Ref. (10) but we use a different form for the unconstrained energy functional. We use the form suggested in Refs. (24, 25) in the context of electronic structure calculations with linear size scaling but without imposing any localization constraints on the electronic orbitals[26]. For reasons of

numerical simplicity we adopt here a total energy functional based on a non self-consistent tight-binding Hamiltonian. This choice simplifies considerably the line minimization in the conjugate gradient scheme, which can be performed exactly[25].

We used a tight-binding Hamiltonian for carbon[22], and we considered an ionic liquid configuration of 64 atoms at a temperature of 5000 K. For this configuration the system is metallic. Our results are reported in Fig. (6) where we plot the logarithmic error in the total energy per atom versus the number of iterations for various minimization schemes, namely damped dynamics, conjugate gradient and steepest descent minimization. In the case of conjugate gradient minimization the number of iterations was multiplied by a factor of 2 in order to take into account the increase in computational cost arising from line minimization. From Fig. (6) it is evident that the numerical efficiency of both conjugate gradient and of damped molecular dynamics is considerably superior to that of steepest descent minimization. In the present example the numerical efficiency of conjugate gradient and that of damped molecular dynamics minimization are practically the same.

We expect that the results that we have found here should remain valid also of in the case of a self-consistent LDA Hamiltonian.

F. Charge sloshing on very long cells

In order to study charge sloshing effects we used a tetragonal supercell having a long side. In particular we considered crystalline silicon in the diamond structure and we constructed two supercells by repeating four or eight elementary cubic cells along the crystallographic (100) direction. The resulting supercells contain 32 and 64 atoms respectively. Then we broke the translational invariance of the diamond lattice by giving the silicon atoms a random displacement of about 5 percent of the bond length. This did not modify the insulating character of the system.

In the present example we have considered only preconditioned steepest descent minimization. As in the previous subsections we prepared the initial trial state by minimizing the total energy with a small cutoff of 2 Ry starting from a set of random wavefunctions. Severe charge sloshing instabilities immediately showed up during this initial minimization in which the starting random wavefunctions were very far from the converged insulating ground-state. In particular, already for the 32 atom cell the time step for numerical integration had to be reduced by an order of magnitude compared to the time step that we could use in an equivalent situation with a smaller cell. Such instability was completely eliminated by replacing the Coulomb by a Yukawa potential as described in Sec. IV. We adopted here a parameter $2\pi/\alpha = 20.5$ a.u. for the Yukawa potential. Once obtained the initial trial state, we performed a total energy minimization on the 32 and on the 64 atom cell with a cutoff of 12 Ry. The results are shown in Fig. (7) which reports the deviation from the converged ground-state energy as a function of the number of numerical time steps. During the initial 30 steps we used the Yukawa potential. This allowed us to use for both 32 and 64 atom cells

an integration time step equal to the one usually adopted for the same system when using cells sufficiently small that no charge sloshing effects are present. Then we switched from Yukawa to Coulomb potential. After 30 minimization steps with the Yukawa potential the system was insulating and already very close to its exact ground-state. In this case, as shown analytically in Sec. IV charge sloshing instabilities are not expected to occur in a periodic system. Indeed not even in our disordered sample they did occur. Therefore we could use in the final 30 minimization steps the same time step used with the Yukawa potential. The overall convergence rate, as it can be clearly seen in the figure, is independent from the cell size.

VIII. CONCLUSIONS

We have presented a detailed analysis of the stability and of the convergence rate of fictitious dynamical methods for electrons. We have succeeded in improving considerably the efficiency of currently used algorithms for total energy minimization and for ab-initio molecular dynamics.

In the case of ab-initio molecular dynamics simulations of the ionic motion we have introduced a novel preconditioning scheme which gives rise to an overall saving of CPU time of the order of 2-3 in typical applications. In the case of total energy minimization we have introduced an optimal damped preconditioned dynamics which has a convergence rate substantially faster than steepest descent algorithms and comparable to that of the best conjugate gradient schemes for electronic structure calculations. This is especially important in metallic situations.

Although in this paper we confine our analysis to electronic minimization, we stress that the damped dynamics algorithm can also be applied to ionic minimization. In this case the optimal ionic damping parameter is related to the phonon frequencies of the system under study.

In addition, we have presented a detailed analysis of the charge sloshing instability and we have indicated a practical way to control it. We have shown with a numerical example that, in the case of insulators, our approach allows us to converge to the ground-state with a number of iterations that is independent of the system size.

IX. ACKNOWLEDGEMENTS

X. NOTE ADDED TO PROOF

In Sec. VII.E we have shown numerically on a specific example that conjugate gradient minimization and our damped dynamics scheme have a similar convergence rate. Recently we became aware that this can be shown also analytically. In fact the convergence rate of the conjugate gradient approach is proportional to $\sqrt{K_{min}/K_{max}}$ as that of our damped dynamical method. An analytical estimate of the convergence rate of conjugate gradient minimization can be found in A. Jennings and J.J. McKeown, *Matrix Computation* 2nd Edition, (Wiley, Chichester,1992) and in J. Stoer and R. Bulirsch, *Introduction to Numerical Analysis*, (Springer Verlag, New York, 1992). This has been extended to the minimization of the DFT-LDA functional in J. Annett (unpublished). We thank J. Annett for sending us a preprint of his work prior to publication.

XI. APPENDIX

In this appendix we show that for a periodic insulator the function S(p) given in Eq. (32) goes to zero like p^2 for p going to zero.

$$S(\mathbf{p}) = \frac{1}{\Omega} \sum_{ik} < \chi_i^0 | e^{-i\mathbf{p}\mathbf{r}} | \chi_k^0 >< \chi_k^0 | e^{+i\mathbf{p}\mathbf{r}} | \chi_i^0 >$$

$$= \frac{1}{\Omega} \sum_i (1 - \sum_j < \chi_i^0 | e^{-i\mathbf{p}\mathbf{r}} | \chi_j^0 >< \chi_j^0 | e^{+i\mathbf{p}\mathbf{r}} | \chi_i^0 >),$$

(47)

where the indices i and j refer to occupied states and the index k refers to empty states. In Eq. (47) we used the completeness relation: $\sum_k | \chi_k^0 >< \chi_k^0 | = 1 - \sum_j | \chi_j^0 >< \chi_j^0 |$. Let us suppose for simplicity that we have a single occupied band. Since the expression in Eq. (47) is invariant under unitary transformations on the occupied subspace, we can write it in terms of Wannier functions, i.e.:

$$S(\mathbf{p}) = \frac{1}{\Omega_{min}} (1 - \sum_{\mathbf{R}} | < W_0 | e^{-i\mathbf{p}\mathbf{r}} | W_{\mathbf{R}} > |^2),$$

(48)

where $W_{\mathbf{R}}$ is the Wannier function centered on site $\mathbf{R}$, and Ω_{min} is the volume of the elementary cell. The Wannier functions are exponentially localized in the case of an insulator: this allows us to expand in a Taylor series for p going to zero the exponentials in Eq. (48). In particular if we consider the term with $\mathbf{R} = 0$ in Eq. (48), and expand the exponentials in $\mathbf{p}\mathbf{r}$ around $\mathbf{p} < \mathbf{r} > = \mathbf{p} < W_0 | \mathbf{r} | W_0 >$, we get:

$$1 - | < W_0 | e^{-i\mathbf{p}\mathbf{r}} | W_0 > |^2 =$$

$$= 1 - | < W_0 | 1 - i\mathbf{p}(\mathbf{r} - < \mathbf{r} >) - [\mathbf{p}(\mathbf{r} - < \mathbf{r} >)]^2/2 | W_0 > |^2 + o(p^2)$$

(49)

$$= + < W_0 | [\mathbf{p}(\mathbf{r} - < \mathbf{r} >)]^2 | W_0 > + o(p^2)$$

This term tends to zero as p^2. In a similar way one can show that the terms with $\mathbf{R}$ different from zero in Eq. (48) also go to zero as p^2.

REFERENCES

[1] R. Car and M. Parrinello, Phys. Rev. Lett., **55**, 2471, (1985).

[2] R. Car and P. Parrinello, in *Simple Molecular Systems and Very High Densities*, ed. by A. Polian, P. Loubeyre, and N. Boccara,(Plenum Press, New York, 1988) p. 455.

[3] *Theory of the Inhomogeneous Electron Gas*, edited by S. Lundqvist and N.H. March (Plenum Press, New York, 1983).

[4] For a review see e.g., G. Galli and A. Pasquarello, *New Perspectives on Computer Simulations in Chemical Physics* (Kluwer, Dordrecht, in press).

[5] W.H.Press, A.A. Teukoisky,W.T. Vetterling and B.P.Flannery *Numerical Recipes* (Cambridge University Press, USA, 1992).

[6] I.Stich, R.Car, M.Parrinello and S.Baroni, Phys. Rev. B, **39**, 4997 (1989).

[7] M. P. Teter, M. C. Payne and D. C. Allan, Phys. Rev. B, **40**, 12225, (1989).

[8] R.K. Nesbet J. Chem. Phys. **43**, (1965) 311.

[9] P.Bendt and A.Zunger Bull. Am. Soc. **27** (1982) 248, D.M.Wood and A.Zunger J. Phys. A **18** (1985) 1343.

[10] T.A.Arias, T.A.Payne and J.D.Joannopoulos, Phys. Rev. Lett., **69**, 1077 (1992).

[11] M. C. Payne, D. Joannopoulos, D. C. Allan, M. P. Teter and D. H. Vanderbilt, Phys. Rev. Lett., **56**, 2656, (1986).

[12] A.Williams and J.Soler, Bull. Am. Phys. Soc. bf 32, 562 (1987).

[13] R.M.Martin and K.Kunc in *Ab Initio Calculation of Phonon Spectra*, edited by J.T.Devreese (Plenum Press, New York, 1983) pag.49.

[14] O. Sugino and R. Car, Bull. Am. Phys. Soc. bf 39, 278 (1994), O. Sugino and R. Car, unpublished.

[15] G. Pastore, E. Smargiassi, and F. Buda, Phys. Rev. A., **44**, 6334, (1991).

[16] P. E. Blöchl, and M. Parrinello, Phys. Rev. B, **45**, 9413, (1993).

[17] to this purpose it is useful to apply the relation $\sum_{ik} < \chi_i^0 |e^{-i\mathbf{p}\mathbf{r}}|\chi_k^0 >< \chi_k^0 |e^{+i\mathbf{p}'\mathbf{r}}|\chi_i^0 >= \Omega S(\mathbf{p})\delta_{\mathbf{p},\mathbf{p}'}$, where $S(\mathbf{p})$ is given in Eq. (32).

[18] see e.g. V.D. Gorobchenko, V.N. Kohon and E.G. Maksimov in *Modern Problems in Condensed Matter Sciences*, edited by V.M. Agranovich and A.A. Maradudin (North-Holland, Netherlands,1989) vol. 24 pag. 113.

[19] A. Pasquarello, K. Laasonen, R. Car, C. Lee and D. Vanderbilt, Phys. Rev. Lett., **69**, 1982 (1992); K. Laasonen, A. Pasquarello, R. Car, C. Lee and D. Vanderbilt, Phys. Rev.

B, **47**, 10142, (1993).

[20] G. B. Bachelet, D. R. Hamann, and M. Schlüter, Phys. Rev. B, **26**, 4199 (1982).

[21] L. Kleinmann and D. M. Bylander, Phys. Rev. Lett. **48**, 1425 (1982).

[22] C. Xu, C. Wang, C. Chan, and K. Ho, J.Phys.: Condens. Matter **4**, 6047 (1992).

[23] I. Stich, R. Car, M. Parrinello, Phys. Rev. B, **44**, 4262, (1991).

[24] F. Mauri, G. Galli and R. Car, Phys. Rev. B, **47**, 9973 (1993).

[25] F. Mauri, G. Galli, Phys. Rev. B **50**, 4316 (1994).

[26] Since we do not impose localization constraints on the electronic orbitals the cost of the calculation still grows as the cube of the system size, as in standard electronic structure calculations. As shown in Ref. (24) the miminum of the unconstrained energy functional coincide with that of the constrained functional. Moreover, since we adopt a truncation parameter $\mathcal{N} = 1$ (see Ref. (24)) for th e inverse of the overlap matrix, the minimization rate is the same for the unconstrained and the constrained functional[25].

Acknowledgements

It is a pleasure to gratefully acknowledge my supervisor Prof. Roberto Car for his scientific guidance and continuous advice throughout the whole thesis work.

The results presented in Chapters 5 and 6 arise from a collaboration with Dr. Giulia Galli. The Appendix is the fruit of a collaboration with Dr. Francesco Tassone.

I would like to thank Dr. Andrea Dal Corso who provided me his assistance and his software to generate the excited core carbon pseudopotential and to perform test calculations in bulk diamond, and Prof. Philip Allen for a critical reading of the manuscript.

Bibliography

[1] For a review see, e.g., G. Galli and A. Pasquarello, in Computer Simulation in Chemical Physics, Edited by M.P.Allen and D.J.Tildesley, p. 261, Kluwer, Dordrecht (1993), and M. C. Payne, M. P. Teter, D. C. Allan, T. A. Arias and J. D. Joannopoulos, Rev. Mod. Phys. **64**, 1045 (1993).

[2] For a review see, e.g., C. Z. Wang et al., Computational Material Science 1994, in press.

[3] For a review see, e.g., D. F. Coker, in Computer Simulation in Chemical Physics, Edited by M.P.Allen and D.J.Tildesley, p. 315 , Kluwer, Dordrecht (1993).

[4] R. Car and M. Parrinello, Phys. Rev. Lett. **55**, 2471 (1985), R. Car and P. Parrinello, in *Simple Molecular Systems and Very High Densities*, ed. by A. Polian, P. Loubeyre, and N. Boccara,(Plenum Press, New York, 1988) p. 455.

[5] F. Tassone, F. Mauri, and R. Car, Phys. Rev. B, (15 October 1994).

[6] *Theory of the Inhomogeneous Electron Gas*, edited by S. Lundqvist and N.H. March (Plenum Press, New York, 1983).

[7] W.H.Press, A.A. Teukoisky,W.T. Vetterling and B.P.Flannery *Numerical Recipes* (Cambridge University Press, USA, 1992).

[8] I.Stich, R.Car, M.Parrinello and S.Baroni, Phys. Rev. B, **39**, 4997 (1989); M. P. Teter, M. C. Payne and D. C. Allan, Phys. Rev. B, **40**, 12225, (1989); T.A.Arias, T.A.Payne and J.D.Joannopoulos, Phys. Rev. Lett., **69**, 1077 (1992).

[9] M.Born and J.R. Oppenheimer, Ann. der Phys. **84**, 457 (1927).

[10] H. Hellmann, Einfuerung in die Quantenchemie (Deuticke, Leipzig, 1937); R. P. Feynman, Phys. Rev. **56**, 340 (1939).

[11] G. Pastore, E. Smargiassi, and F. Buda, Phys. Rev. A **44**, 6334 (1991).

[12] F.Mauri, R.Car and E.Tosatti, Europhys.Lett. **24**, 431 (1993).

[13] P. E. Blöchl, and M. Parrinello, Phys. Rev. B, **45**, 9413, (1993).

[14] C.A.J. Ammerlaan, Inst. Phys. Conf. Ser. **59**, 81 (1981).

[15] R.J. Cook and D.H. Whiffen, Proc. Roy. Soc. London A **295**, 99 (1966).

[16] S.A. Kajihara, A. Antonelli, J. Bernholc, and R. Car Phys. Rev. Lett. **66** 2010 (1991).

[17] J.F. Morar *et all*, Phys. Rev. Lett. **54**, 1960 (1985).

[18] K.A. Jackson and M.R. Pederson, Phys. Rev. Lett. **67**, 2521 (1991).

[19] J. Nithianandam, Phys. Rev. Lett. **69**, 3108 (1992).

[20] P.E. Batson, Phys. Rev. Lett. **70**, 1822 (1993).

[21] Y. Ma, P. Skytt, N. Wassdahl, P. Glans, D.C. Mancini, J. Guo, and J. Nordgren, Phys. Rev. Lett. **71**, 3725 (1993).

[22] W. Hayes and A.M. Stoneham , *Defects and defect processes in non-metallic solids*, (Whiley & Sons, New York, 1985) pag.s 29-38.

[23] A.W.S. Williams, E.C. Lightowlers, and A.T. Collins J. Phys. C **3**, 1727 (1970); J.C. Bourgoin, J. Krynicki, and B. Blanchard, Phys. Status Solidi (a) **52**, 293 (1979).

[24] R.G. Farrer, Solid State Commun. **7**, 685 (1969).

[25] Landolt-Boernstein, New series, Group III, Vols 17a and 22a, edited by K.-H. Hellwege and O. Madelung (Springer, Berlin, 1982).

[26] M.S. Hybertsen and S.G. Louie, Phys. Rev. B **34**, 5390 (1986).

94

[27] M. Rohfing, P. Krueger, and J. Pollmann, Phys. Rev. B **48** , 17791 (1993).

[28] G. Bachelet, D. Hamann, and M. Schlüter, Phys. Rev. B **26**, 4199 (1982).

[29] E. Pehlke and M. Scheffler, Phys. Rev. B **47**, 3588 (1993).

[30] R. Car and U. von Barth, unpublished.

[31] L. Kleinman and D. M. Bylander, Phys. Rev. Lett. **48**, 1425 (1982).

[32] G. Galli, R. M. Martin, R. Car and M. Parrinello, Phys. Rev. B **42** 7470 (1990).

[33] M.R. Pederson and K.A. Jackson, Phys. Rev. B **41**, 7453 (1990).

[34] S. V. Govorkov, I. L. Shumay, W. Rudolph, and T. Schroder, Opt. Lett. **16**, 1013 (1991); P. Saeta, J.-K. Wang, Y. Siegal, N. Bloembergen, and E. Mazur Phys. Rev. Lett. **67**, 1023 (1991); K. Sokolowski-Tinten, H. Schulz, J. Bialkowski, and D. von der Linde.

[35] G. Galli and M.Parrinello, Phys. Rev. Lett. **69**, 3547 (1992).

[36] T. A. Arias, M. C. Payne and J. D. Joannopoulos, Phys. Rev. Lett. **69**, 1077 (1992).

[37] This is so in a PW calculation if advantage is taken of fast Fourier transform techniques and of the localized nature of non local pseudopotentials.

[38] W.-L. Wang and M. Teter, Phys. Rev. B **46**, 12798 (1992).

[39] F. Mauri, G. Galli, and R. Car, Phys. Rev. B **47**, 9973 (1993).

[40] W. Kohn, Chem. Phys. Lett. **208**, 167 (1993).

[41] P. Ordejón, D. Drabold, M. Grunbach, and R. Martin, Phys. Rev. B **48**, 14646 (1993).

[42] F. Mauri and G. Galli., Phys. Rev. B **50**, 4316 (1994).

[43] G. Galli and F. Mauri, unpublished.

95

[44] M. Aoki, Phys. Rev. Lett. **71**, 3842 (1993).

[45] S. Baroni and P. Giannozzi, Europhys. Lett. **17**, 547 (1991).

[46] X.-P. Li, R. Nunes, and D. Vanderbilt, Phys. Rev. B **47**, 10891 (1993).

[47] M. S. Daw, Phys. Rev. B **47**, 10895 (1993).

[48] A. D. Drabold and O. Sankey, Phys. Rev. Lett. **70**, 3631 (1993).

[49] S. Goedecker and L. Colombo Phys. Rev. Lett. **73**, 122 (1994).

[50] P. Löwdin, J. Chem. Phys. **18**, 365 (1950).

[51] R. McWeeny, Rev. Mod. Phys. **32**, 335 (1960).

[52] L. Goodwin, A. Skinner, and D. Pettifor, Europhys. Lett. **9**, 701 (1989).

[53] C. Xu, C. Wang, C. Chan, and K. Ho, J.Phys.: Condens. Matter **4**, 6047 (1992).

[54] R. Beck *et al.*, J. Phys. Chem. **95**, 8402 (1991).

[55] H.-G. Busman, T. Lill, and I. Hertel, Chem. Phys. Lett. **187**, 459 (1991).

[56] R. Mowrey *et al.*, J. Phys. Chem. **95**, 7138 (1991).

[57] H.-G. Busman, T. Lill, B. Reif, and I. Hertel, Surf. Sci. **272**, 146 (1992).

[58] T. Lill, H.-G. Busman, B. Reif, and I. Hertel, Appl. Phys. A **55**, 461 (1992).

[59] C. Yeretzian and R. L. Whetten, Z. Phys. D **24**, 199 (1992).

[60] Y. Li *et al.*, Phys. Rev. B **45**, 13837 (1992) and references therein.

[61] P. Blaudeck, T. Frauenheim, H.-G. Busman, and T. Lill, Phys. Rev. B . **49**, 11409 (1994).

[62] For a review see, e.g., C. Yeretzian, R.D. Beck and R.L. Whetten, Int. Jour. Mass Spectr. and Ion Proc. (in press).

96

[63] V. Paillard *et al.*, Phys. Rev. Lett. **71**, 4170 (1993); V. Paillard *et al.*, Phys. Rev. B **49**, 11433 (1994).

[64] B. Davidson and W. Pickett, Phys. Rev. B **49**, 11253 (1994).

[65] S. Iarlori *et al.*, Phys. Rev. Lett. **69**, 2947 (1992).

[66] C. Z. Wang, C. T. Chan and K. M. Ho, Phys. Rev. B **46**, 9761 (1992).

[67] B. Feuston, M. Andreoni, W. Parrinello, and E. Clementi, Phys. Rev. B. **44**, 4506 (1991); Q. Zhang. J.-Y. Yi and J. Bernholc, Phys. Rev. Lett. **66**, 2633 (1991).

[68] B. L. Zhang, C. Z. Wang, C. T. Chan and K. M. Ho, Phys. Rev. B **48**, 11381 (1993); S. Kim and D. Tománek, Phys. Rev. Lett. **72**, 2418 (1994).